



---

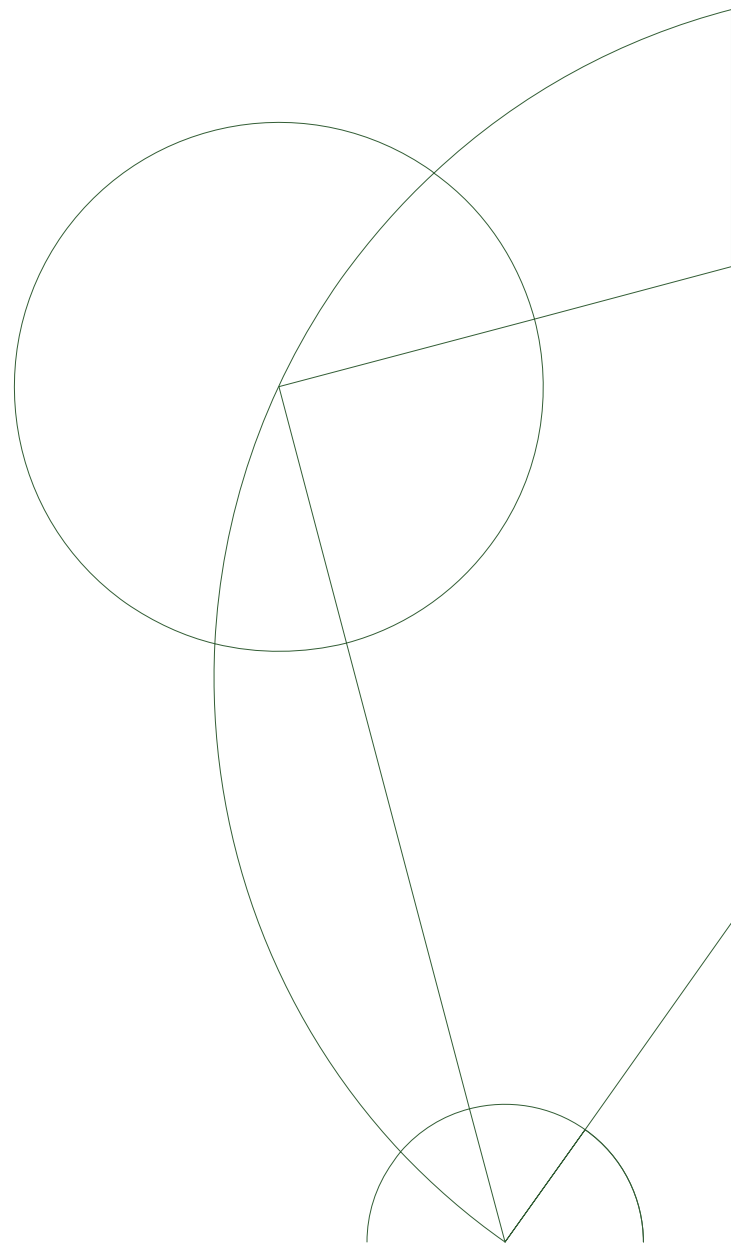
FREQUENCY CONVERSION OF SINGLE PHOTONS FOR  
LONG DISTANCE QUANTUM COMMUNICATION  
Master Thesis

**Written by:** Carlos F. D. Faurby

**Supervisor:** Leonardo Midolo

**Co-supervisors:** Xiaoyan Zhou, Beatrice da Lio

**Handed in:** 19.05.2021



---

## Abstract

To establish quantum communication over long distances it is important to have high quality single photons at the infrared frequency of 1550 nm. This is the wavelength for which there is optimal transmission through most of the existing telecom cables for optical communications. High quality single photons need to be anti-bunched and indistinguishable, and producing such photons directly at 1550 nm is a complex scientific challenge yet to be solved. On the other hand it is possible to produce high quality single photons at near infrared (NIR) wavelengths, using state of the art InGaAs quantum dots. If the wavelength of these photons could be converted to 1550 nm, and their quantum state remained unaltered, high quality single photons at 1550 nm would be produced. The process required to achieve this is called quantum frequency conversion.

This thesis describes the principles, setup and results of a quantum frequency conversion experiment. The quantum light is generated from quantum dots embedded in a nano-photonic structure through resonant fluorescence, with wavelengths around 930 nm. The conversion is done by difference frequency generation in waveguides made of periodically poled lithium niobate (PPLN) by applying a pump laser with a wavelength around 2400 nm. The end goal is to have high quality single photons at 1550 nm coupled to an optical fiber.

The focus of my project is to generate a high count rate of pure single photons at 1550 nm. To generate a high count rate it is important to have a high end to end efficiency of the frequency conversion setup, and to have pure photons it is essential to filter out the noise of other light sources from the output fiber. These are the main goals, but given the academic nature of my thesis, I not only focus on them, but also give detailed attention to the secondary physical processes and questions that arise during the experiment. These processes are for example second harmonic generation, anomalies in the conversion spectrum and flaws in the conversion stability.

The main results can be summarized in the following way: an internal conversion efficiency of  $(95 \pm 1)\%$  was achieved, leading to an end to end efficiency of  $(40.9 \pm 0.8)\%$ . With the current quantum dots this allows for photon count rates up to 1.3 MHz with an upper bound for the  $g^{(2)}(0)$  value of  $1.8 \pm 0.1\%$  at 1550 nm. The internal and external efficiency are both the highest recorded to date for difference frequency generation, and the  $g^{(2)}(0)$  value is among the lowest for photons at 1550 nm which are also expected to have a high indistinguishability.

## Acknowledgements

My greatest thanks to my supervisor Prof. Leonardo Middolo and to my co-supervisors Dr. Xiaoyan Zhou and Dr. Beatrice Da Lio. Thank you Leonardo for introducing me to this interesting topic and for being a very supportive and motivating supervisor. Thank you Xiaoyan for teaching everything I know about laboratory work in quantum optics and thank you Beatrice for guiding me and supporting me with so many important details of this work. I should also thank Prof. Peter Lodahl for following closely on my project and for creating a research group where this project was possible. Thanks to all my colleagues at the quantum photonics group for creating a comfortable and motivating research environment. At last thanks to my friends and family for being an essential part of my social life throughout my physics education. Thank you!

## Contents

<b>1</b>	<b>Introduction</b>	<b>1</b>
<b>2</b>	<b>Frequency conversion model</b>	<b>4</b>
2.1	Analytical derivations . . . . .	4
2.2	Simulations and predictions . . . . .	7
2.3	Summary . . . . .	11
<b>3</b>	<b>Experimental setup</b>	<b>12</b>
3.1	Single photon generation and detection . . . . .	12
3.2	PPLN Waveguides . . . . .	14
3.3	Lasers and optical elements . . . . .	14
3.4	Summary . . . . .	20
<b>4</b>	<b>Conversion range and spectrum</b>	<b>22</b>
4.1	Sum frequency generation . . . . .	22
4.2	Spectral asymmetry mystery . . . . .	26
4.3	Summary . . . . .	28
<b>5</b>	<b>Conversion efficiency</b>	<b>30</b>
5.1	Difference frequency generation . . . . .	30
5.2	End to end efficiency optimization . . . . .	33
5.3	Conversion of different sources . . . . .	37
5.4	Summary . . . . .	41
<b>6</b>	<b>Quantum purity</b>	<b>42</b>
6.1	Second harmonic generation . . . . .	42
6.2	Noise filtering . . . . .	44
6.3	Hanbury-Brown and Twiss experiment . . . . .	48
6.4	Summary . . . . .	51
<b>7</b>	<b>Stability and indistinguishability</b>	<b>52</b>
7.1	Efficiency stability . . . . .	52
7.2	Indistinguishability . . . . .	56
7.3	Summary . . . . .	57
<b>8</b>	<b>Concluding remarks and outlook</b>	<b>59</b>
	<b>Bibliography</b>	<b>61</b>
	<b>Appendices</b>	<b>64</b>
<b>A</b>	<b>Practical guides</b>	<b>64</b>
<b>B</b>	<b>Gaussian beam propagation theory</b>	<b>66</b>
<b>C</b>	<b>1550 nm SNSPD and TT characterization</b>	<b>67</b>
<b>D</b>	<b>Possible explanations for the MNLE</b>	<b>69</b>
<b>E</b>	<b>List of abbreviations</b>	<b>75</b>

# 1 Introduction

## Motivation

The world of quantum technologies has opened possibilities to secure communication methods[1], accurate health care imaging [2] and very powerful computing possibilities [3]. An important step in the making of a future filled with quantum devices, is the possibility for such devices to communicate with each other, even at long distances in what is known as the quantum internet. To send quantum information over long distances, the information has to be encoded into photons, since they can be sent in a controlled manner by the use of optical fibers. Due to extremely low losses in these fibers [4], the infrared frequency of 1550 nm is usually the preferred wavelength for long distance telecommunications. To make use of the existing telecommunication networks, it is therefore necessary to be able to produce single photons at 1550 nm.

Single photons are the carriers of quantum information, and can be defined as light that is composed of single photon states, rather than coherent or thermal states. In practice, light that is made of single photon states can be identified by being anti-bunched, which can be measured by a Hanbury-Brown and Twiss experiment [5]. A promising technique to generate single photon states is the use of electron-hole excitations in quantum dots, since they can be accurately controlled to generate one photon at a time. The highest quality quantum dots produced in the quantum photonics group at the Niels Bohr institute emit photons at near infrared (NIR) wavelengths around 930 nm [6][7]. To use these photons for long distance communication, they need to be converted to a wavelength of 1550 nm. There is therefore a need to implement wavelength conversion from NIR to telecom wavelengths with a process that preserves the quantum state of the incoming light. This process and its implementation is denoted as quantum frequency conversion, and will be the main topic of this thesis.

## The Fire-Q project

This work is a part of the Fire-Q project, which stands for Field Ready single-photon quantum technologies. The Fire-Q project is a collaboration effort between different institutions to implement quantum communication protocols using the existing telecommunications network. The first goal of this project is to achieve secure communication between the Technical University of Denmark and the Niels Bohr institute (NBI), by the use of quantum key distribution through public optical fibers. This is illustrated in figure 1.1.

Quantum key distribution (QKD) is an encryption technique that relies on the fact that the quantum state of a particle cannot be measured without being altered, thus making it impossible to spy on a message without altering the content of the message [1]. Applying quantum key distribution experimentally may vary in complexity depending on the protocol that is chosen, but for a simple protocol, it is the simplest example of long distance quantum communication that exists. Therefore achieving quantum key distribution is an important first step in the implementation of more complex quantum communication schemes in the future.

The approach that Fire-Q takes to the implementation of long distance quantum key distribution is to do it with true single photon sources (i.e. quantum dots) instead of weak coherent states, combined with the fact that the photons are sent by the use of the existing telecommunication network, instead of having to install specialized fibers. The purpose of my work is to facilitate these two facts, by converting the single photons emitted from quantum dots, to single photons that are able to travel through public fibers. The process used is difference frequency generation (DFG), which is a non-linear optical process that arises when light of two different wavelengths propagates through a material with a high second order non-linearity, by which light with a frequency equal to the difference between the two incoming frequencies is produced.

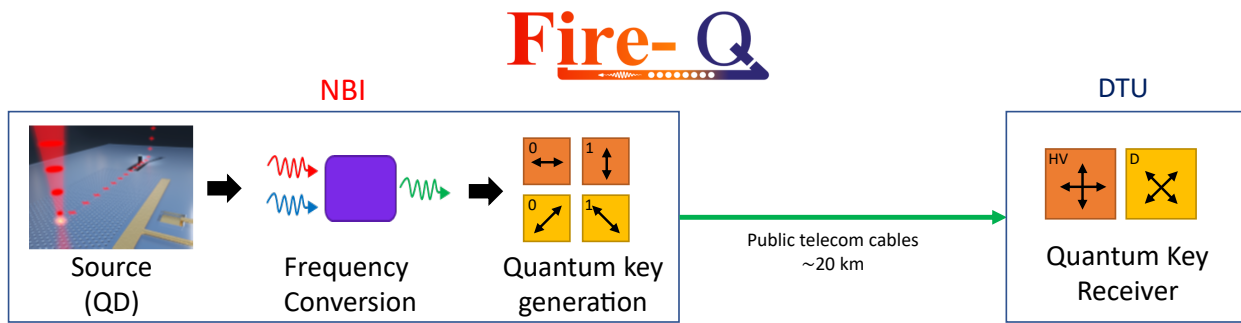


Figure 1.1: Illustration of the main idea of the Fire-Q project, which is to do quantum key distribution using single photons produced with quantum dots and converted to telecom wavelengths through difference frequency generation. The single photons are used to generate a quantum key with polarization encoding, and are decoded after travelling around 20 km through public telecom cables.

## Past work on frequency conversion and QKD

The fact that quantum light could preserve its state through frequency conversion was first suggested in *Optical Letters* in 1990 [8] and measured by Jianming Huang and Prem Kumar [9]. The popularity of quantum frequency conversion grew in turn with the improvement of technologies to fabricate single photon sources, leading to improvements in frequency conversion techniques as well. The fact that anti-bunching is preserved after frequency conversion was first reported in a nature paper by Tanzilli et al. [10], and the preservation of indistinguishability was confirmed seven years later in 2012 [11]. All of these measurements were done with sum frequency generation (SFG), and soon after, the use of difference frequency generation (DFG) as a means to convert light from quantum dots to telecom wavelengths became possible. An effective realization of DFG with the highest internal efficiency reported to date (92%) and a noise-free output light was done by Kambs et al. [12], but they were limited by the quality of their quantum dots, having some bunching and distinguishability. The current benchmark for downconverted photons to telecom wavelengths is by Morrison et al. [13] with an end to end efficiency of <35%, a  $g^{(2)}(0)$  value of 0.04 and an indistinguishability characterized by a Hong-Ou-Mandel (HOM) visibility of 60%.

The concept of QKD was proved for the first time in 1992 in the *Journal of Cryptology* [1], where weak coherent states were exploited as a source of quantum light. Weak coherent states have weaknesses that are not present when true single photon sources are used [14]. Even though these weaknesses can be countered by the use of decoy states [15], the use of true single photon sources imposes a lower complexity of the experimental setup, making it preferable due to its having less potential loopholes [16]. Single photon QKD has been proven to be viable at distances up to 120 km [17], thanks to the fabrication of quantum dots that work directly at 1550 nm, with values of  $g^{(2)}(0)$  that are in the order of  $10^{-3}$ . This is the record for the lowest  $g^{(2)}(0)$  of single photons at 1550 nm. The record for the highest key rate at 20 km is of 26.2 megabits/s [18].

## Goals of Fire-Q and this thesis

The goal of the Fire-Q project is to achieve a key rate in QKD comparable to the current record, at the distance that has been proposed of about 20 km. The goal of this project is to produce the high quality single photons required to realize this vision. A 20 km long optical fiber of telecom wavelengths can expect to have a channel loss of 4 dB [18]. To match the current record of 26.2 megabits/s [18] it is thus necessary to be able to produce count rates above 50 MHz of single photons at 1550 nm. One of the sub-goals of the Fire-Q project is to generate count rates up to 250 MHz directly from the source. At this rate, an end to end conversion efficiency of about 20% would give the desired count

rate at 1550 nm. It is therefore important for the frequency conversion setup to have an end to end efficiency of at least 20%.

Apart from being essential for the Fire-Q project, high quality single photons at 1550 nm also have applications for other long distance quantum communication techniques. It is therefore also a goal of this project to produce single photons at a quality that is comparable or better than the highest quality single photons produced to date. This is a HOM visibility in the range of 60% with a  $g^{(2)}(0)$  value in the range of 0.04. Combining these capabilities with the high count rates generated by the quantum dots at the NBI, will produce state of the art streams of single photons at telecom wavelengths, opening countless possibilities for long range quantum communications in the future.

## Outline of this thesis

The main findings of this thesis are presented through the following chapters:

- **Chapter 2 Frequency conversion model:** The theory behind frequency conversion is introduced. This theory is then used to make simulations of the main experiment of the thesis, which is DFG. The focus of these simulations is to make three predictions. The range of frequencies that can be converted, the allowed bandwidth for the input light and the amount of pump power required to achieve full conversion.
- **Chapter 3 Experimental setup:** The optical components and apparatus used to do frequency conversion of both laser light and single photons are described, as well as what was done to couple the different light beams into the PPLN waveguides, which is further explained in appendix A. Simulations done to optimize the coupling of the pump into the waveguides are also introduced, and the theory behind these simulations is explained in appendix B.
- **Chapter 4 Conversion range and spectrum:** Before doing DFG, the slightly easier to achieve process of sum frequency generation (SFG) was realized. The results of the experiments with SFG are presented in this chapter. These experiments are helpful for characterizing the conversion range and spectrum of the PPLN waveguides when doing DFG, and can be directly compared to the expected values from the simulations in chapter 2. During the experiments with SFG, the conversion spectrum was observed to be asymmetrical around the optimum wavelength. An in depth discussion for the physical cause of this phenomenon is also included in this chapter.
- **Chapter 5 Conversion efficiency:** The main experiment of DFG is presented together with the techniques used to achieve a high internal and external conversion efficiency. The width of the conversion spectrum is found to be very different for SFG than for DFG, and an explanation for this difference is presented. The downconversion process is tested for 3 different sources, a continuous wave (CW) laser, a pulsed laser and single photons, and the resulting conversion efficiency for these sources is presented.
- **Chapter 6 Quantum purity:** It is found that the main sources of impurities in this experiment comes from second harmonic generation (SHG) from the pump, and from photons at the wavelength of the pump itself. The steps taken to filter out the noise produced by these sources are discussed. The results of measuring the purity of the converted light through a Hanbury-Brown and Twist (HBT) experiment are presented, and the errors of this experiment that are intrinsic to the measuring apparatus are discussed in appendix C.
- **Chapter 7 Stability and indistinguishability:** The limiting factors for the stability and indistinguishability of the frequency conversion are discussed and if possible suppressed. The main source of instability is found to be a mysterious non-linear effect (MNLE), which is presented in this chapter and explored in detail in appendix D.

## 2 Frequency conversion model

The main physical process for the purpose of this thesis is three wave mixing, which is when light gets converted between 3 different wavelengths through non-linear optical media. In this chapter the basic theory about three wave mixing is reviewed and then applied to make physical predictions about the experiment.

### 2.1 Analytical derivations

#### Introduction to three wave mixing

When light propagates through a material, its electric and magnetic fields alter the position and motion of the particles of such material. For example in the case of a unidirectional electric field, the response of a material is measured by the polarization density  $P(t)$  and its dependence on the electric field  $E(t)$  can be assumed to be described by a series expansion like in the following equation:

$$P(t) = \epsilon_0 \left[ X^{(1)}E(t) + X^{(2)}E^2(t) + X^{(3)}E^3(t) + \dots \right] = P^{(1)}(t) + P^{(2)}(t) + P^{(3)}(t) + \dots, \quad (2.1)$$

where  $\epsilon_0$  is the vacuum permittivity and the  $X^{(n)}$  terms the  $n$ th order susceptibilities, which are dependent on the direction of propagation, the polarization and the crystal structure of the material. The first term is the linear response, and the rest are the non-linear terms. The linear response accounts for most of the phenomena that can be seen in everyday life, such as refraction and reflection of light through different surfaces. The effects that arise due to the higher order terms are less prominent, and this section will explore the consequences of the second order term, as this will form the underlying theory for all of the frequency conversion phenomena in this thesis.

First, it is beneficial to understand which material properties give rise to a second order response. Any solid with molecules arranged in crystal form will have a periodically repeating electric potential that holds its molecules or atoms trapped in a crystal structure. The repeating part of the potential (basis) can be symmetric or asymmetric around its center, and its shape will determine the  $X^{(n)}$  coefficients of equation 2.1. I will now try to argue that the second order susceptibility can only appear for noncentrosymmetric potentials. The argument will be made from a single classical mechanics perspective in a 1D crystal basis. The potential is generated by a restoration force in the crystal, and This force is assumed to be proportional to the polarization density  $P(t)$  due to Hooke's law. When an electric field interacts with a crystal, it will create a crystal deformation  $\Delta x$  which is linearly proportional to the field strength, so according to equation 2.1 the restoration force is proportional to

$$F \propto X^{(1)}\Delta x + X^{(2)}\Delta x^2 + X^{(3)}\Delta x^3 + \dots \quad (2.2)$$

The potential  $V$  is obtained by integrating the force, which in a simple 1D crystal would be

$$V = \int F dx \propto \frac{1}{2}X^{(1)}\Delta x^2 + \frac{1}{3}X^{(2)}\Delta x^3 + \frac{1}{4}X^{(3)}\Delta x^4 + \dots, \quad (2.3)$$

where it can be seen that the second order susceptibility gives a third order polynomial contribution to the potential, which is an anti-symmetric contribution. This means that if there is a second order susceptibility term, the potential will be noncentrosymmetric.

Now focus will be given to the case of light composed of unidirectional plane waves with 2 frequency components  $\omega_1$  and  $\omega_2$ . The electric field in this case has the form

$$E(t) = E_1 e^{-i\omega_1 t} + E_2 e^{-i\omega_2 t} + E_1^* e^{i\omega_1 t} + E_2^* e^{i\omega_2 t}, \quad (2.4)$$

which is inserted in the second order term of eq. 2.1 to give

$$\begin{aligned}
P^{(2)}(t) &= \epsilon_0 X^{(2)} E^2(t) = \epsilon_0 X^{(2)} [E_1^2 e^{-2i\omega_1 t} + E_1^*{}^2 e^{2i\omega_1 t} + E_2^2 e^{-2i\omega_2 t} + E_2^*{}^2 e^{2i\omega_2 t} \\
&+ 2E_1 E_2 e^{-i(\omega_1 + \omega_2)t} + 2E_1^* E_2^* e^{i(\omega_1 + \omega_2)t} + 2E_1 E_2^* e^{-i(\omega_1 - \omega_2)t} + 2E_1^* E_2 e^{i(\omega_1 - \omega_2)t}] \\
&+ 2\epsilon_0 X^{(2)} [E_1 E_1^* + E_2 E_2^*] .
\end{aligned} \tag{2.5}$$

The resulting expression has many terms, which can be grouped into the following categories: The first four terms describe a process where the resulting electric field has double the frequency of each of the input fields. This is referred to as second harmonic generation (SHG). The fifth and sixth term describe light created with the sum of the input frequencies, in a process called sum frequency generation (SFG). The seventh and eighth terms are the opposite process, where light with the difference of the frequencies is created, thus called difference frequency generation (DFG). These processes are illustrated in figure 2.1. The last two terms create a constant electric field which have no influence on the dynamics of the output field.

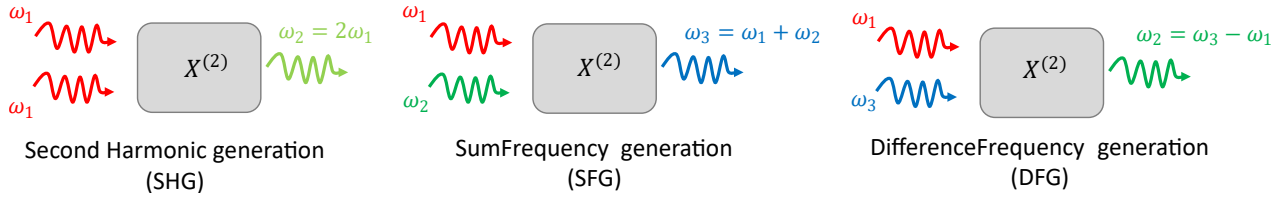


Figure 2.1: Illustration of the three different frequency conversion processes mediated by the second order non-linear susceptibility  $X^{(2)}$

These processes are present in a noncentrosymmetric material, but as shall be later described, not all can be phase matched simultaneously, thus making only some of them relevant for a chosen crystal. The most important process for this thesis is DFG, which can be written as:

$$P^{(2)}(t) = 2\epsilon_0 X^{(2)} E_1 E_2^* e^{-i(\omega_1 - \omega_2)t} + c.c. = 2\epsilon_0 d_{eff} E_1 E_2^* e^{-i(\omega_1 - \omega_2)t} + c.c. , \tag{2.6}$$

where  $X^{(2)}$  is substituted with  $d_{eff}$  to symbolize that it is the effective non-linear susceptibility for the given non-linear process in the chosen direction of propagation.

### Propagation equations

In this subsection the coupled differential equations that govern three wave mixing for light propagating through a waveguide are derived. Such equations will be highly useful for the understanding of many of the experimental phenomena observed throughout this project.

The wave equation for the electric field within a medium is taken as the starting point:

$$\nabla^2 \mathbf{E} - \frac{1}{c^2} \frac{\partial^2}{\partial t^2} \mathbf{E} = \frac{1}{\epsilon_0 c^2} \frac{\partial^2}{\partial t^2} \mathbf{P} . \tag{2.7}$$

In an isotropic material, it is the case that  $\epsilon_0 \mathbf{E} + \mathbf{P}^{(1)} = \mathbf{D} = \epsilon_0 \epsilon \mathbf{E}$ , where  $\epsilon$  which is usually a 3x3 matrix can be approximated as a scalar that is only dependent on the wavelength and temperature. Using this together with equation 2.1 to second order yields

$$\nabla^2 \mathbf{E} - \frac{\epsilon}{c^2} \frac{\partial^2}{\partial t^2} \mathbf{E} = \frac{1}{\epsilon_0 c^2} \frac{\partial^2}{\partial t^2} \mathbf{P}^{(2)} . \tag{2.8}$$

This is a linear second order equation in  $\mathbf{E}$  and  $\mathbf{P}$ , which means that the solution can be assumed to be a superposition of separable solutions of the form  $\mathbf{E}(\mathbf{r}, t) = \sum_i \mathbf{E}_i(\mathbf{r}) \mathbf{E}_i(t)$  and  $\mathbf{P}^{(2)}(\mathbf{r}, t) =$

$\sum_i \mathbf{P}_i^{(2)}(\mathbf{r})\mathbf{P}_i^{(2)}(t)$ . Here the time solutions are taken to be the ones derived in equations 2.4 and 2.6 respectively. Inserting into equation 2.8, it becomes

$$\nabla^2 \mathbf{E}_i(\mathbf{r}) + \frac{\omega_i^2}{c^2} \epsilon(\omega_i) \mathbf{E}_i(\mathbf{r}) = -\frac{\omega_i^2}{\epsilon_0 c^2} \mathbf{P}_i^{(2)}(\mathbf{r}). \quad (2.9)$$

For the spatial part, an assumption is made of it being composed of a fast oscillating term multiplied by a slowly oscillating term. Assuming  $z$  to be the direction of propagation the spatial part can be written as  $E_i(z) = A_i(z)e^{ik_i z}$ . From here on, the  $i$  indexes will be assigned inversely proportional to the wavelength, so  $i = 1$  means  $\lambda \approx 2300$  nm, also called pump wavelength,  $i = 2$  means  $\lambda = 1550$  nm, also called output wavelength and  $i = 3$  means  $\lambda \approx 930$  nm, also called signal wavelength. Attention is now turned into the generation of 1550 nm light in the forward propagating direction, as it is the main task of this thesis. Inserting into eq 2.9 it becomes

$$\left[ \frac{d^2}{dz^2} A_2 + 2ik_2 \frac{dA_2}{dz} - k_2^2 A_2 + \frac{\epsilon(\omega_2)\omega_2^2 A_2}{c^2} \right] e^{ik_2 z} = \frac{-2d_{eff}\omega_2^2}{c^2} A_3 A_1^* e^{i(k_3 - k_1)z}. \quad (2.10)$$

Remembering that  $k_2^2 = \epsilon(\omega_2)\frac{\omega_2^2}{c^2}$  the third and the fourth term in the left hand side cancel each other. The first term can be neglected under the slow change approximation, as it is very little compared to the second term. The equation then finally becomes

$$\frac{d}{dz} A_2 = i \frac{d_{eff}\omega_2}{n_2 c} A_3 A_1^* e^{-i\Delta k z}, \quad (2.11)$$

where

$$\Delta k = k_1 + k_2 - k_3 \quad (2.12)$$

is the phasematching condition. This same derivation can be made for SFG between  $E_1$  and  $E_2$ , yielding the equation

$$\frac{d}{dz} A_3 = i \frac{d_{eff}\omega_3}{n_3 c} A_1 A_2 e^{i\Delta k z}, \quad (2.13)$$

and for DFG between  $E_2$  and  $E_3$  one gets

$$\frac{d}{dz} A_1 = i \frac{d_{eff}\omega_1}{n_1 c} A_3 A_2^* e^{-i\Delta k z}. \quad (2.14)$$

Equations 2.11, 2.13 and 2.14, are the main equations governing the three wave mixing process that will be essential for this thesis.

To calculate the power given the electric field amplitude  $A_i$ , the following equation can be applied

$$P_i = \frac{c\epsilon_0 n_i}{2} S \langle E_n \rangle^2 = \frac{c\epsilon_0 n_i}{2} S |A_n|^2. \quad (2.15)$$

where  $S$  is the mode overlap area inside the waveguide between the  $E_1$  and  $E_3$  modes.

### Solution under the strong pump approximation

The propagation equations 2.11, 2.13 and 2.14 can be simplified by introducing the quantity:

$$a_i = \sqrt{\frac{n_i S}{2\mu_0 c \hbar \omega_i}} A_i. \quad (2.16)$$

Physically this quantity is approximately equal to the square root of the photon number expectation value for a given waveguide mode, but this is not relevant here as its only purpose is to simplify the calculations. The equation for calculating the power becomes

$$P_i = \hbar \omega_i |a_i|^2, \quad (2.17)$$

and the propagation equations in terms of this quantity become

$$\begin{aligned}\frac{da_1}{dz} &= i\gamma_0 a_2^* a_3 e^{-i\Delta k z}, \\ \frac{da_2}{dz} &= i\gamma_0 a_1^* a_3 e^{-i\Delta k z}, \\ \frac{da_3}{dz} &= i\gamma_0 a_1 a_2 e^{i\Delta k z},\end{aligned}\tag{2.18}$$

with

$$\gamma_0 = \sqrt{\frac{2\hbar\mu_0\omega_1\omega_2\omega_3}{S n_1 n_2 n_3 c}} d_{eff}.\tag{2.19}$$

The system of differential equations is now simpler than before rewriting it, as all of the individual equations share the same prefactor of  $\gamma$  on the right hand side. All of the simulations done in this and the following chapters are based on numerical integration of these equations, but a simplified analytical solution will be presented before introducing the simulations. Solving these equations for an arbitrary value of  $\Delta k$  is a complicated task and will not be pursued in this thesis. But as will be discussed in the next section, in practice it is always possible to tune the experiment such that  $\Delta k = 0$ , so it can be assumed to be zero. Another reasonable assumption is the so called strong pump approximation, which states that the value of  $a_1$  changes very little compared to its size, such that  $\frac{da_1}{dz} = 0$  and  $a_1(z)$  is a constant. Under these assumptions, equation 2.18 can be rewritten as

$$\begin{aligned}\frac{d^2 a_2}{dz^2} &= -\gamma^2 |a_1|^2 a_2, \\ \frac{d^2 a_3}{dz^2} &= -\gamma^2 |a_1|^2 a_3,\end{aligned}\tag{2.20}$$

which are simple harmonic oscillator equations, and given the start condition that  $a_2(0) = 0$ , the solution becomes:

$$\begin{aligned}a_2(z) &= a_3(0) \sin(\gamma |a_1| z), \\ a_3(z) &= a_3(0) \cos(\gamma |a_1| z).\end{aligned}\tag{2.21}$$

This solution will be useful when doing experiments, as it can be used to make predictions of how much converted power can be expected with a given pump power.

## 2.2 Simulations and predictions

### Phase matching

In this section a numerical solution to the propagation equations in 2.18 is described and used to discuss the necessary conditions to achieve constructive frequency conversion. These numerical solutions will be useful to explain many of the complex phenomena that will be described in later chapters, for which an analytical approach would be impossible.

The simulations are based on numerical integration of the differential equations 2.18. For the integration method I tried using both the Euler integration method and the Runge-Kutta 4th order (RK4) method. Even though the RK4 method should in general be more effective for a given step size, for this specific problem the difference proved to be negligible. I chose therefore to use the Euler method since it requires less computations per step. To do the simulation, the values for the effective mode index  $n_i$  and  $d_{eff}$  are required. The value of  $d_{eff}$  for this specific process was not found in the literature. In Schiek et al [19], it is measured for SHG of 1.52  $\mu\text{m}$  light to be  $20.6 \pm 2.1 \frac{\text{pm}}{\text{V}}$ . This is the closest I have found to the wavelengths of this work, and I therefore assume the value to be  $20 \frac{\text{pm}}{\text{V}}$  in my

simulations. The method for calculating the effective mode index is presented in the next subsection. If the non-linear susceptibility  $d_{eff}$  is assumed to be constant as the black line in figure 2.2a, the result of the simulation is the black line 2.2b. This shows that the converted power oscillates periodically with a very small amplitude. This is due to bad phase matching, which physically means that the electric fields create DFG when they are in phase but SFG when they are out of phase, converting and then backconverting periodically, making it impossible to produce a significant amplitude of DFG.

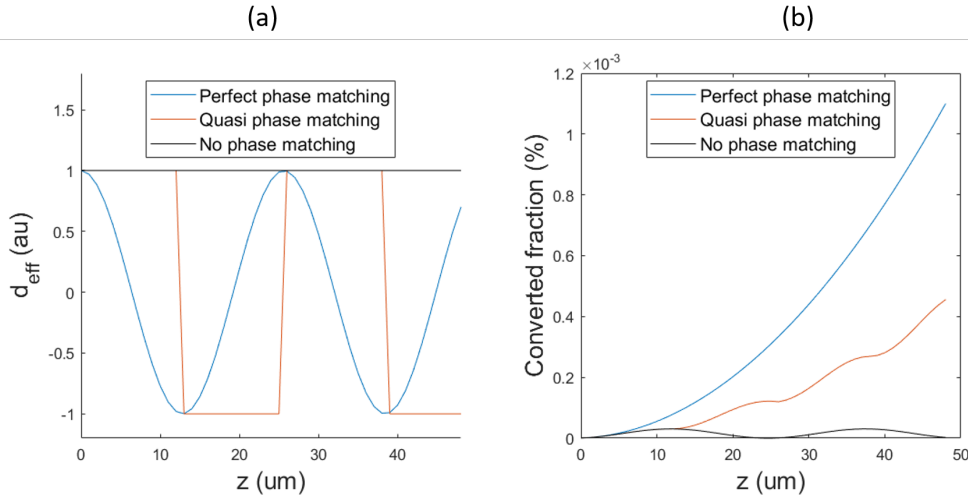


Figure 2.2: (a) Illustration of the spatial dependence of  $d_{eff}$  for the three phase matching models. (b) Converted frequency propagation for different phase matching techniques according to simulation. The pump power in the waveguide is 6mW, the phase matching condition  $\Delta k$  is assumed to be zero.

The phase mismatch is described by equation 2.12, which for an arbitrary material will in general be non-zero. When this quantity is close to zero, the three waves will be mostly in phase, and completely in phase if it equals zero. To achieve efficient frequency conversion it is therefore necessary to engineer a crystal where  $\Delta k = 0$ , which maximizes the non-linear process. The ideal would be a crystal where  $X^{(2)}$  had a sinusoidal spatial oscillation with exactly the same wavelength as the phase mismatch periodicity as illustrated with the blue line in figure 2.2a. This is equivalent to adding the following modification to the  $\Delta k$  equation:

$$\Delta k = k_1 + k_2 - k_3 + \frac{2\pi}{\Lambda}, \quad (2.22)$$

where  $\Lambda$  is the oscillation period of the crystal. The blue curve in figure 2.2b is the simulation result for perfect phase matching which is where  $\Lambda$  is set such that  $\Delta k = 0$ .

In practice it is very hard to engineer a crystal with a sinusoidal oscillation of the non-linear polarizability, but something close to it can be achieved. If  $X^{(2)}$  is periodically poled instead, as illustrated by the red curve in figure 2.2a, constructive frequency conversion can still be achieved. This is called quasi-phase matching, which is made possible by modern fabrication techniques. The frequency conversion result can be seen in the red curve of figure 2.2b.

### Conversion efficiency and bandwidth

Finally it is possible to apply the model described through this chapter using the actual parameters from the experimental setup, with the aim to estimate the values that should be expected in the following chapters.

Within this frequency conversion experiment, a key figure of merit is the efficiency, which is, what fraction of the incoming 930 nm photons that gets converted to 1550 nm photons. This value depends on the propagation distance, the pump power inside the waveguide and the phase matching condition

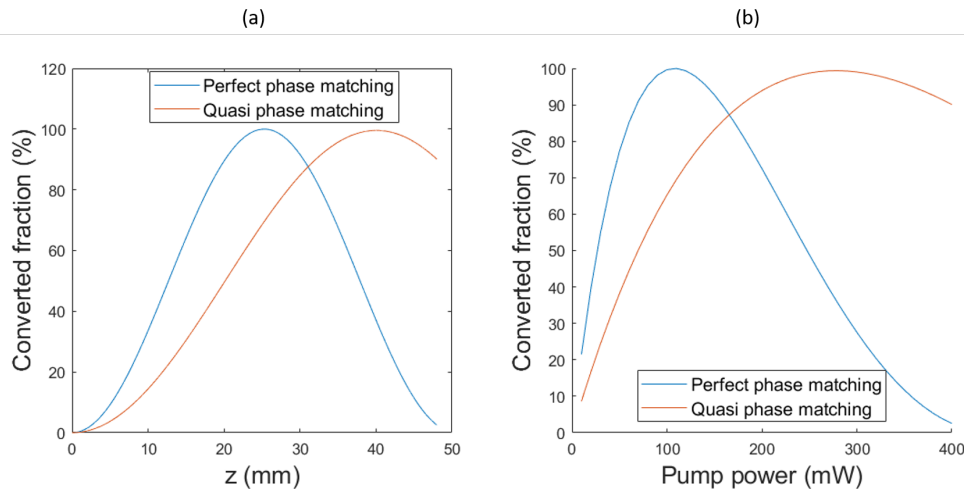


Figure 2.3: (a) Conversion efficiency as a function of propagation distance. Pump power in the waveguide is 400 mW. (b) Conversion efficiency as a function of the pump power, waveguide distance is 48 mm. In both cases  $\Delta k = 0$

$\Delta k$ . The length of the waveguides used in the experiment is 48 mm, which cannot be changed and thus all of the following simulations will be done at this propagation length. The pump power inside the waveguide can be easily controlled experimentally and is described in the next chapter. The phase matching condition is dependent on the wavelengths, the refractive indexes and the structure of the non-linear susceptibility.  $\Delta k$  can be controlled experimentally in several ways, but a key aspect is that it is always possible to make it very close to zero. A simulation for the dependence on the distance and pump power can be seen in figure 2.3a and 2.3b. These same plots can be obtained using the analytical solution expressed in equation 2.21 as long as the pump power is very high compared to the power of the incoming 930 nm light. I tried plotting both the analytical and simulated solutions on together and confirmed that they overlapped almost perfectly. This can be taken as a validation that the simulations are done correctly.

The figures show that quasi phase matching is less efficient than perfect phase matching, but given a large enough pump power or a sufficiently long distance, quasi phase matching will achieve full conversion just as perfect phase matching. By varying the value of  $d_{eff}$  I observed that quasi phase matching becomes equal to perfect phase matching if  $d_{eff} \rightarrow \frac{2}{\pi}d_{eff}$ . It can be seen from figure 2.3b that for the physical parameters of my experiment full internal conversion should be achieved for a pump power in the waveguide around 280 mW.

Another desired prediction is the conversion bandwidth, which is how broad a spectrum of the 930 nm photons can be expected to be converted to 1550 nm photons. This requires a more detailed study of the phase matching condition and its influence on the conversion efficiency. Experimentally, the wavelength of the signal light is fixed, together with the telecom wavelength thus  $\lambda_3$  and  $\lambda_2$  cannot be controlled, but the wavelength of the pump  $\lambda_1$  can be controlled with great accuracy. The poling period can be chosen between 6 different possible values. Furthermore the refractive indexes are all dependent on the temperature, which can also be tuned in the experiment, giving an extra degree of freedom in the control of  $\Delta k$ .

The bandwidth is determined by the wavelength dependence of the phasematching condition 2.22. This condition will be important for many discussions, so it should be examined in detail. The wavevector  $k$  depends on the refractive index, which in a waveguide is not simply the refractive index of the material, but instead adopts a value that is in between that of the waveguide material and its surrounding materials. This is called the effective mode index, and it depends on many factors such

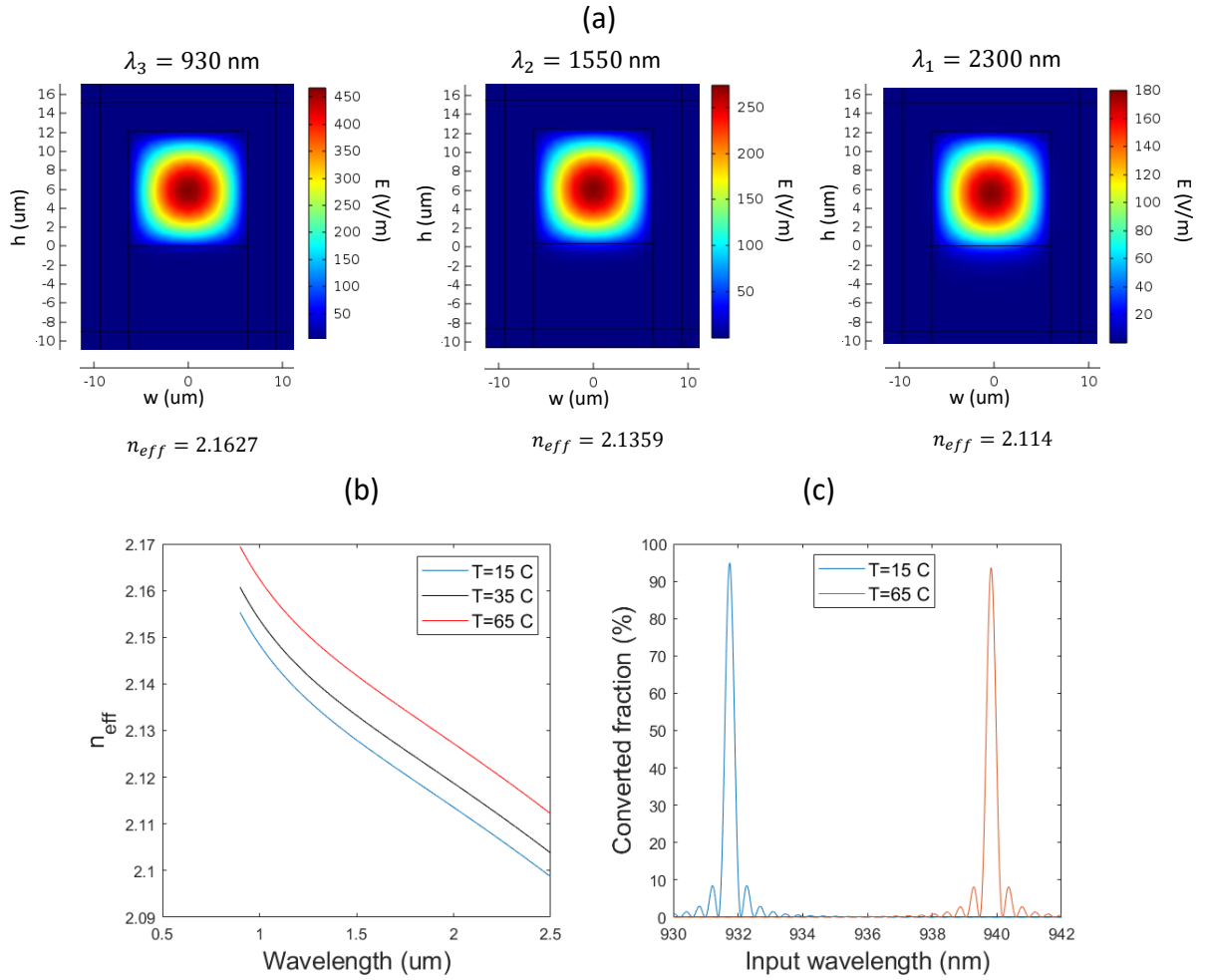


Figure 2.4: (a) Comsol simulation of waveguide mode for different wavelengths, temperature is set to 50  $^{\circ}\text{C}$ . (b) Effective mode index for different wavelengths and temperature obtained from Comsol simulation. (c) Conversion efficiency as a function of input wavelength. Pump power in the waveguide is 150 mW and the pump wavelength is set to 2337 nm. Poling period of 26.17  $\mu\text{m}$ .

as the free space wavelength  $\lambda$ , temperature  $T$ , width  $w$  and height  $h$  of the waveguide. Keeping this in mind, the phasematching condition becomes

$$\Delta k = \frac{2\pi n_{eff}(\lambda_1, T, h, w)}{\lambda_1} + \frac{2\pi n_{eff}(\lambda_2, T, h, w)}{\lambda_2} + \frac{2\pi n_{eff}(\lambda_3, T, h, w)}{\lambda_3} + \frac{2\pi}{\Lambda} \quad (2.23)$$

To make predictions about the bandwidth it is necessary to know the effective mode indexes inside the waveguides for all of the wavelengths and temperatures that are present in this experiment. I calculated these indexes using Comsol Multiphysics, which is a finite element method simulation program. Here I introduced the boundary conditions and the material properties of the waveguides in this experiment, thus allowing the program to calculate the mode profile for each wavelength and its correspondent effective mode index. The specifications used for the waveguides are described in the next chapter. An illustration of some of the modes can be seen in figure 2.4a, and the plot over the complete region for the effective mode indexes is in figure 2.4b. The two temperatures chosen for demonstration are the two extreme values for the temperature achievable by the temperature controlling apparatus in the experimental setup, which will be described in chapter 3.

Having calculated the effective mode index, the conversion bandwidth can be simulated. The result can be seen in figure 2.4b, where  $\lambda_1$  is kept constant and the value of  $\lambda_3$  is scanned. The curves look similar to sinc functions with a high peak for  $\Delta k = 0$  and many small peaks nearby. By energy conservation the value of  $\lambda_2$  will also change, so the output wavelength is only 1550 nm at the top of the blue peak. The figure shows that within the temperature tunability range of the experiment the conversion range is expected to be 8 nm for a fixed poling period. In the figure the output wavelength is not represented, but from energy conservation the output wavelength range can be calculated to be 19 nm for the same temperature span. This is luckily not a problem as the output wavelength can be freely tuned and always set to be 1550 nm because  $\lambda_1$  which is the wavelength of the pump can be changed, and again by energy conservation  $\lambda_2$  will change as well. The thermal expansion of the waveguide in the direction of propagation is also taken into account, as it slightly shifts the poling period. The thermal expansion in this temperature range is in the order of 0.05% of the length of the waveguides  $L$ , which results in a phase matched wavelength shift of 0.5 nm in the 930 nm region.

For this thesis, the conversion bandwidth of the DFG will be defined as the full width half maximum (FWHM) of the converted curve if the wavelength at the 930 nm range is scanned with constant temperature and output wavelength of 1550 nm. The curve obtained by such a scan will be referred to as the conversion spectrum. The expected conversion bandwidth can be extracted from the FWHM of the main peak of one of the curves in figure 2.4c. This is read to be  $\Delta\lambda = 0.35$  nm, which in the frequency domain is  $\Delta\nu = 120$  GHz. Doing the same simulation for a different value of the poling period changes the optimal phasematching wavelength, but other factors as the tunability range and the bandwidth are almost completely unchanged.

So far frequency conversion has only been explored in the classical regime, where the quantum states of the input and output light were irrelevant. The fact that the quantum state of the input light is preserved after frequency conversion is not trivial, but it will not be derived in this thesis. A discussion about this topic can be found in the groundbreaking article by Prem Kumar on quantum frequency conversion [8]. The argument given is that so long as the pump light at  $\omega_1$  is undepleted (strong pump approximation), its quantum state will not affect the state of the output light at  $\omega_2$ , which will therefore only be dependent on the state of the signal light at  $\omega_3$ . If the signal light is therefore composed of single photon states, and the pump power is much stronger than the signal (around 12 orders of magnitude in this case), the converted light will be composed of single photon states.

## 2.3 Summary

In the first part of this section, the definition of the second order non-linear coefficient was applied together with Maxwell's equations to derive the propagation equations for three wave mixing. These are written in equation 2.18. The propagation equations were then used as a basis for numerical simulations of the DFG process that is expected to happen in the main experiment. By doing the simulation it was found that the phasematching condition in equation 2.23 needed to be very close to zero for the conversion to be efficient. This is experimentally achievable through quasi-phasematching, and it was found that even though quasi-phase matching reduces the conversion efficiency compared to perfect phase matching, given enough pump power or propagation distance, total conversion can still be achieved. With a fixed propagation length of 48 mm, the simulations predict that full conversion can be achieved if the pump power inside the waveguides is of 280 mW. Another prediction is that a single PPLN waveguide in the temperature span from 15 to 65 °C can convert NIR light within a range of 8 nm. The conversion bandwidth is of  $\Delta\lambda = 0.35$  nm

### 3 Experimental setup

In this chapter I will describe the experimental setup used to achieve frequency conversion. In order to optimize the conversion efficiency and stability, I have made many changes and improvements to the setup. This chapter describes the original design of the setup, while the changes and improvements will be described in the following chapters.

The goal is to take single photons coming from a quantum dot with a wavelength in the range of 910 to 950 nm, do difference frequency generation (DFG) and collect the converted photons at 1550 nm. This is done in a free space setup due to low losses for all of the wavelengths and easy polarization control. A sketch of the most important parts of this free space setup can be seen in figure 3.1. The light from the quantum dot is transported with an optical fiber to the table where this experiment is located. Simultaneously a very strong pump field in the range of 2.0 to 2.5  $\mu\text{m}$  is required which is obtained by placing a tunable laser at this range from the company IPG photonics in the same table as the setup. The two wavelengths are combined by the use of a dichroic mirror which is custom designed for both ranges of wavelengths. The two beams of light are focused by an aspherical lens into very narrow waveguides.

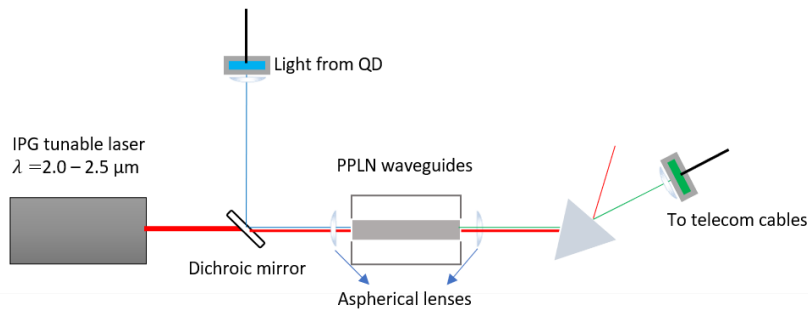


Figure 3.1: Illustration of the main components in the experiment. QD: quantum dot, PPLN: periodically poled lithium niobate

The waveguides are made of periodically poled lithium niobate and have a length of 48 mm and cross dimensions of about  $12 \times 12 \mu\text{m}^2$ . There are 12 different waveguides with poling periods in the range of 24.5 to 26.0  $\mu\text{m}$ . A similar aspherical lens as the one for the input is necessary to collimate the beam after the output of the waveguide. The 1550 nm light is then separated from the pump light by using a prism. The desired beam, i.e. the converted single photons at 1550 nm, are then coupled into a fiber output. After being in a fiber and at the telecom wavelength, the single photons are ready for applications in long distance quantum communication.

#### 3.1 Single photon generation and detection

##### Quantum dots

For this experiment, InGaAs quantum dots embedded in GaAs nanostructures are used. The experimental procedure to produce and collect highly anti-bunched and indistinguishable photons using these quantum dots is part of an extensive topic and was not part of my work. Luckily exactly such a setup was available, which is described in detail in the PhD thesis by Pedersen [20]. By connecting to the quantum dot setup, high quality single photons were available for frequency conversion. In this subsection I will briefly describe the practical considerations that are necessary when using the single photons from the quantum dots setup.

In the setup, quantum dots are excited from top (normal to the planar structure) and because of the design of the photonic crystal most of the single photons will be sent in a predetermined direction

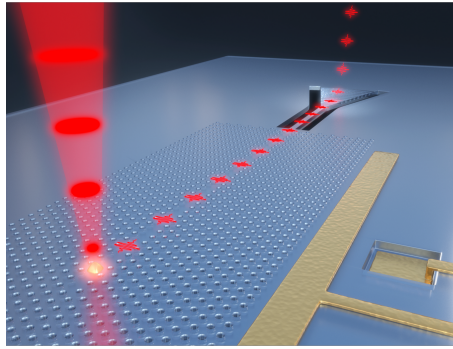


Figure 3.2: Illustration of the resonant fluorescence technique for single photon generation. Figure taken from the Science Advances paper by Uppu et al. [7].

and coupled out to a fiber through a grating. The quantum dot is excited by a pulsed laser which is almost perpendicular to the crystal, at an angle that minimizes the chance that the laser light will be collected by the crystal. This is called resonance fluorescence and is illustrated in figure 3.2. Given the right pulse duration, laser power and beam alignment, the laser light will induce a  $\pi/2$  Rabi rotation of the atomic state if the voltage given to the dot is in the correct range for single exciton operation. To ensure the highest quality and count rate of single photons coming from the quantum dot, it is therefore necessary to have the optimal voltage and the optimal pump power from the laser, as well as having optimized the alignment of the incident beam. The alignment of the beam should be stable and unnecessary to optimize from day to day. The indicator to check if realignment is necessary is the extinction ratio coming from shifting the voltage given to the quantum dot. The extinction ratio is calculated as the counts measured with the voltage set into the right range, divided by the counts measured with the voltage set away from this range. If the extinction ratio is easily above 200 it is a good indication that realignment is not necessary. On the other hand if it is below 100, realignment is necessary. The most likely reason for the alignment to drift away is temperature instabilities in the optical table, so if the extinction rate is low one should begin by checking the temperature control system.

The voltage and power should be optimized before taking any long measurements with the quantum dots, as the optimal value might slightly drift during a day. To do so one should do a voltage scan with a fixed pump power, and a laser power scan with a fixed voltage. From the scan, the optimal value can be found by fitting the corresponding curve with the expected function, and set the corresponding physical value to the fitted value. More details about these scans and their desired curves can be found in Uppu et al. [7].

### Single photon detectors

To detect the generated 930 nm and the converted 1550 nm photons, superconducting-nanowire single photon detectors (SNSPDs) were used. The 930 nm detectors had been used regularly by other members of the group, which meant that their required bias current and their detection efficiency had been determined. On the other hand, the 1550 nm detectors had never been used, and I had to characterize them.

The SNSPDs can maximally measure about 2 million photon counts per second. This means that to characterize them using a regular laser, a significant amount of attenuation is necessary. The setup used for characterizing the SNSPDs is illustrated in figure 3.3. If the input power and the and the transmission through all of the attenuating components is known, the detector efficiency is obtained by dividing the measured photon number by the expected photon number. I found that the 1550 nm SNSPDs require a bias current of about -17 mA before they reach their peak efficiency, if using a

PicoHarp time tagger. The measured efficiency is  $62 \pm 3\%$  for detector A2 and  $50 \pm 15\%$  for detector A1, where the later is quite unstable and therefore has a very varying efficiency.

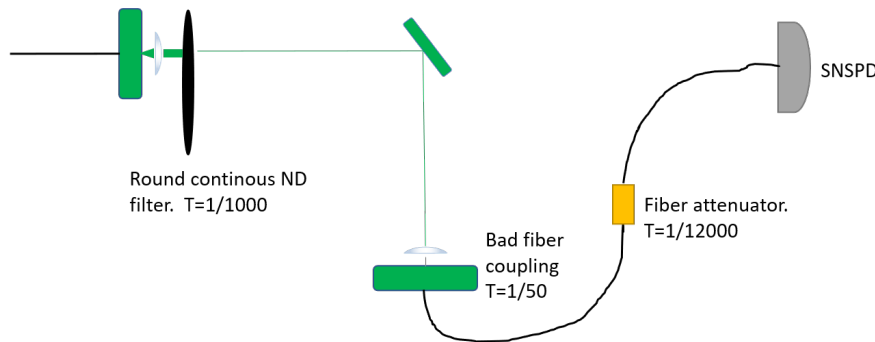


Figure 3.3: Setup for characterizing the SNSPDs. ND: Neutral density

### 3.2 PPLN Waveguides

The main element in this frequency conversion experiment are the periodically polled lithium niobate waveguides (PPLN), as the three wave mixing process happens inside of them. The waveguides are all on a chip which is mounted on a stage as can be seen in figure 3.4a. The vertical and horizontal position of the waveguides can be controlled precisely using the stage in which they are mounted. This allows for easier coupling and quick change of the operating waveguide once the setup is aligned. The lenses can also be precisely controlled in all directions. Once aligned, the Y and Z positions are fixed, but the X positions, which define the focal point of input and output beams, can change from day to day, and are constantly being optimized for better coupling. Inside the chip there are waveguides with 6 different poling periods and are arranged such that there are two waveguides for each poling period, as can be seen in figure 3.4b.

A direct picture of a group of waveguides taken by the camera in the setup can be seen in figure 3.4c, as well as the dimensions of the waveguides. The only difference between two waveguides in a group is their width. The odd numbers have width  $12.7\mu\text{m}$  and the even numbers have width  $12.6\mu\text{m}$ , which, as will be discussed in chapter 4, has an influence on the phasematched wavelength. The waveguides are embedded with an anti-reflection (AR) coating, specially designed to maximize transmission at the wavelengths that are relevant for this experiment. A simulation of the reflectivity spectrum of this coating can be seen in figure 3.4d. This simulation was done by the manufacturer of the waveguides. The bulk material in which the waveguides are mounted has a built-in electrical thermistor connection, which allows for temperature control. The installed temperature controller can give temperatures in the range on 15-65 °C and has a precision of 0.1 °C. The temperature of the waveguides cannot be controlled directly, as their temperature will be dependent both on the bulk temperature and the room temperature. This might give rise to slight oscillations in the phase matched wavelength, due to oscillations in room temperature. To minimize this effect, and to protect the waveguides from dust particles, I built an acrylic box that covers the whole stage where the waveguides are mounted.

### 3.3 Lasers and optical elements

#### Signal input paths

The input paths are the optical elements that couple the light coming from the fibers into the waveguide. There are two input paths, the 930 nm path for doing DFG and the 1550 nm path for doing sum frequency generation (SFG). This subsection is a brief description of the optical elements and general remarks on how to align both paths. The most important path is the 930 nm path, which is

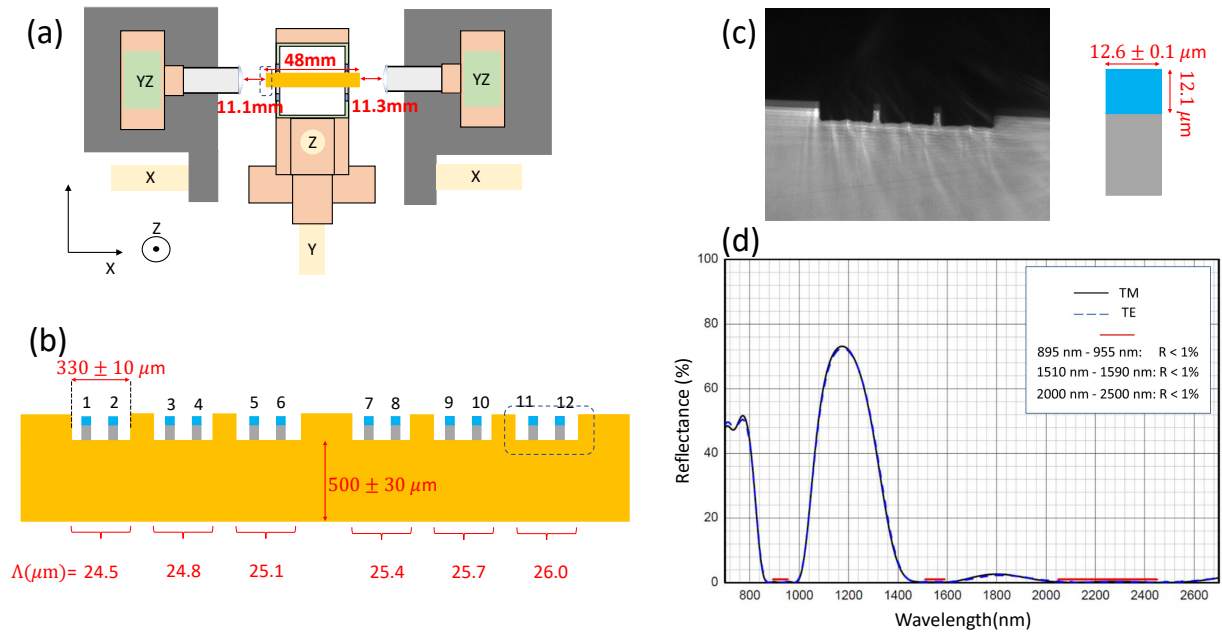


Figure 3.4: (a) Stages in which the waveguides and the aspherical lenses are mounted. The letters X, Y and Z represent the places where the translation screw for the given direction is located. (b) Schematic front view of the waveguides with their poling periods and chip dimensions specified. (c) (Left) Camera picture of waveguides 11 and 12. (Right) Height and width dimensions of the waveguides. (d) Simulation of the AR coating reflectivity spectrum measured by NTT electronics corporation, the manufacturer of the waveguides. The red lines mark the regions relevant for this experiment.

the blue path in figure 3.5a. As usual there is a collimator lens as the first element after a fiber, and two mirrors for precise beam control. For frequency conversion in the waveguides of this experiment the light has to be linear and S polarized, which is the polarization required to couple into the TM mode of the waveguides. Therefore there are two waveplates used for polarization control. The light is then reflected by the dichroic mirror, which is represented in white and has above 99% reflectivity for 930 nm S polarized light. The entire transmission and reflection spectrum of the dichroic mirror can be seen in figure 3.5b. Lastly the beam is focused into the waveguide by an aspherical lens with focal length  $f = 11.0$  mm, which is mounted in a high precision translation mount to create the correct distance between the lens and the waveguide. The distance is not exactly 11 mm but 11.125 mm due to wavelength focal shift. The focal length was chosen such that the beam size at the focal point is close to the simulated mode size in the waveguide for the 930 nm mode.

A 1550 nm fiber coupled diode laser is installed directly on the setup. The actual wavelength of this laser has not been measured, but according to its specifications it should be between 1549 and 1551 nm. Its purpose is to do SFG, which, as will be seen in the next chapter, is an important aid to create DFG. The path of this laser is illustrated by the green lines in figure 3.5a. The fiber out-coupler uses a mount that allows to adjust the position of the beam as if it was a mirror mount, resulting in the path having effectively two mirrors. There is also a half wave plate to control the polarization, which should be the same as the polarization for the 930 nm beam. A quarter waveplate could improve the polarization further, but since there is no need to achieve high efficiency for SFG it was not included in the setup. The path is then coupled to the rest of the setup by using a beam splitter on a deployable mount. The beamsplitter is only on the path when doing SFG. An infrared detection camera was also used, and was an important tool for aligning the beam into the desired waveguide.

To produce SFG and DFG it is important that the modes inside of the waveguides are singlemoded,

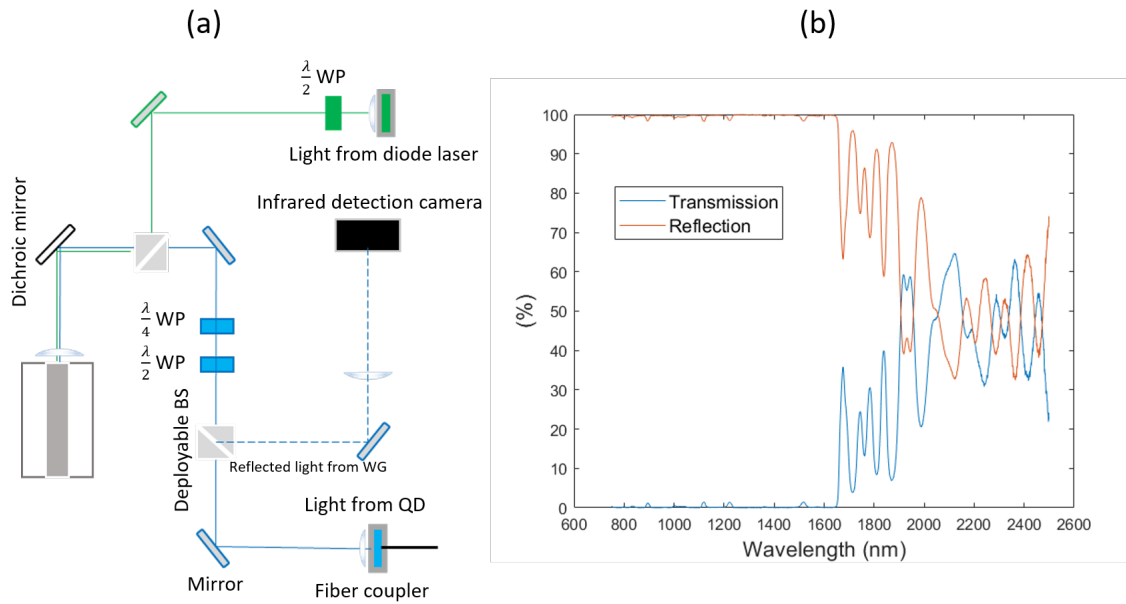


Figure 3.5: (a) Optical elements in the 930 and 1550 nm input paths. The camera and the first beamsplitter are only used for alignment purposes. WP: waveplate, BS: beamsplitter (b) Transmission and reflection spectrum of the dichroic mirror for S-polarized light. (figure made from the data available by the manufacturer at their homepage).

which requires that the incoming light is centered and parallel with the waveguides. At 930 nm it may prove to be a challenge to couple the light such that it is single moded, as there are many possible high order modes in the waveguides at this wavelength, and they are very easy to excite. I have made a step by step guide to the way I recommend the coupling to be made, which can be seen in appendix A. Further suggestions to how to improve the coupling will come in chapter 5. The 1550 nm light does not have as many high order modes in the waveguides and they are not so easily excited. The challenge when coupling this one is that it cannot be detected by the camera. My suggestions as to how to couple it can be seen in appendix A

### Pump laser

This subsection contains some important details about the pump laser that is used, as well as an explanation of the optical elements and the alignment procedure needed to couple the pump into the waveguides.

The laser used is CW with a tunability range from 2.0 to 2.5  $\mu\text{m}$  and a specified maximal output power of 4.5W at 2.3  $\mu\text{m}$ . Laser operation is achieved by a secondary pump laser of 20W operating at 1567 nm. The wavelength of the laser is determined by the position of a stepper motor which is built directly into the laser cavity, and can be controlled using its usb connection to a computer. Precise tuning of the wavelength can be achieved by 3 piezos also built into the cavity and controllable by the same usb connection. More details about the piezos can be found in the manual of the laser.

According to the manufacturer the laser can achieve longitudinal single mode operation for any wavelength in the given range. But setting the stepper motor to the right position is not enough. A scan of the pump power as a function of the stepper motor position can be seen in figure 3.6a, where it is clear that the power oscillates by about 20% depending on the position. This is because for many positions the cavity is multimoded longitudinally, resulting in less effective laser operation. This is confirmed by a measurement taken by the manufacturer which can be seen in figure 3.6b, where a

Fabry Perrot cavity is scanned to determine the different frequency components of the laser, showing that for a certain detuning of piezo 3, the laser has two mode operation. To achieve single mode operation for a given wavelength, piezo 3 has to be tuned such that the power output of the laser is maximised.

Unfortunately, during the time I did the experiment the laser never met the specifications for the maximal output power. It could maximally give 3W at a wavelength of 2300 nm, and only 2.4W at a wavelength of 2400 nm, which is the wavelength that was used for most of the experiments. Another problem was that only piezo 3 was actually controllable, while the other 2 could not be moved.

The optical elements in the path of the pump beam can be seen in figure 3.6c. First there is a Faraday isolator, which is an element that allows only propagation in one direction. Its purpose is to avoid damage of the laser due to back reflections. The power of the laser that goes into the setup is controlled by a half waveplate and a polarizing beamsplitter, because changing the power output directly from the laser makes it unstable. The polarization is controlled by two waveplates, and should be set to be linear in the S polarization, such that it couples into the TM mode of the waveguides. There are four mirrors in the path, where the first two are used to center the beam into all of the pump path optics, and the last two are used to couple the beam into the waveguide. In principle, this is all of the optics that are needed to couple the pump into the waveguide, but given that the aspherical lens is chosen to be the optimal to couple a wavelength of 930 nm, it will not be optimal at 2300 nm. This is because the beam width at the focal point is both dependent on the beam width before the lens and the wavelength of the light. Both beams have roughly the same beam width, which is about 1.5 mm, but very different wavelengths. To account for the wavelength difference a larger beam size for the pump is needed, and thus a beam magnifier is installed. The beam magnifier is made of two lenses, the first with focal length  $f = -40$  mm lens and the second with  $f = 100$  mm, giving a magnification of  $M = 2.5$ .

According to the Comsol simulation, light at  $2.3 \mu\text{m}$  has only two possible TM modes carried in the waveguides: The fundamental zeroth order mode, and a very lossy, very hard to excite first order mode. This means that the pump light coupled into the waveguide will almost always be singlemoded with the desired zeroth order mode. Nonetheless, the pump proves to be the hardest one to couple of all of the three wavelengths. This is because it cannot be detected with fluorescent detector cards, and the only way to spot it is to use thermal detector cards, which are very slow and unreliable. My practical suggestions for how to couple this path into the waveguide by the help of a visible light laser can be seen in appendix A.

### Pump coupling optimization

The aspherical lens placed before the waveguide has a different focal distance for 930 nm than for 2300 nm. In the original design of the setup, which is described in the subsection above, this effect was assumed to be negligible. Doing the experiment I quickly found that this was not the case, which meant that when the aspherical lens was optimized to couple the 930 nm light, the 2300 nm light would be poorly coupled, even if it was perfectly centered. This subsection contains a discussion of how to deal with this issue from simulations and experiments that I have made.

The field of the pump laser is that of a free space propagating gaussian beam, and thus I have applied gaussian beam propagation theory to simulate the beam width and curvature through the path followed by the pump. Then the overlap integral between the resulting beamfront and the mode in the waveguide is calculated to determine the coupling efficiency. The underlying equations for the simulation are described in appendix B. For the simulation to be accurate, it is necessary to know the beam width and the focal length of the aspherical lens. The first one can be between 1 mm and 2.5 mm according to the laser manufacturer. I measured it to be  $w = 1.8 \pm 0.3$  mm. The focal length at 2300 nm for this aspherical lens has not been measured by the manufacturer. I measured it to be  $f = 11.46 \pm 0.08$  mm by maximizing the transmitted power through the waveguide.

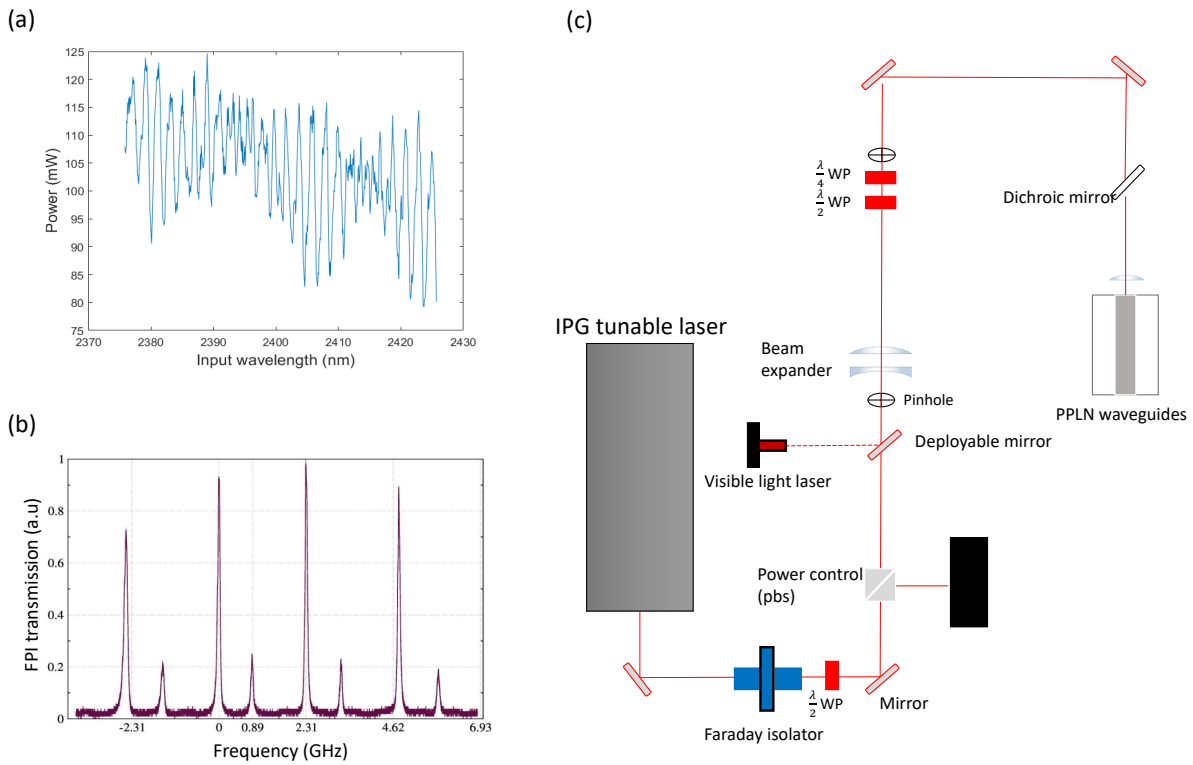


Figure 3.6: (a) Power spectrum at a selected wavelength region, scanning the stepper motor of the laser and measuring with a power meter the optical power at each wavelength position. The power is measured after the attenuation with the pbs. (b) Fabri perot interference of the pump laser at a fixed wavelength with a slight detuning piezo 3. (figure taken from the laser manual of the laser made by IPG photonics) (c) Optical elements in the path of the pump laser. The visible light laser and the pinholes are only used for alignment.

The parameters available for this optimization are the positions and the focal lengths of all the lenses, as well as the possibility to introduce extra lenses. The position and focal length of the aspherical lens were fixed, as it optimized the 930 coupling. The focal lengths of the lenses in the beam expander were also fixed, as it would have been expensive to buy new ones. On the other hand the distance between the lenses, which is 60 mm for a collimated beam, does not need to be fixed, as a slightly non-collimated beam might actually couple better into the waveguides. Doing some quick test simulations I also found that introducing any lens with a focal length below 1000 mm would introduce a divergence of the beam too big for it to couple into the waveguide. As 1000 mm is the largest focal length that is commercially available at this wavelength, the focal length of an eventual extra lens is therefore fixed to be this.

Figure 3.7a shows the simulated coupling efficiency when tuning the position of the extra lens and the distance between the lenses in the collimator. The beam path is schematically depicted in figure 3.7b, and a simulation for its beam size evolution before optimization is illustrated in figure 3.7c. The simulation suggests that the closest the extra lens is to the waveguide, the better the coupling. Experimentally there is a limit to how close this extra lens can be set, and that is to just before the dichroic, as putting it afterwards would create unwanted absorption for the signal at 930 nm. As there is 15 mm from the dichroic to the waveguide, the extra lens should optimally be placed at a distance of 1.1 m after the pump. This would result in a beam width development as shown in figure 3.7d. The shape of the waveguide mode is illustrated in figure 3.7e, which has to match the beamfront of the

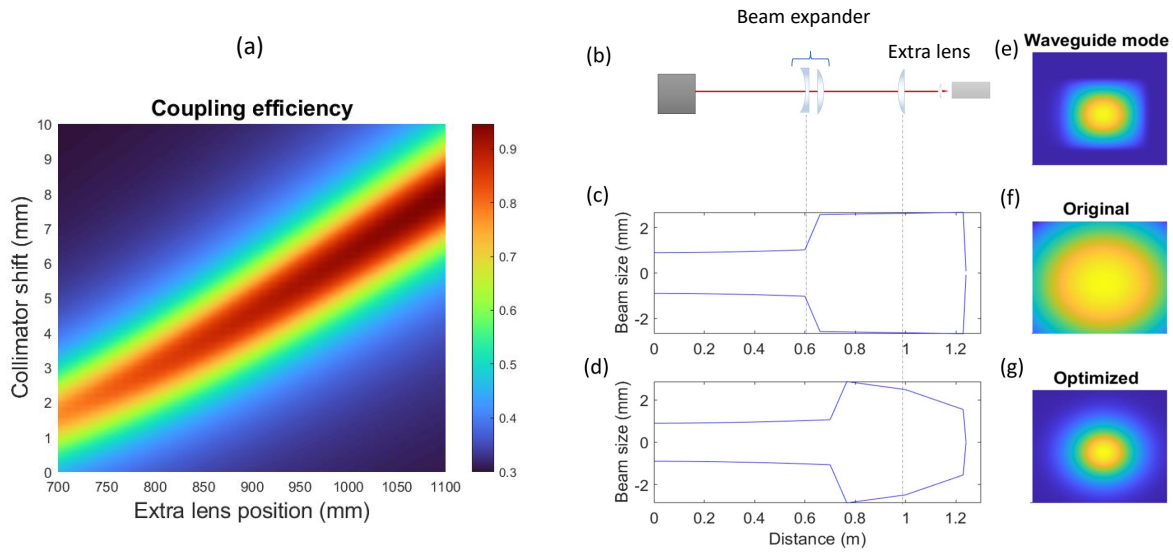


Figure 3.7: (a) Simulated coupling efficiency with respect to the extra lens position and the shift in the distance of the collimator lenses. (b) Lenses in the pump path. (c,d) Beam width propagation without and with optimization respectively. (e) Simulated mode for the pump field inside the waveguide. (f,g) Simulated field for the beam right before the waveguide in both the original and optimized configuration

incoming beam, illustrated in figure 3.7f for the original case and in 3.7g for the optimized setup.

According to this same simulation, further optimization of the pump coupling can be achieved by switching the position of the beam expander (BE) with the position of the waveplates, such that the BE is closer to the waveguides.

Experimentally the pump coupling cannot be measured directly, as the aspherical lenses have some significant losses at the pump wavelength and unfortunately I did not think of characterizing them before installing them into the setup. I took a measurement with a spherical lens of similar width and made of the same material and found the transmission of the pump to be of around 70 %. The loss can also be estimated from the lens to lens transmission coefficient, which is the power after the collection aspherical lens divided by the power measured before the signal aspherical lens. Table 4.1 summarizes the experimental results for the transmission coefficients compared to the results from the simulation. The experimental uncertainties in the table come from measuring the transmission many times during

Optimization step	Coupling in simulation	Measured transmission
Original setup	$29.5 \pm 0.2\%$	$15 \pm 3 \%$
Collimator distance optimizing	$83 \pm 2\%$	$38 \pm 2 \%$
New lens before dichroic	$93 \pm 3\%$	$44 \pm 2 \%$
Switch BE position	$95 \pm 2\%$	$44 \pm 2 \%$

Table 1: Pump coupling optimization summary. The measured transmission is the ratio between the power after the output aspherical lens with the power before the input aspherical lens.

the course of the experiment, giving an estimate of what range of values the transmission is usually between. From the table it can be seen that switching the BE position has no measurable influence on the coupling of the pump, even though it should be an advantage according to the simulation. I decided to leave the setup with the switched BE position as it might still be better, just not measurable

due to the large uncertainties.

### Collection path

The last step after converting is to collect the 1550 nm light into a fiber. For this it is necessary to separate the 1550 nm light from the pump and any eventual residual 930 nm light. There are many ways to separate light into its frequency components, it can be done by a prism, a grating or a specially designed dichroic mirror. Prisms can be made with minimal losses, but they have a small spread. Gratings would have higher losses due to higher order modes, but a very wide spread. Dichroic mirrors are usually the preferred choice, as they are good at filtering the unwanted light but also have a very good transmission for the desired wavelength, but they are very expensive. In this setup a prism is used, and its advantages and disadvantages are further discussed in chapter 6. Apart from a

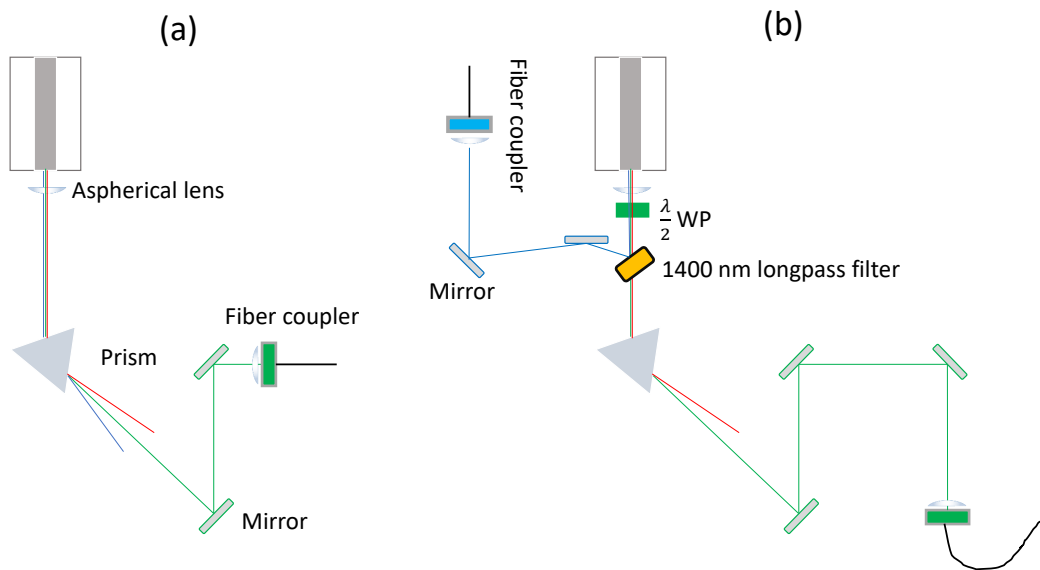


Figure 3.8: (a) Original design for the collection. (b) Modified design for the collection.

prism, 2 mirrors are necessary to collect the light, such that it can be coupled into a fiber. 1550 nm dielectric mirrors are used, which have a high reflectance in the region 1300 - 1700 nm, but are very lossy outside this region. These function as additional filtering mechanisms. The resulting design can be seen in figure 3.8a. Through the course of my thesis I have added many elements to the collection to improve the end to end efficiency and the purity of the collected light, resulting in the path seen in figure 3.8b. The reasons for these modifications will be discussed in chapter 5 and chapter 6. The overall setup, made of putting together all the parts introduced in this section, is shown in figure 3.9.

### 3.4 Summary

A simple illustration of the main idea of the setup can be seen in figure 3.1. Through this chapter the function and operating parameters of the different components have been described together with some of their limitations. The coupling of the pump into the waveguides was optimized through simulations and the results of this optimization can be seen in table 4.1. The final version of the setup can be seen in figure 3.9, and the details about the PPLN waveguides are specified in figure 3.4.

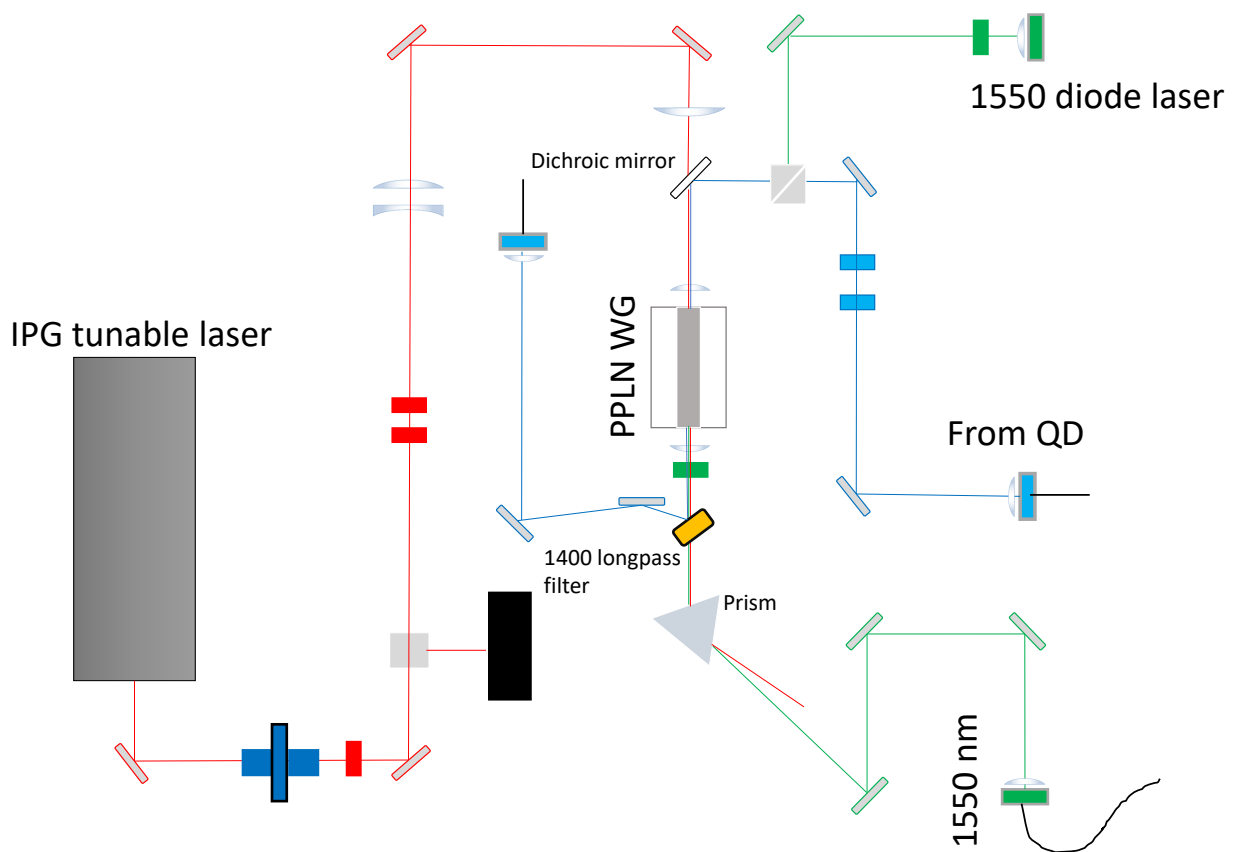


Figure 3.9: Full optimized setup without the optical elements required for alignment. The 1550 diode laser is only used for SFG, and the beam splitter that couples it to the setup is taken down when doing DFG

## 4 Conversion range and spectrum

Chronologically, the experimental part of the project started by installing optics and aligning all of the lasers' free-space optical paths into the waveguides. Then, frequency conversion was introduced, beginning with sum frequency generation (SFG), then difference frequency generation (DFG) and at last single photon DFG, optimizing the setup more and more everytime. This chapter describes the first frequency conversion experiments in this project, which were with SFG, and were useful for gaining knowledge about the phase-matching conditions and characterizing the setup.

### 4.1 Sum frequency generation

To produce SFG, a 1550 nm diode laser is coupled into the PPLN waveguides together with a strong pump laser at around 2300 nm. For further details on the lasers and the coupling see chapter 3. Even though it was not strictly necessary, SFG was an important tool for achieving DFG. This is because it is easier to achieve, making it a valuable proof of concept before moving to the slightly more complicated process of DFG. This section describes how SFG was achieved and how it helped exploring the range of frequencies that can be converted by the waveguides, as well as the tolerable bandwidth of the input light for frequency conversion.

#### Achieving SFG

There are two reasons why SFG is easier to achieve than DFG. The first reason is that the camera that was available could not detect anything above 1300 nm, but was very sensitive for frequencies around 930 nm. This meant that if there was just the slightest amount of SFG at 930 nm, it would be detected by the camera. The second reason is that the output wavelength is far from the telecom and pump wavelengths, so with a photodetector in the range 400-1100 nm, the power of the pump and the residual 1550 nm light are not detectable, and there will only be a signal if there is SFG. Detecting the light with a photodetector is also essential for alignment optimization.

To achieve SFG, it is necessary that both the 1550 nm diode laser and the pump are coupled into the same waveguide. In my guide on how to couple the pump into the waveguide (appendix A), I suggest using SFG as a mean to couple the pump into the waveguide. This was though not possible before achieving SFG for the first time, as the phase-matched wavelength and its required temperature were not known. The pump had therefore to be coupled solely by using the visible light laser and the thermal detector cards. After coupling the pump, the camera was installed and focused on the desired waveguide. This was possible by using a light diode that illuminates the waveguides, giving a view as the one illustrated in the upper picture of figure 4.1a, and then focusing the camera on the square, which is the waveguide. Once both lasers were simultaneously coupled into the waveguide, and the camera was focused to the right position, the stepper motor position, which is the mechanical device that determines the wavelength of the pump, was scanned. The output was monitored with the camera, which was dark if there was no SFG. A dot appeared on the camera for a given wavelength, similar to the one in the lower picture of figure 4.1b, but much dimmer. The stepper motor was then set to the position that made the dot brightest. The camera was then replaced with a photodetector and the alignment was then configured with the mirrors and waveplates such that the measured power on the photodetector was optimized.

Apart from a proof-of-concept, another reason for doing SFG is that the phase-matching conditions are assumed to be the same for both SFG and DFG processes. Hence I could use SFG to characterize the phase-matching conditions of the waveguides and thus know the required pump wavelength and temperature for the phase-matching of the DFG. For this assumption to be valid, it was important to be sure that the converted light was in the fundamental mode, as higher order modes have different phase-matching conditions. A simple test was to see the SFG mode on the camera. The result can

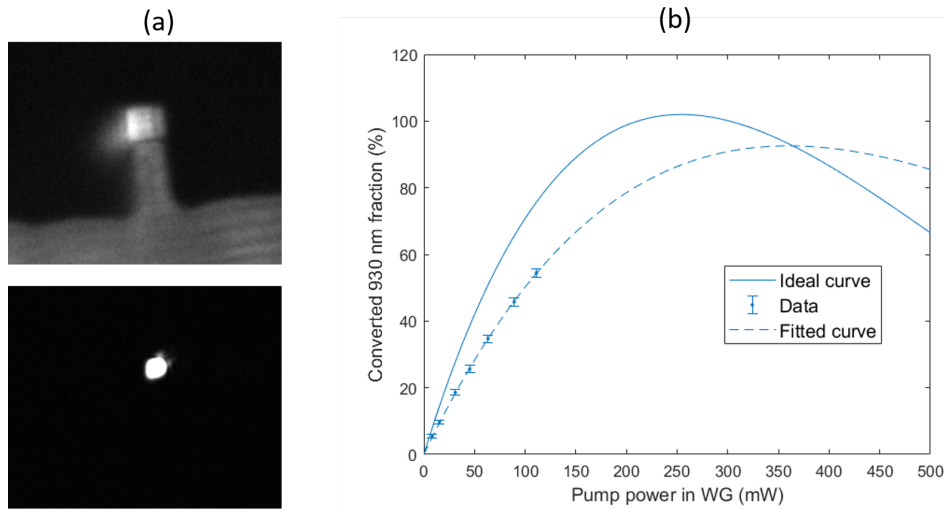


Figure 4.1: (a) Camera view of (above) waveguide illuminated by diode light, no lasers coupled, (below) sum frequency generated mode. The position of the camera is the same in both cases. (b) Measured converted SFG power as a function of the assumed power inside of the waveguides.  $P_2$  is the power of the 1550 nm light assumed to be coupled into the waveguide.

be seen in the lower picture of figure 4.1b, which looks very single-moded. There is some light on the lower left corner which does not look as a part of a fundamental gaussian mode, but that comes from imperfections of the camera, as the same distortion is similarly present in the upper figure.

As a second test for single-moded conversion and to check if the lasers were coupled correctly, the converted light for different pump powers was measured. The results should follow the theoretical curve described by equation 2.21, which has been proven experimentally by previous work on SFG [21]. The result of this experiment can be seen in figure 4.1b. Due to technical problems with the pump laser at the time at which the experiment was done, the pump could only achieve about 30% of its expected output power, impeding a high maximal conversion efficiency. A fit was done to have an estimation of how the data-points would look if higher pump powers were achieved, this can be seen as the dashed line in the figure. There are two differences between the fitted curve and the ideal curve. The first is that the ideal curve reaches its peak at lower pump power. The reason for this will be discussed in section 4.2. The second is that the maximal value for the fitted curve is 90% of that from the ideal curve. There are two physical reasons for this. The first one is that there might bad coupling of the 1550 nm laser into the waveguides, and the second one is that the aspherical lenses have higher losses at NIR than at telecom wavelengths, which will be explored in the next chapter. In any case, 90% projected conversion efficiency of the 1550 nm light together with the fundamental looking mode in the camera picture gave strong evidence for the fact that it was indeed the fundamental mode that was being converted.

The result of the characterization of the waveguides is summarized in the following table:

WG number	Poling period ( $\mu\text{m}$ )	T ( $^{\circ}\text{C}$ )	$\lambda_{\text{pump}}$ (nm)	$\lambda_{\text{out}}$ (nm)	Bandwidth (nm)
1	24.5	43.3	2153.7	901.32	Not measured
2	24.5	43.6	2148.0	900.32	Not measured
3	24.8	43.6	2196.2	908.68	0.26
4	24.8	43.6	2190.5	907.71	0.29
5	25.1	43.6	2241.2	916.29	0.33
6	25.1	43.6	2236.4	915.49	0.34
7	25.4	44.2	2289.4	924.25	0.34
8	25.4	43.9	2282.9	923.18	0.34
9	25.7	43.9	2340.0	932.38	0.32
10	25.7	43.9	2333.9	931.42	Not measured
11	26.0	43.9	2396.7	941.27	0.34
12	26.0	43.9	2387.3	939.81	0.34
Uncertainty	Unknown	0.1	0.5	0.05	0.03

where  $\lambda_{\text{pump}}$  is the wavelength of the pump that gave the maximal conversion efficiency at the given temperature and  $\lambda_{\text{out}}$  is the calculated output wavelength using energy conservation and assuming that the diode laser has  $1550 \pm 0.2\text{nm}$ . The bandwidth is given for the 930 nm range, and details about how it was measured are given in the next section.

### Conversion range and bandwidth

According to the simulation in section 2.2, for a fixed temperature, the converted light should have a similar spectral shape to a sinc function if the wavelength of the 930 nm light is scanned. The full width half maximum can then be obtained by simply scanning the wavelength of the pump, and calculating the output wavelength by using energy conservation. Doing such an experiment for WG 9 gives the spectrum of figure 4.2a. The bandwidth of this waveguide is measured by reading the full width half maximum of this spectrum, which is  $0.32 \pm 0.03$  nm. The curve looks like an asymmetric sinc function and the reason for this asymmetry is explored in the next section. The converted power in the Y axis is in arbitrary units and the reason is that the experiment was done at a very low pump power, so giving the converted fraction would be misleading. This applies for the rest of this thesis in any plot where the converted power is given in A.U..

The conversion range for each waveguide is not limited to the conversion bandwidth, as the phase-matching wavelength can be tuned by changing the temperature. This was observed experimentally, and the resulting conversion range for one in each waveguide pair in the chip is illustrated in figure 4.2b. This experiment was done by finding the optimal wavelength for the given waveguide at  $15^{\circ}\text{C}$  and then at  $65^{\circ}\text{C}$ , which are the two temperature extremes that the thermistor can provide. It can be seen that any wavelength in the range from 900 to 950 nm can be phase-matched using one of the waveguides. For some wavelengths, there are even two possible waveguides for phase-matching. But in practice, as will be showed soon, the conversion efficiency drops for very high temperatures ( $T > 50^{\circ}\text{C}$ ), so this "double phase-matching" is not useful if the goal is to have efficient frequency conversion, and if in doubt one should always choose the waveguide effective at the lower temperature.

A specific example of the conversion range for one of the waveguides is illustrated in figure 4.3a, where the measured temperature dependence of the optimal wavelength for waveguide 10 is shown. Between 20 and  $50^{\circ}\text{C}$ , the experimental values are seen to be close to the simulated values, but they differ significantly outside this range. The conversion range according to the simulation should be 8 nm, while the measurement says 13 nm, which is a difference of about 40%. The simulated curve seems to have a different shape than the pattern formed by the experimental measurements.

The conversion efficiency was observed to depend on the temperature, and is illustrated in figure 4.3b. Theoretically, if the light is phase-matched and optimized, there should be no difference in the

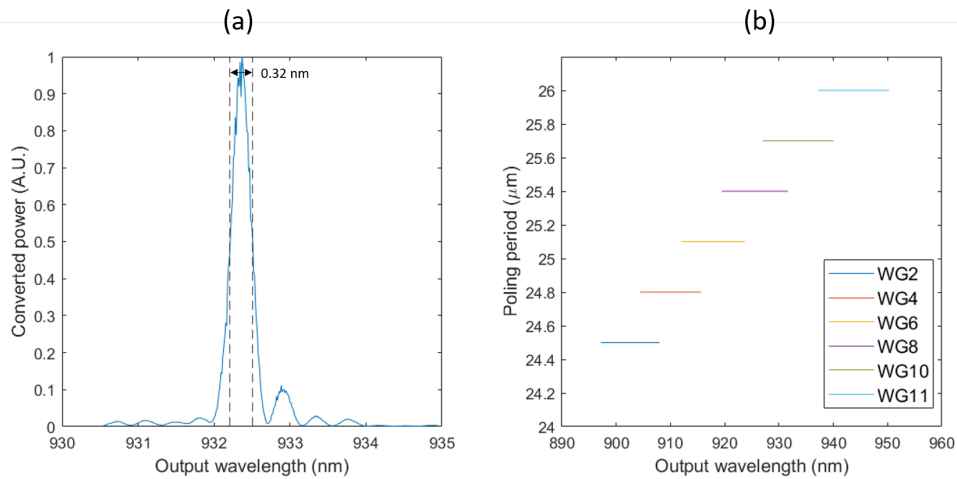


Figure 4.2: (a) Spectrum during wavelength scan of the pump for SFG in WG 9. The temperature and the wavelength of the 1550 nm laser are kept constant. (b) Possible phasematch range by temperature tuning for each of the poling periods in the experiment.

conversion efficiency for different temperatures. The efficiency seems to be stable for temperatures between 25 to 45 °C and decreases a little bit at 15 °C, and dramatically at 65 °C. This coincides with the discrepancies in figure 4.3a, where the data and the simulations differ for the same temperatures. The reason for the anomalies in both figures might be due to a physical mechanism not included in the simulation. For example if the temperature distribution is not uniform, the phase-matching condition would be a function of the distance of propagation, instead of being constant as assumed in the simulation. This could happen if the heat provided by the thermistors was concentrated around their positions, creating a temperature gradient pointing away from the thermistors. This is beyond the scope of this thesis and should be investigated further.

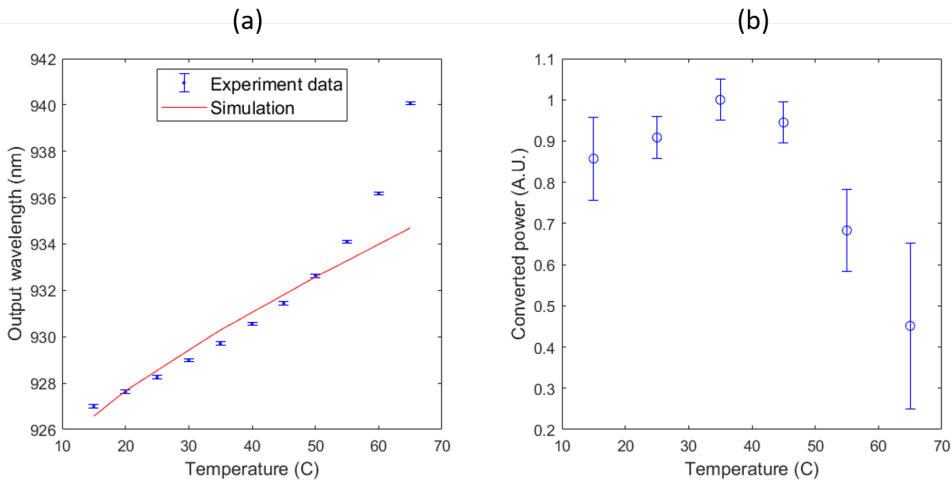


Figure 4.3: (a) Optimal SFG output wavelength as a function of temperature in waveguide 10. The simulation was done similarly to the one in figure 2.4c. (b) Conversion efficiency dependence on temperature for waveguide 6. The input power is the same, but the converted power changes depending on the temperature. The conversion was optimized in both alignment and phase-matching for every measurement.

The simulated curve in figure 4.3a is for a poling period of 25.9  $\mu\text{m}$ , instead of 25.7  $\mu\text{m}$ , where

the second is the poling period of waveguide 10 specified by the manufacturer. This is because I have found that for the simulated conversion range to be within the experimental range, the poling period used in the simulation has to be  $0.2 \mu\text{m}$  larger than the specified poling period, and this difference is the same for all the waveguides. An explanation could be that there is some physical mechanism that has not been taken into account in the simulation, which greatly shifts the position of the phase-matched wavelength. An example here could be that the poling was not instantaneous but had a finite displacement required for it to happen. This would effectively manifest as a constant shift in the phase-matched wavelength.

## 4.2 Spectral asymmetry mystery

The goal of this section is to find an explanation for the pattern observed in figure 4.4, which can be put into words in the following way: scanning the pump wavelength when doing SFG, the conversion spectrum for all of the waveguides is asymmetric. This asymmetry is anti-correlated for two waveguides with the same poling period. Moreover the phase-matched wavelength differs by about  $1 \text{ nm}$  for two waveguides that have exactly the same poling period, which in theory should have very similar phase-matching conditions (except for the difference in the average width, which according to my simulations should maximally change the phase-matched wavelength by  $0.4 \text{ nm}$ ). To find an explanation, I have studied the influence that different imperfections in the frequency conversion process will have on the converted spectrum, by including them in the simulation.

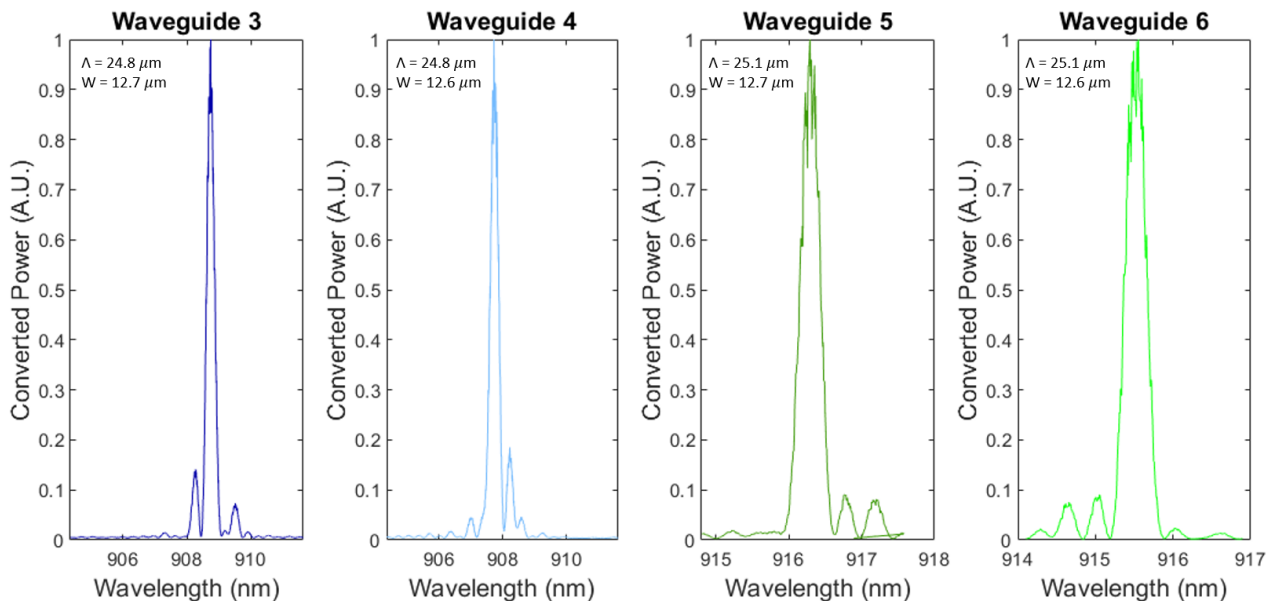


Figure 4.4: SFG pump scan for different waveguides.  $\Lambda$ : poling period,  $W$ : waveguide average width.

When talking about imperfections, there are four candidates: random temperature fluctuations, pump spectrum imperfections, alignment imperfections and fabrication imperfections. The first one, random temperature fluctuations, is an error that is always present to a certain degree. Temperature fluctuations would alter the phase matching condition and thus the conversion efficiency, which should influence the spectrum. Apart from random, there could also be systematic fluctuations due to the position of the thermistors, as discussed in the previous section. In any case, even though they may be present, they cannot explain why the patterns of a poling period pair are anti-correlated, since both waveguides should have the same temperature fluctuations, and thus be affected equally. The setup alignment or the spectrum of the pump laser can neither explain the pattern, for exactly the same

reason. The only candidate left are fabrication imperfections. I have therefore focused my simulations to fabrication imperfections in the waveguides and their effect on the conversion spectrum.

The patterns in a poling period pair are anticorrelated, but there is no correlation between the patterns of different pairs. It is therefore reasonable to assume that each pair, along with its imperfections, was fabricated individually. The first error that I studied were imperfections in the poling period, i.e. if the distances between the sign flips of  $X^{(2)}$  are not completely uniform. I introduced these imperfections in the simulation by changing the position of the sign flip within a poling cycle, which in the perfect case would be after  $0.5\Lambda$  or 50% of the length of the poling period. The result is seen in figure 4.5a, where it may be concluded that imperfections in the poling period only affect the overall conversion efficiency, but create no asymmetry in the spectrum. This can be also explained by the argument that imperfections in the poling period do not introduce any spectrally dependent change to the phase-matching condition, and can therefore not create any spectral pattern. To ex-

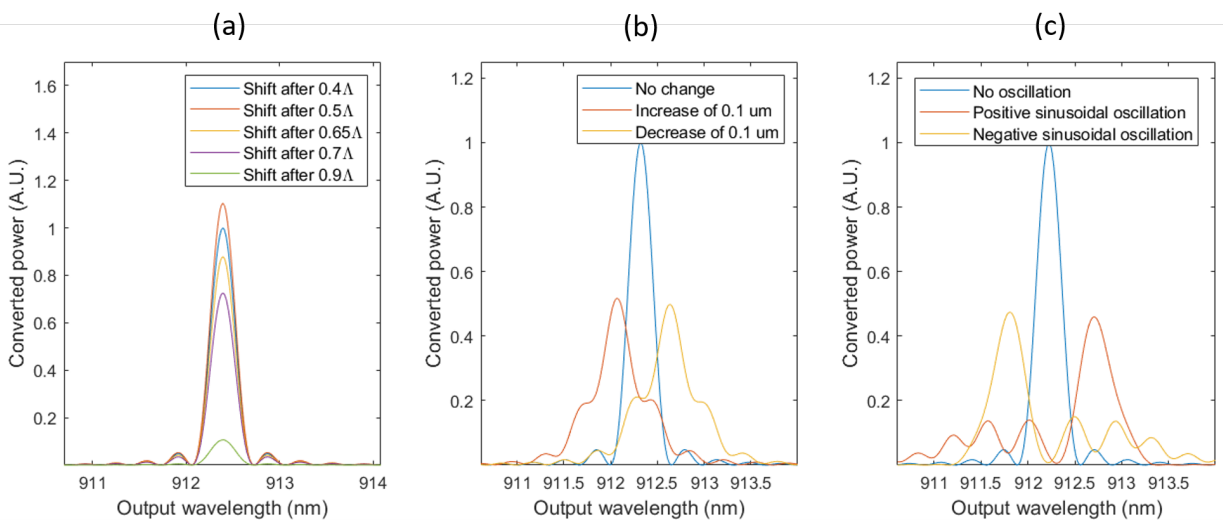


Figure 4.5: (a) Converted spectrum simulation of imperfections in the poling period. Each poling cycle has the same length, but the position of the sign shift in the middle of the cycle is varied. (b) Spectrum simulation in the case of a linear increase or decrease in the waveguide width. (c) Spectrum simulation in the case of sinusoidal oscillations of the waveguide width. The oscillation period is  $\lambda = 2L$  where  $L = 48$  m and it has an amplitude of  $A = 0.2\mu\text{m}$ .

plain this pattern it is therefore necessary to find an error that is both related to the fabrication of the waveguides and also adds a spectral dependence to the phase-matching condition. I found that the only reasonable candidate to explain this problem would be imperfections in the width of the waveguides. These imperfections would have a spectral dependence as they would change the effective mode index differently depending on the wavelength. From a fabrication perspective, if the lithium niobate is firstly poled and then cut into pairs of waveguides, the width of the two waveguides will be anticorrelated due to imperfections in the cutting process. If the imperfection results in a linear increase or decrease of the waveguide width as a function of distance, the effect on the frequency conversion spectrum according to my simulation can be seen in figure 4.5b. From the figure it may be concluded that such imperfections will decrease the conversion efficiency, change the shape of the spectrum, and shift the phase-matched wavelength by about 0.5 nm. This comes very close to explaining the pattern in figure 4.4, but the asymmetry is still missing. By considering that the width imperfections are not linear but sinusoidal instead, the pattern of figure 4.5c is obtained. This one is similar to the linear case, but now the curves are also asymmetrical and anticorrelated. By deduction, and by the lack of other candidates, it may therefore be concluded that the spectral asymmetry is caused by sinusoidal width oscillations in the waveguides.

Sinusoidal oscillations have 3 parameters: period, amplitude and phase. I have done my simulation for different values of these 3 parameters to have an idea of the range they may reasonably take for the waveguides of this experiment. For example to estimate the period of the oscillations I have looked at the spectrum for different oscillation periods as shown in figure 4.6. The experimental spectrum patterns are definitely not as irregular as the one shown in figure a, neither as the one in b, but they are also not as regular as the one shown in figure c. It can therefore be estimated that their oscillation period is between  $2L$  and  $3L$ , where  $L$  is the length of the waveguides. By analogous simulations I have estimated that the oscillation amplitude must be between 1 and 2  $\mu\text{m}$ , and the phase must be very close to zero.

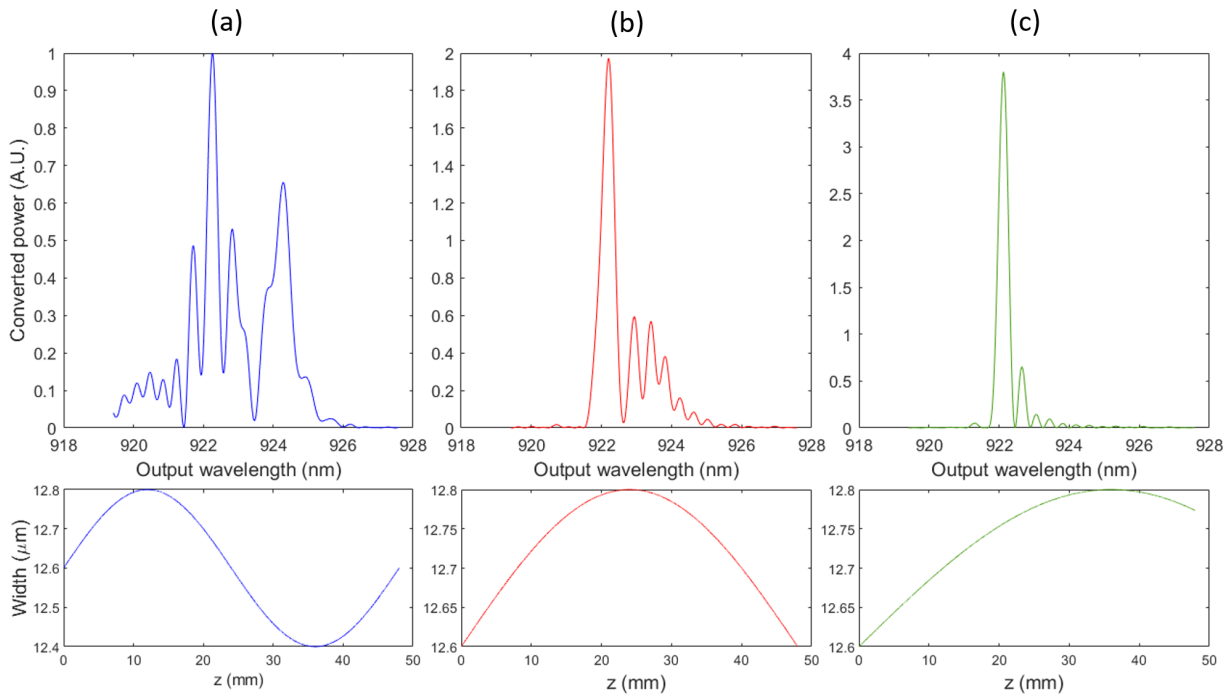


Figure 4.6: (a) Simulated conversion spectrum for width sinusoidal oscillation with period of  $L$  (length of the waveguides). (b) Simulated conversion spectrum for width sinusoidal oscillation with period of  $2L$ . (c) Simulated conversion spectrum for width sinusoidal oscillation with period of  $3L$ . In all three cases the oscillation amplitude is  $0.2 \mu\text{m}$

Given that these width oscillations are present, it is important to estimate their influence on the conversion efficiency. A simulation of the expected conversion efficiency as a function of the pump power taking the width oscillations into account can be seen in figure 4.7. The simulation shows that these imperfections do not result in a significant change to the maximal conversion efficiency, but result in a higher pump power requirement to achieve full conversion. For the width oscillations in figure 4.6c, there is only slightly more power required than in the perfect case, reaching its maximum at around 300 mW. But for the case of figure 4.6b, a pump power of 600 mW is required to achieve full conversion. In practice, the required pump power is somewhere in between these two numbers, but it is hard to estimate the precise value due to the complexity of the simulations.

### 4.3 Summary

The characterization of the waveguides through sum frequency generation is mainly summarized by figure 4.2. The bandwidth for all the waveguides is on average  $0.322 \pm 0.01 \text{ nm}$ , and by temperature

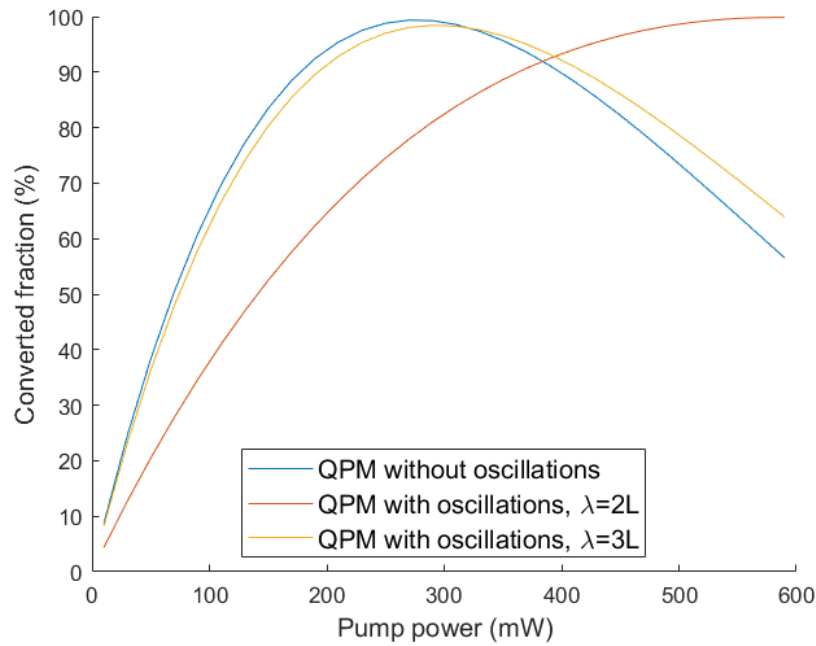


Figure 4.7: Expected conversion efficiency as a function of pump power. The blue curve is the same as the red curve from figure 2.3b. The red and yellow curves are including the width imperfections depicted in figure 4.6b and c.

tuning, any wavelength from 900 to 950 nm can be phase-matched for frequency conversion. The conversion bandwidth for a fixed temperature was found to be the same as what was expected from the simulations, but the conversion range on the other hand was found to be about 40% smaller, suggesting that there was some physical mechanism that was not taken into account by the simulations. The converted spectrum for all of the waveguides, which should look like a symmetric sinc curve around the optimal phase-matching wavelength, is instead an asymmetric looking sinc curve. This is explained by sinusoidally oscillating width imperfections in the waveguides, which were produced during the fabrication process. These imperfections have the effect that more pump power is required to achieve full conversion than what was predicted in the original model.

## 5 Conversion efficiency

The main non-linear process for the purpose of this experiment is difference frequency generation (DFG). Unlike with sum frequency generation (SFG), which was only used as a proof of concept, the end to end efficiency is important for DFG, as it directly affects the count rate of 1550 nm single photons that can be produced. This chapter describes how DFG was achieved and the many optimization steps that were implemented to achieve a high end to end efficiency. Section 5.3 describes the end to end efficiency results of DFG for different light sources, including the quantum dots.

### 5.1 Difference frequency generation

Achieving DFG is slightly more challenging than achieving SFG for 2 reasons. Firstly because achieving single moded light inside the waveguides is harder for 930 nm light than for 1550 nm light, as the higher order modes for 930 nm light are easily excited. Secondly, the output of DFG has a wavelength of 1550 nm, which is closer to the wavelength of the pump around 2300 nm. This means practically that all of the available photodetectors that could detect light at 1550 nm could also do so at 2300 nm, making it impossible to differentiate the converted signal from the pump transmitted light using photodetectors. For these reasons SFG was done to characterize the waveguides, such that the phasematching wavelengths and temperatures of each waveguide were known, which would facilitate achieving DFG. To achieve DFG it is therefore advised to use the given parameters in the table of section 4.1 for the selected waveguide.

Before trying DFG, the two problems just described had to be solved. The first problem was tackled by using a continuously tunable laser (CTL) with a high output power capability as the 930 nm signal source. This laser was visible in the IR camera, allowing the alignment to be optimized such that the image seen in the camera would be of single moded light. The second problem required the use of the prism and the fiber coupling, such that the prism would separate the different frequency components and only the 1550 nm light would be coupled into the fiber. To make sure of this, the light of the 1550 nm diode laser was used as a guide, sending it through the waveguides, prism and coupling it to the fiber.

With these considerations, DFG was easily obtained for a high input power from the CTL, as enough light was converted to be detected with a photodetector placed at the end of the output fiber. The signal was detected and then optimized by beam walking the signal path, the pump path and the collection path, as well as moving the position of the aspherical lenses that couple in and out of the waveguides. After optimizing, the end to end efficiency of the whole setup was estimated. Since the goal of the setup is to do single photon conversion, the end to end efficiency can be defined as the ratio of the output photon number with the input photon number. When converting high power laser light, where the output is measured by a powermeter, this ratio can be calculated by using the following equation:

$$\eta = \frac{P_{out} \lambda_{out}}{P_{in} \lambda_{in}}, \quad (5.1)$$

where  $P_{out}$  is the power measured after the output fiber,  $P_{in}$  is the power measured the input fiber,  $\lambda_{out}$  is 1550 nm and  $\lambda_{in}$  is the wavelength of the CTL.

In the early stages of the experiment, before different optimization ideas were implemented, a  $22 \pm 1\%$  end to end efficiency was achieved. This was when using the collection path of figure 3.8a. In the next section the optimization steps that allowed to almost double this efficiency will be described, but before that, there is a question that arised when DFG was achieved, and should be discussed first.

### Scan width differences

A common measurement to do during optimization with laser light is a spectrum measurement or wavelength scan, to find the optimal wavelength for the conversion process. When doing SFG there was only the wavelength of the pump laser that could be scanned, as the diode laser had a fixed wavelength at 1550 nm. For DFG on the other hand, both the pump laser and the CTL wavelength were possible to scan. Naively it was expected that they would both result in a similar FWHM to the one in figure 4.2a, where a pump wavelength scan was done for SFG, giving a FWHM of  $0.33 \pm 0.03$  nm at the 930 nm range or  $1.9 \pm 0.2$  nm at the pump wavelength range. For DFG the measurements resulted in a FWHM of indeed 0.33 nm for the CTL (930 nm range) wavelength scan, but a FWHM of  $28 \pm 1$  nm for the pump scan. In other words, the pump scan for DFG gave a peak that was 15 times broader than what was naively expected from SFG, even though the CTL scan for DFG gave exactly the same width as what was expected from SFG. This subsection analyzes how and why this discrepancy arises. The measurements for the 930 nm range scans for both SFG and DFG are

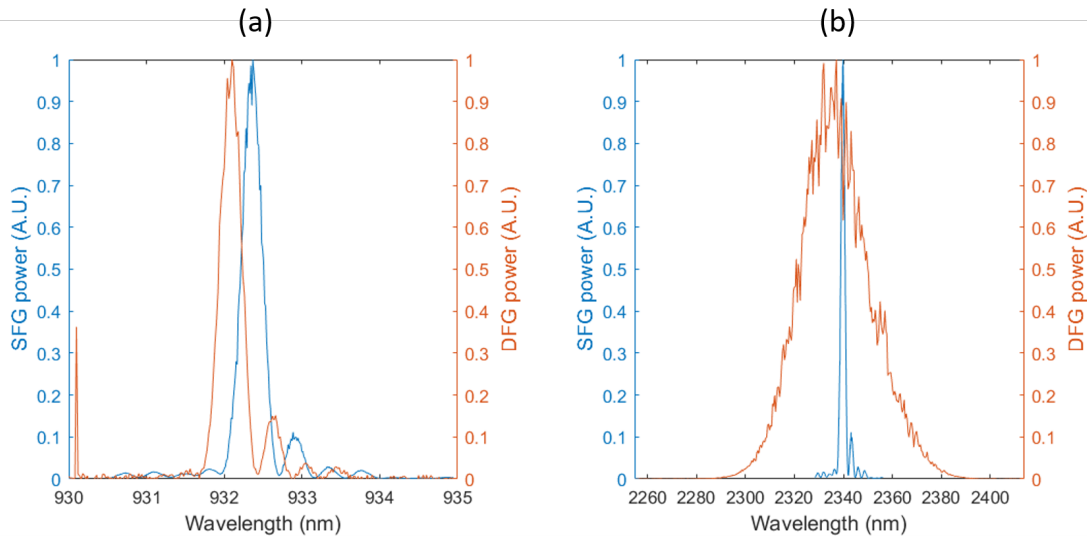


Figure 5.1: (a) DFG in WG9 where the pump wavelength is kept constant and the CTL wavelength is scanned compare to SFG where the pump wavelength is scanned. The output wavelength for SFG is calculated by energy conservation. The peak at 930 nm for the red line is due to an instrument error from the powermeter. (b) DFG in WG9 where the pump wavelength is scanned and the CTL wavelength is kept constant compared to the same SFG pump scan as in (a) but with the pump wavelength plotted.

illustrated in figure 5.1a, which were done on waveguide 9. They have the same width but a slightly different peak position. This position difference will be explained later when talking about efficiency optimization. The pump scans are illustrated in figure 5.1b where the DFG case is much broader than the SFG case. Just as with the spectral asymmetry mystery in section 4.2, this mystery was also solved by doing a simulation, but this one in contrast proved to be much more simple.

Figure 5.2a shows the simulation of a DFG signal scan (comparable to an experiment where the CTL is scanned). The simulation has the same width as the experiment. Similarly figure 5.2b shows the simulation of a pump scan, which as in the experiment is much broader than the signal scan. The reason for the difference in their width can now be analyzed, and the easiest way is by looking at the orange curves of both figures, which is a plot of the calculated phase mismatch  $\Delta k$  as a function of the wavelength. It can be seen that the slope of  $\Delta k$  is much steeper for the signal scan than for the pump scan, making it deviate away from 0 much faster for the signal scan. This can be explained by looking

at figure 2.4b, where the effective mode index in the 930 nm region is steeper than in the rest of the simulated regions. When doing SFG and scanning the pump, the 930 nm output wavelength was also scanned, making this steep slope relevant, but when scanning the pump for DFG, what changed was the 1550 nm wavelength, while the 930 nm wavelength remained constant, such that the change in the effective mode index was slower. This answers the original question, at least qualitatively, but taking a closer look at the the solid blue curve in figure 5.2b, its FWHM can be determined to be  $68 \pm 2$  nm, which is more than the double of the measured value. The question of "why is the spectrum so broad?" turns into a question of "why is the spectrum so narrow?" when comparing the experiment with the simulation. Another question that arises is, why are there no side peaks for the orange curve in figure 5.1b? The rest of this subsection will be devoted to answering these two new questions. To

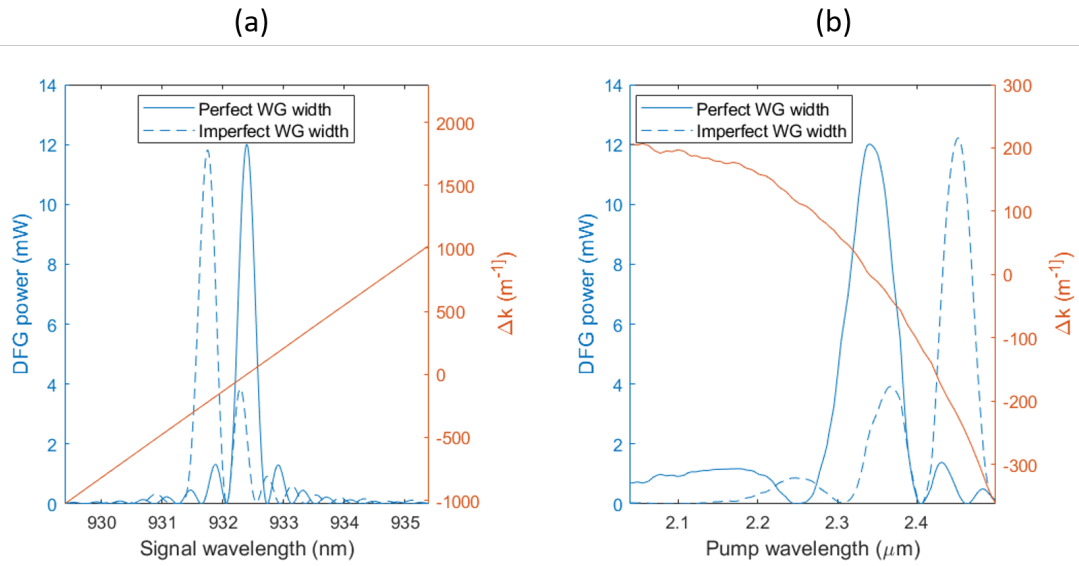


Figure 5.2: (a) Simulation of a signal scan for DFG where the Pump wavelength  $\lambda_1$  is kept constant and the signal wavelength  $\lambda_3$  is scanned. (b) Simulation of a pump scan for DFG where  $\lambda_1$  is scanned and  $\lambda_3$  is kept constant. In both cases the curve for the width oscillations corresponds to the oscillations described in figure 4.6c. Also in both cases the plotted  $\Delta k$  curve describes the phase mismatch calculated by eq 2.22 for the perfect width case. The input power is set to be 20 mW.

find an explanation, there are two physical mechanisms that have to be taken into account. First there is the fact that the waveguides probably have some width imperfections shaped as sinusoidal oscillations as discussed in section 4.2. Adding these imperfections into the simulation, the spectrum should become the one depicted by the dotted blue line of figure 5.2b, which is less broad and has a FWHM of  $43 \pm 1.5$  nm. This partly explains the narrowness of the experimental curve. The second reason is that the prism together with the fiber coupling in the collection path act as a bandpass filter with a limited bandwidth. Given that the wavelength of the 1550 nm light is also shifting during the pump scan, this filtering mechanism becomes relevant, and explains why the sidepeaks are not visible, and probably also why the experimental curve is narrower than the simulated curve.

The effect of the prism and fiber coupling combination was estimated by the following experiment: A pump scan was done and the converted output was monitored. Furthermore, the residual 930 nm light, which is the light coming out of the waveguide that failed to be converted, was also monitored. The easiest way to do this is to use the 1400 nm bandpass filter, which also functions as a dichroic mirror, reflecting the 930 nm light but transmitting the 1550 nm light. This allows to have a separate detector for each beam, and if the dichroic mirror is placed before the prism, the residual light will not be filtered by the same mechanism as the 1550 nm light, allowing to measure the full spectrum

indirectly. The result for this experiment can be seen in figure 5.3. It can be seen that the sidepeaks

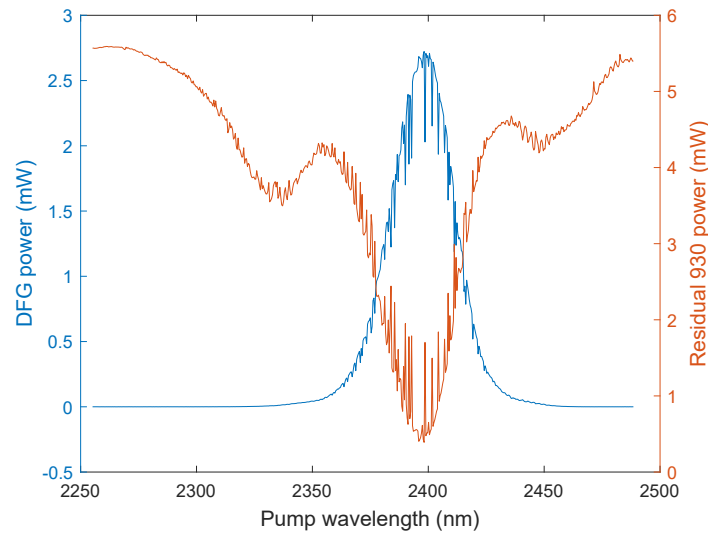


Figure 5.3: DFG pump scan with the CTL wavelength kept constant for WG11. The amount of residual 930 light, which is the amount of light at 942 nm that was not converted is also measured. This residual light suffered losses in the order of 40% due to the 1550 nm waveplate.

are present in the residual light spectrum, and that the main peak of the residual light is broader than the one for the 1550 nm signal. The FWHM of the residual light main peak can be determined to be  $47 \pm 3$  nm, which is close to the width of the simulation, in contrast to the FWHM of the 1550 nm light which is  $29 \pm 1$  nm. The question of why the pump scan simulation is broader than experimental scan measurement can therefore be answered by the fact that the prism and fiber coupling combination act as a filtering mechanism.

## 5.2 End to end efficiency optimization

One of the main goals of this project was to achieve a high count rate of single photons at 1550 nm. For this it is important to have a QD with a high count rate and also a good end to end efficiency of the frequency conversion setup. This section describes the optical elements and alignment techniques that helped double the conversion efficiency from what was achievable in the early phases of the experiment.

### Prism transmission

The prism has 2 important parameters that have to be taken into account when maximizing the transmission through it. The first, which was expected and taken into account from the beginning, is that the insertion angle of the 1550 nm light has to be equal to the angle of minimal deviation for the prism. This is essential for the prism to cause dispersion optimally, but it also maximizes the transmission through it. The angle is found experimentally by turning the prism on a rotation stage and looking at the transmission with a detector card. For most angles the spot will be at a specific point, but it will start moving in one direction when the angle is close to the minimal deviation angle and then move in the opposite direction once the angle has been passed. When the spot is at its extreme position, it will also be at the minimal deviation angle.

The second parameter is the polarization, which was not taken into account in the original setup design. The prism has a reflectance below 1% for P polarized light, but for S polarized light it is about

30%, according to the manufacturer. The converted light coming out of the waveguide is S polarized as this is the polarization of the non-linear susceptibility. To correct for this polarization preference mismatch, there were two possibilities. The first was to put a 1550 nm waveplate in front of the prism. This would introduce an extra loss to the setup, but it should be below 0.2% for most waveplates. The second was to turn around the prism, such that its dispersion would be in the vertical direction instead of horizontal. This would introduce an extra technical challenge when doing the fiber coupling as the light would have a steep vertical angle. For the setup the first option was chosen, as it was more simple and the extra losses introduced were negligible.

Installing the waveplate was the most important optimization step for the end to end efficiency. It allowed to couple 40% more of the converted light into the fiber, yielding an end to end efficiency of 37% very shortly after its installment. The reason why there was 40% reflection on the prism surface instead of 30% as was expected from the manufacturer specifications is unknown.

### Alignment optimization - camera aid

The high value of 37% end to end efficiency was achieved, but I was unable to reproduce for about 2 months afterwards. The end to end efficiency varied a lot from day to day, and would maximally be at around 32% most days. The reason is that doing optimal setup alignment is a complex task, and for it to be consistently well done, some extra tools and realizations would be necessary.

One of the main alignment challenges is to achieve single mode operation of the 930 nm light inside the waveguides. There are three parameters that determine this condition: the input aspherical lens position and the orientation of each of the two coupling mirrors. Single mode operation results in the highest frequency conversion output, so in principle, single mode operation could be achieved alone by optimizing the converted power. This is the usual method opted for quick optimization, but it has two limiting factors. First is that the converted power fluctuates due to changes in the power of the pump or the CTL as well as polarization fluctuations of the signal input. This makes it hard to achieve single mode operation by optimizing the output power alone. Second is that it also relies on the alignment of the pump laser, introducing more parameters into the optimization, like the distance of the beam expander lenses and the orientation of the pump coupling mirrors. Having this many parameters allow for many local maxima for the optimization, like for example choosing an aspherical lens position that maximizes the coupling of the pump power but not the singlemodedness of the 930 nm light.

A second method to confirm single mode operation is to look directly at the mode using the camera. This has unfortunately also 2 problems. First is that the setup introduces some distortions to the beam such that even if the light is completely singlemoded it might still look a bit distorted on the camera. Second is that if the light is very well coupled, the single mode will dominate the picture, making any eventual higher order modes invisible in comparison. A way to combine the best of both methods is to look at the camera picture while the frequency conversion is running. In an ideal case where the light is completely singlemoded and there is a sufficiently high pump power coupled into the waveguide, the mode in the camera should disappear when the pump is turned on, as the camera cannot detect 1550 nm light. But if the light is not singlemoded, only the fundamental mode will disappear, allowing to see the weaker higher order modes on the camera. Unfortunately the pump power was never enough to achieve full conversion, so eliminating the fundamental mode completely was not possible during the experiment, but the technique was still useful. Figure 5.4 illustrates this technique for two cases. In (a) the 930 nm light is not optimally coupled into the waveguide, so it is multimoded. Still, by looking at the picture on the left it is hard to say if the irregularity is due to distortion on the camera or to multimodedness of the light. After turning on the pump the fundamental mode is attenuated and the higher order modes become more apparent, as can be seen on the right picture. This will usually be the case when the alignment is at one of the local maxima of the parameters. The problem usually lies in the position of the input aspherical lens, and these results will usually mean that its



Figure 5.4: Camera mode of the 930 nm light with the pump on and off for (a) a situation with higher order modes present and (b) a situation without higher order modes present

position has to be optimized. For an optimized alignment the pictures look like in figure 5.4b, where the mode is very similar with and without the pump.

### Alignment optimization - longpass filter aid

For reasons that will be explained in chapter 6, a 1400 nm longpass filter was installed in the collection, as shown in figure 3.8b. Not only a filter, it also proved to be a perfect dichroic mirror, with over 99% reflectivity for light at 930 nm. It was therefore possible to collect the 930 nm light coming out of the waveguides and measure it independently from the 1550 nm light. By monitoring the residual light, the internal conversion efficiency can be estimated by blocking and unblocking the pump by using the following equation

$$\eta_{int} = 1 - \frac{P_{on}}{P_{off}}, \quad (5.2)$$

where  $P_{on}$  is the residual power measured with the pump on, and  $P_{off}$  is the residual power measured with the pump off or blocked. Having an estimate of the internal efficiency simultaneously with the external efficiency, allows for quick alignment error diagnosis. If the internal efficiency is high but the external is low, the problem lies in the collection path, in which case it will usually be the fiber coupling that should be optimized. If both efficiencies are low, the problem lies in the pump path alignment or the polarization of the input signal. In both cases it is assumed that the 930 nm light in the WG is confirmed to be singled moded as described in the previous subsection.

A second way that the longpass filter can help improve the end to end efficiency is by spectral centering of the collection fiber coupling. Figure 5.3 shows a DFG pump scan of an instance where the collection is aligned such that the peak of the fiber-coupled light is at the same wavelength of the minimum of the residual light. This is not necessarily always the case. If the collection is aligned such that its transmission curve would be centered at a different position, as is the case in figure 5.5, the conversion will not achieve its maximal efficiency, as the phasematching is not perfect at the center of the curve. To correct for this, the wavelength of the pump has to be set to the one that gives the minimum of the residual light, and then align the mirrors in the collection to optimize the power coupled into the fiber.

### Limiting factors and further optimization suggestions

Applying the mentioned alignment techniques, an end to end efficiency of  $41.7 \pm 0.3\%$  was achieved, with an internal conversion efficiency of  $95 \pm 1\%$ . The internal efficiency is limited by two factors. First is that the light could still be a little bit multimoded, and second that there was not enough pump power to achieve full conversion. These two factors will be discussed in the next section. The external efficiency has many more limiting factors, and they will be discussed in this subsection.

To investigate the limiting factors on the external efficiency, I characterized the losses of all of the components in the input and collection paths of the setup. Figure 5.6a contains an illustration of the path that the single photons will follow, with the losses in each component written besides

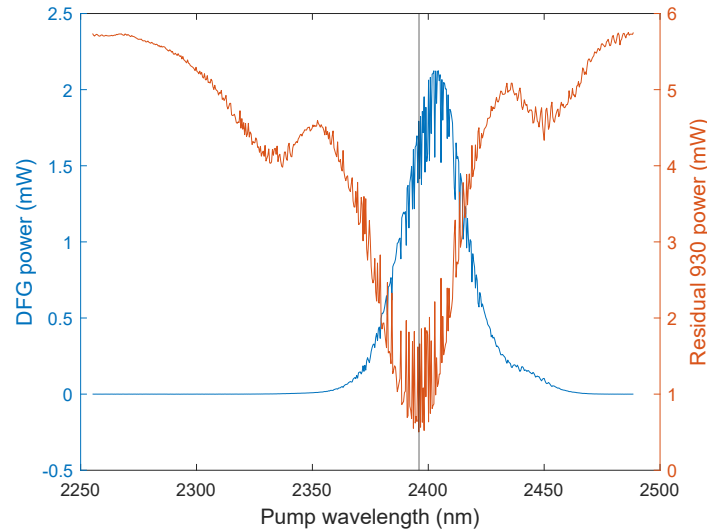


Figure 5.5: DFG pump scan with the CTL wavelength kept constant for WG11. The amount of residual 930 light, which is the amount of light at 930 nm that was not converted is also measured. The collection is not aligned in a way that both curves have extremes at the same wavelength.

them. The losses in the input path were measured using the CTL and placing a powermeter before and after each component. The uncertainty on these measurements is of about 5% of their value and is caused by power fluctuations of the CTL power and the photodetector measurement uncertainty. The 5% loss of the very first component are due to the use of a polarization maintaining (PM) fiber to couple into the setup. The single photons come from a single mode fiber, and coupling to a PM fiber always introduces losses. For the losses in the aspherical lenses and the coupling to the waveguide, no direct measurement of these was possible, as the distance between them was too short to put a powermeter in between. The values can be estimated from measuring the power before the input aspherical lens and after the collection aspherical lens. The total measured losses were of 25% for the CTL. Assuming a 95% waveguide coupling efficiency (simulation predicts  $96 \pm 1\%$ , if the alignment is completely perfect), the losses inside of the lenses were of 11% for each of them. If instead the losses are calculated from the refractive index, they should be of 8% for a 2mm thick lens of BK7 glass, in which case a waveguide coupling efficiency of 89% would account for the measured loss. In either case, the loss of one lens plus the waveguide coupling loss is about 17%. For the collection path, the losses were measured by coupling the 1550 nm diode laser through the waveguides and placing a powermeter before and after each component. Due to polarization oscillations and the aperture of the detector being very little, the uncertainty on the loss measurements were about 30%. Similarly to the 930 nm case, the aspherical lens loss could not be measured directly, but was estimated similarly, assuming no losses in the outcoupling. The mirrors in the collection path should have a reflectivity above 99.5%, but my measurements show that they scatter or absorb 1.5 to 3% of the incoming power. This is a sign that they may have some dust or scratches and should be checked.

Figure 5.6b shows the remaining photon fraction after a specified number of components, which is calculated by cumulatively multiplying the losses in figure 5.6a. Multiplying all of the losses together, and assuming  $95 \pm 1\%$  internal conversion efficiency, the end to end efficiency should be of  $42.0 \pm 0.5\%$ , which is in agreement with the measured efficiency of  $41.7 \pm 0.3\%$ . The two main limiting factors are the coupling efficiency to the collection fiber, and the reflection losses in the aspherical lenses. The fiber coupling efficiency might be improved by replacing its aspherical lens to one with a more suitable focal length or numerical aperture, as they may be limiting the coupling efficiency. The reflections

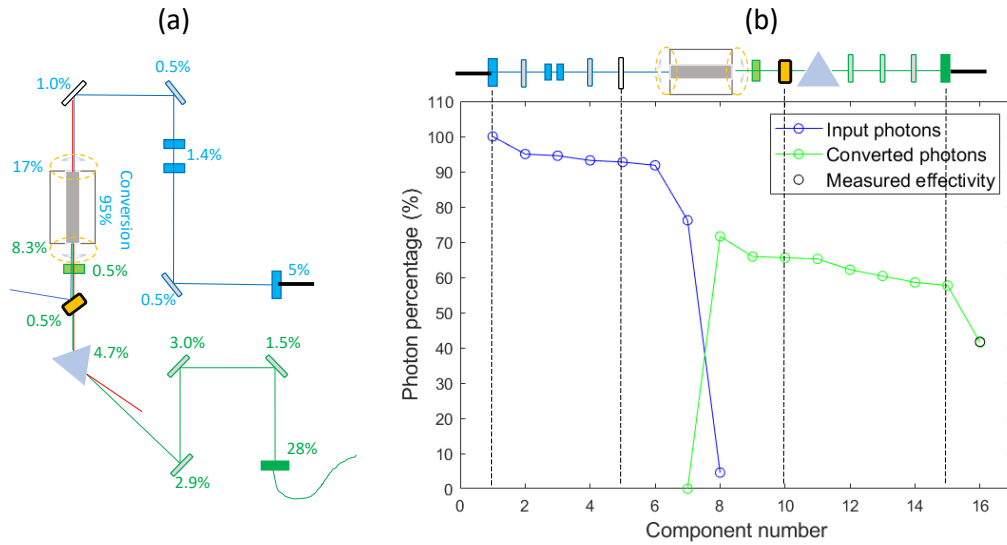


Figure 5.6: (a) Input and collection setup with the measured relative losses of each component specified. (b) Plot of the percentage of the photons expected to remain intact after a certain number of components. The component number comes from counting the number of components that the light goes through in figure (a).

in the aspherical lenses for the waveguide can be decreased by using standard anti-reflection coated lenses, which have very high transmission in their specified range of wavelengths. Such lenses were not applied to begin with because of the possibility that the high pump intensity may damage the coating. With the pump at its current maximum power, there will be maximally be 700 mW before the input aspherical lens, which corresponds to an intensity of  $1.8 \text{ W/cm}^2$ , and 500 mW before the collection aspherical lens, or an intensity of  $1.3 \text{ W/cm}^2$ . According to tests done by the manufacturer, anti-reflection coatings may suffer damage for intensities above  $2 \text{ W/cm}^2$ . If the lenses were to be replaced, it would probably only be safe to replace the collection lens, as the input lens may suffer damage. For the input lens, a custom coating would be necessary, which has high transmission both at the pump and the 930 nm regions. If the lenses were replaced by coated ones and the collection fiber coupling efficiency was improved to 80%, the end to end efficiency would increase to 55%.

### 5.3 Conversion of different sources

So far, all of the measurements presented have been using continuous wave (CW) lasers with bandwidths below 1 MHz. This section explores what happens when this and other kinds of light are used as the input, including single photons.

The case of CW light conversion is analyzed in figure 5.7a. The ideal curve is the theoretical curve in the case that there is 100% internal efficiency and no imperfections in the waveguides. The conversion efficiency should increase with the pump power, until it reaches saturation and begins to decrease, which can be seen in both the ideal and the fitted curve. In this experiment there was not enough pump power to achieve saturation, which is why the measured points do not reach the peak of the curve. The power inside the waveguide should have been of 397 mW to reach the top of the fitted function, but the maximal power achieved is of 326 mW. Efficiency-wise this is not a big problem, as the peak has 41.9% efficiency, while the maximal efficiency achieved experimentally had a value of  $41.7 \pm 0.3\%$ . As for the internal efficiency, the measured value is  $95 \pm 1\%$  experimentally with a maximum of 95.4% according to the fitted curve. This was measured by looking at an analogous plot for the residual NIR curve.

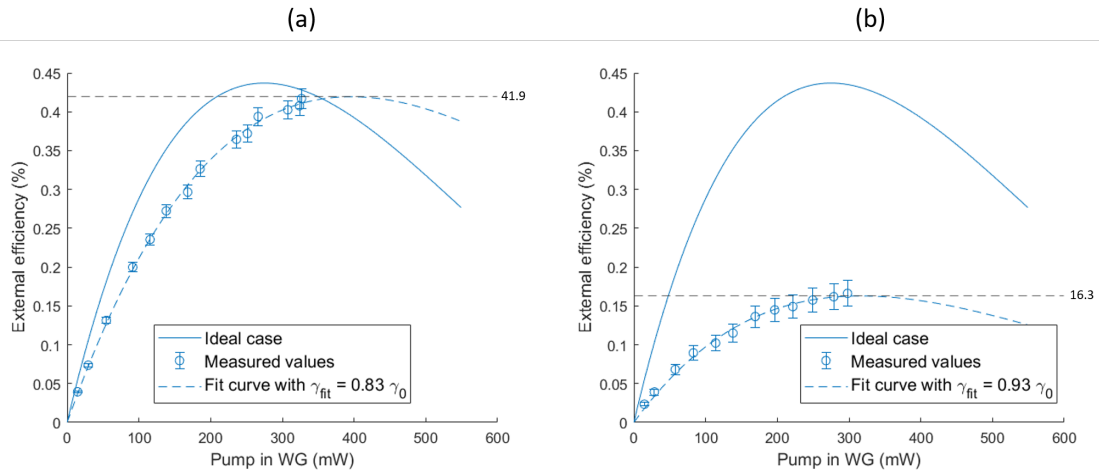


Figure 5.7: (a) DFG end to end efficiency of CW laser light for different pump powers. (b) DFG end to end efficiency of pulsed laser light for different pump powers.

Why is the ideal case different from the fitted curve? There are two differences to be analyzed. The first is that the peak happens at 17% higher pump power for the fitted curve. As studied in section 4.2, width imperfections in the waveguides can account for this difference, as they can make the conversion efficiency more ineffective for a given pump power. There are probably also temperature irregularities in the waveguides which are also decreasing the efficiency. The second difference is that the ideal case has a higher maximal efficiency than the fitted curve. This is because the theory is done for perfect singlemoded light, while there may be higher order modes which are not converted. The ideal curve shows how high the end to end efficiency could be in case of perfect frequency conversion. This is read to be 43.7%. From this analysis it can be seen that improving the internal efficiency will not improve the external efficiency significantly, and that further improvements should therefore focus on minimizing the losses in the optical components of the setup.

For pulsed lasing, a Mira 900 from the company Coherent was used. It had a pulse duration of 3 ps, corresponding to a bandwidth of 110 GHz, or 0.32 nm, and a repetition rate of 76MHz. This was the laser used to excite the quantum dot, which means that the single photons to be converted would be arranged similarly in time. It was therefore interesting to try frequency conversion with it. At first, an average power of 4 mW was sent through the setup. The conversion had a surprisingly rare behaviour. Regardless of the pump power, the conversion efficiency was around 8%, also when there was only about 5 mW of pump power inside the waveguide. Using attenuators to decrease the pump power even more, the conversion began to drop and was then linear with the pump power when it was below 1 mW. This means that the high momentary peak power of the pulses was enough to make the lasers switch roles, such that the input became the pump and the pump became the input. Decreasing the input power of the Mira to 396  $\mu\text{W}$ , the conversion came back to its usual behaviour, which can be seen in figure 5.7b. Unlike with the CTL, the end to end efficiency is maximally  $16.3 \pm 0.5 \%$ , which almost about 3 times less than the ideal case. There can be many reasons for this. One is that the power output of the Mira was highly fluctuating, making alignment optimization very hard. The second may be due to the bandwidth, which was in the same order of magnitude of the FWHM of the conversion, which is  $0.33 \pm 0.3 \text{ nm}$ , as described in section 4.1.

To test the influence of the bandwidth on the conversion efficiency, the Mira laser was sent through a volume bragg grating (VBG), which functions as a spectral filter, reducing the bandwidth. The bandwidth after the VBG was calculated to be 20 GHz. Doing this unfortunately destabilized the power output even more, making the power oscillate with about 30% of its central value. This made alignment optimization in the conversion setup completely impossible, limiting the conversion

efficiency. The end to end efficiency achieved without optimization was of  $26 \pm 10\%$ , with an internal efficiency of  $75 \pm 15\%$ .

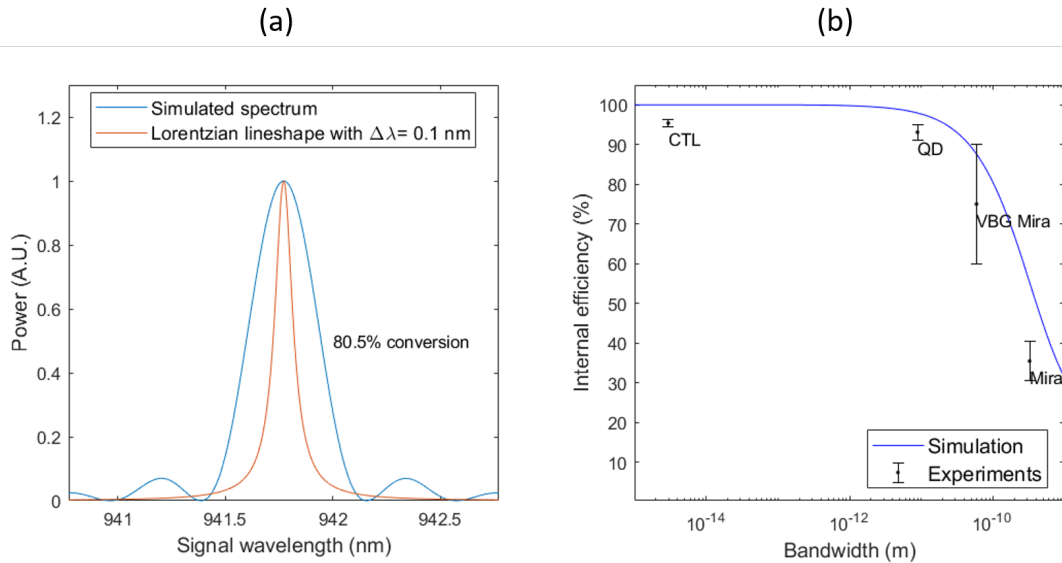


Figure 5.8: (a) Lorentzian shaped curve of bandwidth  $\Delta\lambda = 0.1$  nm compared with the simulated converted spectrum of the experiment. (b) Simulation of the internal efficiency dependence on the bandwidth and its comparison with the measured values for different sources. The internal efficiency in the case of the QD and the non-VBG Mira were never measured, so they are extrapolated from their end to end efficiencies and given a higher uncertainty.

To have an idea of what to expect from the bandwidth dependence, the theoretical conversion efficiency for different bandwidths should be simulated. Here I will assume the spectral shape of the Mira laser to be lorentzian, as it is a common shape for many laser sources. Figure 5.8a shows a lorentzian shape compared to the usual sinc curve obtained from the spectrum simulation. The conversion percentage is obtained by taking the overlap integral between these curves and dividing by the integral of the Lorentzian curve alone. Using this technique, the blue curve from figure 5.8b can be obtained. The conversion efficiency obtained for different sources is then also plotted. It can be seen that none of the sources achieve the theoretical conversion efficiency. For the CTL the reasons can be found in the previous discussion, which are lack of pump power and non-fundamental modes in the waveguide. These factors also affect the conversion of the Mira, especially the higher order modes, as it was harder to align the Mira due to its power oscillations. There is also the possibility that if the spectrum shape is not lorentzian but something else, the calculated probabilities will then also vary. For the broad bandwidth measurements it could also make a difference that there are waveguide imperfections which create an asymmetry in the conversion spectrum. This asymmetry has not been taken into account in the simulation. Even though it is hard to say whether these factors are sufficient to account for the difference between theory and experiments, it can still be confirmed that for bandwidths above 1 GHz the conversion efficiency will decrease, and that this can explain the low internal efficiency of the conversion of the Mira.

### Single photon conversion

The conversion efficiency for the single photon source is one of the most important figures of merit for this thesis, which is why the method for measuring it will be explained in detail in this subsection. Measuring the conversion efficiency for the CTL and Mira lasers was a simple task, as it was possible to place powermeters before and after the setup. Using single photons this is not possible, as the

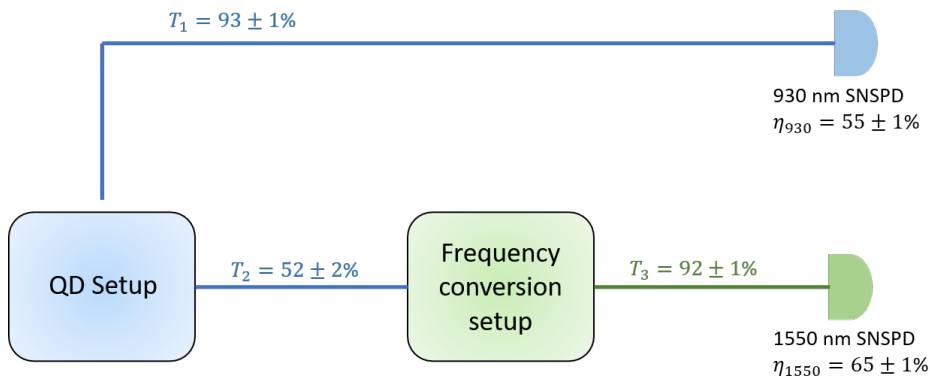


Figure 5.9: Overview of the single photon conversion efficiency measurement. The lines that connect the different blocks represent optical fibers, and the numbers besides them specify their measured transmission.  $\eta_{930}$  and  $\eta_{1550}$  are the detector efficiencies of the 930 nm and 1550 nm SNSPDs respectively.

detection has to be done with SNSPDs, which are located inside a cryostat on a different room. To know the efficiency before and after the setup it is therefore necessary to characterize the losses of the fibers connecting the quantum dot setup and the frequency conversion setup to the SNSPD room. Such fibers are illustrated in figure 5.9. It is also important to extract the constant background coming from the pump photons that manage to couple into the fiber. This background will be analyzed in detail in chapter 6. The end to end efficiency is given by the number of photons converted to 1550 nm divided by the number of photons coming into the setup. Taking all of the losses into account, the count rate at the input can be calculated by the following equation

$$N_{in} = \frac{N_{930} \cdot T_2}{T_1 \cdot \eta_{930}} = (2.20 \pm 0.02) \cdot 10^6 \text{ Hz}, \quad (5.3)$$

where  $N_{930}$  is the measured count rate at the SNSPD, and the remaining quantities are defined in figure 5.9. The converted number of photons right after the setup can be calculated by the following equation:

$$N_{out} = \frac{N_{1550} - N_b}{\eta_{1550} \cdot T_3} = (9.00 \pm 0.15) \cdot 10^5 \text{ Hz}, \quad (5.4)$$

where  $N_{1550}$  is the measured count rate at the SNSPD,  $N_b$  is the measured count rate for the background and the remaining quantities are defined in figure 5.9. The end to end efficiency is then given by:

$$\eta_{ext} = \frac{N_{out}}{N_{in}} = 40.9 \pm 0.8\%. \quad (5.5)$$

The bandwidth of the quantum dots was measured to be of about 500 MHz by looking at its resonance fluorescence on a spectrometer. According to the simulation in figure 5.8b this bandwidth should decrease the internal efficiency by 1% when compared to the CTL. In the measurement it looks like there is a decrease in efficiency, but due to the very high uncertainties it is difficult to confirm. An important value for quantum communications is the total output count rate achieved with this setup. In this case it is  $(9.00 \pm 0.15) \cdot 10^5$  Hz. This number is highly limited by the lossy fiber connecting the QD setup with the frequency conversion setup. Because the cryo time with the source was limited when this experiment was done, there was no time to replace the fiber with a better one. If this fiber were replaced with a less lossy one, the count rate would be of about 1.3 MHz assuming everything else to be the same.

## 5.4 Summary

In the beginning, shortly after achieving DFG for the first time, an end to end efficiency of  $22 \pm 1\%$  was achieved using a CTL laser. Through the introduction of a waveplate in the collection and the use of special alignment optimization techniques, an end to end efficiency of  $41.7 \pm 0.03\%$  was achieved, and an internal efficiency of  $95 \pm 1\%$ , measured with the CTL laser. The main limiting factors for the end to end efficiency are losses in the aspherical lenses and in the output fiber coupling, while for the internal efficiency are limited pump power and multimoded light in the waveguides. The conversion efficiency when converting the light from Mira pulsed laser, which has a bandwidth of 110 GHz, was of  $16.3 \pm 0.5\%$ . This is much lower than for the CTL laser and can be explained by it having a bandwidth in the same order as the conversion bandwidth. Using the quantum dots, the conversion efficiency was of  $40.9 \pm 0.8\%$ , and a count rate of  $(9.00 \pm 0.15) \cdot 10^5$  Hz was achieved.

## 6 Quantum purity

An important requirement of quantum frequency conversion is that the purity of the converted light is as good as what it was before conversion. The purity describes the ratio of the light that comes from the quantum dots with the noise, which is the light coming from other sources. If the light is completely pure, then it will be composed exclusively of single photons traveling in regular time intervals. A good quantity to characterize the single photon purity is the two photon correlation function  $g^{(2)}(\tau)$ , where  $\tau = t - t_0$  and  $t_0$  is the arrival time of a reference photon. For an ideal single photon source,  $g^{(2)}(0) = 0$ , as there should never be two photons arriving at the same time.

This chapter includes a close study of the processes that limit the single photon purity of the frequency conversion output, a detailed explanation of how the two photon correlation function was measured, and a discussion on its results.

### 6.1 Second harmonic generation

Through this chapter it will be proven that the main source of noise in this quantum frequency conversion experiment comes from the second harmonic generation (SHG) created by the pump laser in the PPLN waveguides. This section analyzes the SHG of the pump as an isolated process, and in the next two sections its influence on the main DFG experiment will be studied.

First, by the use of simulations, I tried to estimate the amount of SHG that should be present on the setup if the maximal pump power inside the waveguides that was achieved is present. The theory behind SHG is exactly the same as for SFG and DFG, which was derived in section 2.1 leading to equation 2.18 for its propagation. If the SHG terms of equation 2.5 were used instead, the following propagation equations would be derived:

$$\begin{aligned}\frac{da_1}{dz} &= 2i\gamma_0 a_1^* a_s e^{i\Delta kz}, \\ \frac{da_s}{dz} &= i\gamma_0 a_1^* a_1 e^{i\Delta kz},\end{aligned}\tag{6.1}$$

where  $a_s$  is proportional to the electric field amplitude of the SHG and has a wavelength of  $\lambda_s = \lambda_1/2$ . The conversion rate  $\gamma_0$  is for SHG:

$$\gamma_0 = \sqrt{\frac{2\hbar\mu_0\omega_1^2\omega_s}{Sn_1^2n_2c}}d_{eff}.\tag{6.2}$$

Solving the propagation equations numerically for a given pump wavelength and temperature yields the graph in figure 6.1a, where the amount of SHG power as a function of the propagation distance can be seen. Since the waveguides are not designed to phasematch the SHG process, the converted power does not necessarily increase constantly as a function of the propagation distance, as SHG may be just as probable as its opposite process, downconversion. This can be seen in both the perfect and imperfect cases, where the SHG power oscillates very fast over the course of the plotted propagation distance. The figure shows that the waveguide imperfections add a phase to the oscillations, but make no difference in the maximal achievable power. Despite the bad phasematching and fast oscillations, the SHG power can still be expected to be up to 2  $\mu$ W, simply because there is such a high pump power coupled into the waveguides, but it should also be expected to oscillate constantly due to the equally fast downconversion. The SHG dependence on the pump wavelength is shown in figure 6.1b, where it can be seen that the maximal SHG power is in the range of 1 to 2  $\mu$ W for the wavelengths relevant to this experiment. It can also be seen that the maximal power is exactly the same for all of the wavelengths independently if there are width imperfections or not. The power at the end of the waveguides, which is the relevant output power, should oscillate with the wavelength, giving thin peaks

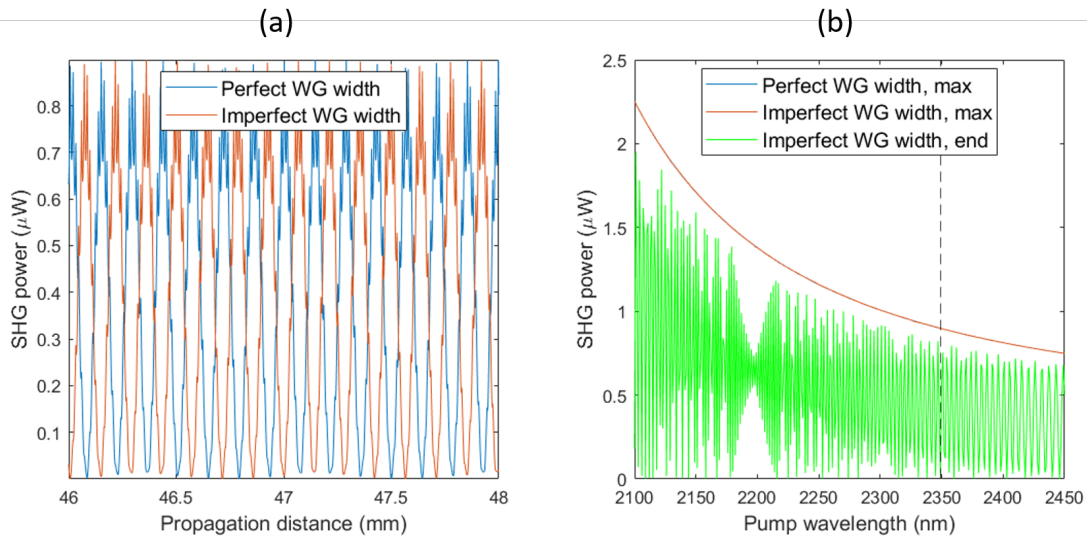


Figure 6.1: (a) Simulation of the SHG power in WG11, assuming a pump power inside the waveguide of 340 mW, a pump wavelength of  $\lambda_1 = 2349$  nm and a temperature of  $T = 50\text{C}$ . The simulation shows the power through the last millimeter of the waveguides. (b) Simulation of the maximum SHG power for different pump wavelengths in WG11. The pump power inside the waveguides is assumed to be 340 mW and the temperature is  $T = 50\text{C}$ . The imperfect width case is simulated using the width oscillations depicted in figure 4.6c

like the ones in the green curve. The SHG was first detected in this setup by using a powermeter with detection range 400 - 1100 nm placed after the waveguides with the pump at full power and wavelength  $\lambda_1 = 2200$  nm. It was confirmed that this powermeter did not register any power if placed before the waveguides, meaning that it was completely insensitive to light at the wavelength of the pump. But when placed after the waveguides and before the prism, it registered a fluctuating and very unstable power in the orders of micro Watts. At this point it was not sure that the detected wavelength was of  $\lambda_s = \lambda_1/2 = 1100$  nm. To confirm this, the light was sent to a spectrometer with a maximal detection wavelength of 1000 nm. The spectrometer did not detect anything, meaning that the light had a wavelength higher than 1000 nm, making it very likely for it to be SHG at 1100 nm.

Having confirmed the presense of the SHG and the possibility to measure it using the 400 - 1100 nm range powermeter, its spectrum was then measured by varying the wavelength of the pump and recording the amount of SHG power. The result can be seen in figure 6.2a. This measurement shows a constant background of a few micro Watts of power for most wavelengths and some peaks with tenths or even hundreds of micro Watts of power. Even though the power meter could seemingly still detect something for wavelengths above 1100 nm, its detection efficiency was limited severely and thus the detected powers should not be trusted and only taken as a reference of where the peaks are located. To measure the SHG at higher pump wavelengths a powermeter with a range of 1200 - 2600 nm was used. Using this powermeter was challenging because if it was placed right in front of the waveguides it would mostly measure the power of the light at the pump wavelength. The measurement of the SHG at these wavelengths was not possible until many months after the first SHG measurement, when a grating and a 1400 nm longpass filter had been installed. The reasons for installing these components are explained in the next section. The grating could effectively separate the pump from the SHG beam, and using a detector card, the position of the SHG beam could be located, allowing to place the opening of the powermeter in that position. The resulting measurement can be seen in figure 6.2b, where the measurement is taken with and without the 1400 nm filter. The measurement with the filter shows the amount of power that comes from the pump, and the difference between the two

measurements should give the power at 1200 nm. The SHG is attenuated by the grating, and its total power can therefore not be used as a reference number. The simulated and measured SHG spectra

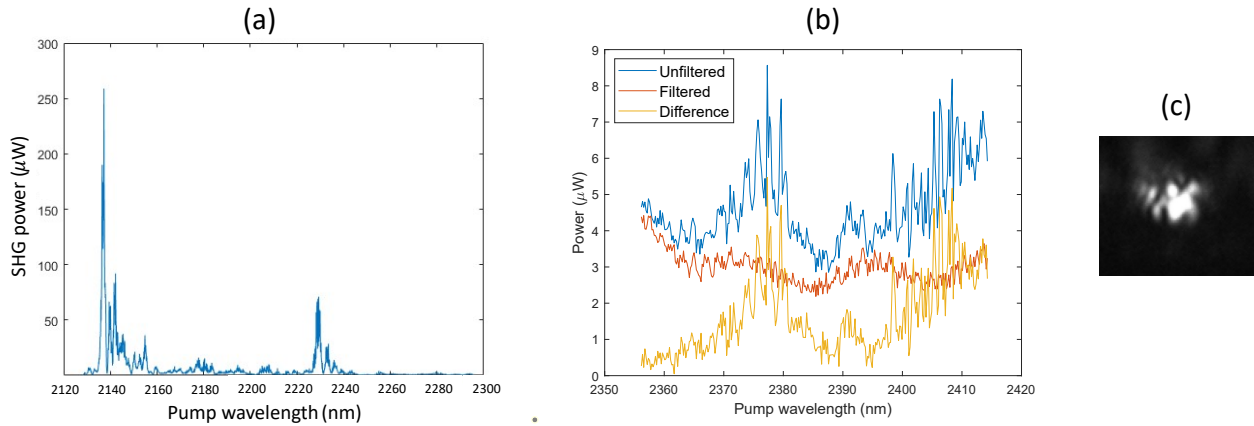


Figure 6.2: (a) SHG power measurement in WG11 for different pump wavelengths using a powermeter with detection range 400 - 1100 nm. (b) SHG power measurement in WG11 for different pump wavelengths using a powermeter with detection range 1200 - 2600 nm at a fixed position after using a grating to separate it from the main pump beam. A 1400 nm longpass filter is used to see the difference between the signal with and without SHG. (c) Camera picture of the SHG.

should now be compared and discussed. The simulation predicted a constant background with small peaks due to phase differences at the end of the waveguides. This is also seen in the measurements, but there are also some very high peaks, not predicted by the simulation. A possible explanation for the unpredicted peaks can be obtained by looking at figure 6.2c, where the camera picture of the SHG light shows that it is highly multimoded. This is because even though the pump beam is singlemoded, due to its high power and the very bad single mode SHG phasematching, there may be some higher order modes that have a better phasematching, since higher order modes have lower effective mode index. These higher order modes were not taken into account due to the simplicity of the simulation, and can introduce an unpredicted amount of SHG. A more complex simulation that takes the higher order modes into account would help clarify whether this is the right explanation.

## 6.2 Noise filtering

To have a high purity of the converted light, it is important that only the single photons at 1550 nm are coupled into the fiber. But there are three other beams that could couple into the fiber, the residual 930 nm beam, the SHG beam and the pump beam. The prism should separate these beams from the 1550 nm single photons such that they do not couple into the fiber, but it happens that the SHG and the pump beams are so strong and defocused that even after being separated by the prism, they still couple a significant amount of photons into the fiber. This section discusses how the noise from these beams was filtered.

### SHG filtering

The count rate of the noise was measured by the 1550 nm SNSPDs when the fiber from the setup was connected to them. When the pump and the signal path were blocked, the noise was measured to be  $(3.5 \pm 0.5) \cdot 10^3$  cps. This is the background caused by the room light that is coupled to the fiber that goes from the setup to the detector room. It can be greatly reduced by using a dark coated fiber. Unblocking the signal path made no difference, as the signal from the quantum dots was too low to couple into the fiber significantly. Blocking the signal path but unblocking the pump made a big

difference. The registered count rate at full pump power was too much to be measured by the SNSPDs, which made them latch. The first attempt to reduce the noise was to add a third dielectric mirror to the collection, which would have a low reflectivity for any beam outside the 1200 - 1700 nm range and also increase the path length allowing for further separation due to the prism. Unfortunately the SNSPDs were still latching after adding this mirror.

Originally when this experiment was designed, there was not expectation that there would be a measurable amount of SHG, and even less that it would affect the main experiment in any significant way. The hypothesis of its presence began after measuring the aforementioned high background counts, which were still present after adding a third dielectric mirror. This suggested that the noise came from a beam with a wavelength close to 1550 nm such that it would not be separated significantly by the prism and also would not suffer significant losses at the dielectric mirrors. These noise background counts could be measured by using ND filters, through which I estimated count rates up to  $4 \cdot 10^6$ . I also observed that the count rate was constantly oscillating, with the oscillation amplitude being up to two orders of magnitude. The experiments described in the preceding section confirmed the presence of SHG in the waveguides, but this did not prove that the noise was at 1200 nm, as it could also be at 2400 nm. So to verify that it was light at the second harmonic wavelength generating the noise, two experiments were made. The first can be seen in figure 6.3a, where the noise was measured while scanning the pump wavelength. If the noise was due to SHG, there would be some high and thin peaks, like the ones in the yellow curve of figure 6.2b, while if the noise was at the pump wavelength the peaks would be broad and short, like the ones in the red curve. The measurement shows that the peaks are high and thin, suggesting that they are due to SHG. The second experiment was to test the amount of noise while varying the power of the pump inside the waveguides. If the noise was SHG, it should be quadratic with the pump power, while it would be linear if it was at the pump wavelength. Figure

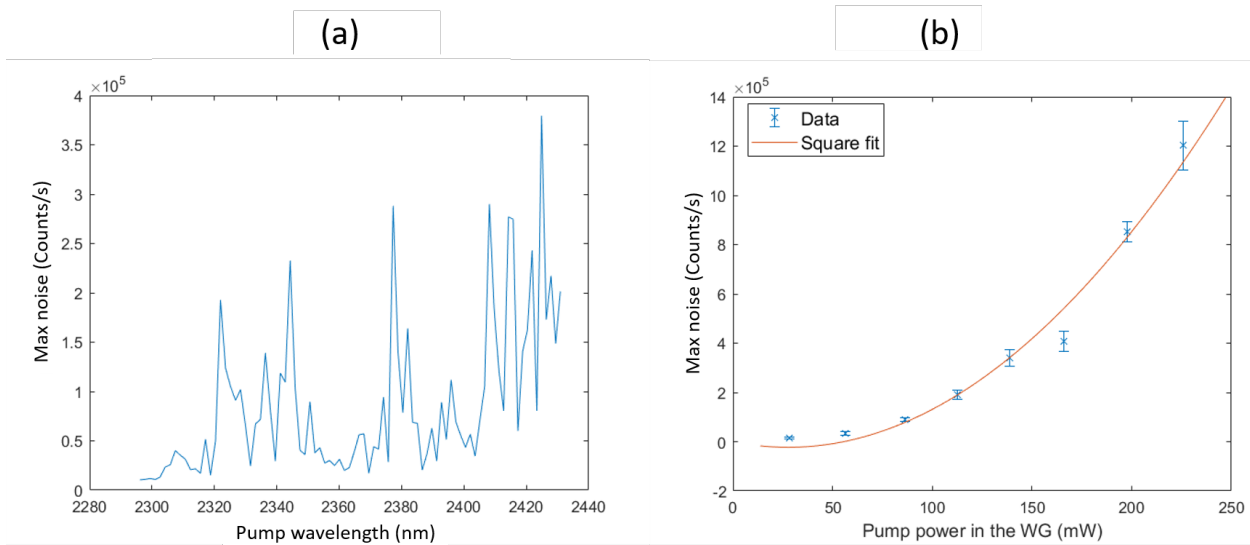


Figure 6.3: (a) Noise intensity in 1550 nm fiber as a function of the pump wavelength when the pump is on but the signal path is blocked. The pump power inside the waveguide is one third of the maximal power. (b) Noise intensity dependence on the pump power for a pump wavelength of  $\lambda_1 = 2360$  nm.

6.3b shows the result of this experiment, together with a second order polynomial fit of the data. The fitted curve goes through 5 out of 8 of the datapoints, which is statistically acceptable, suggesting that the noise level is squared with the pump power, which can only be the case for SHG. These two experiments reaffirmed the hypothesis that the noise was being caused by SHG in the waveguides, and the decision to buy and install a 1400 nm longpass filter was made based on them.

After installing the longpass filter, the noise was again measured using the SNSPDs. This time the

noise at full pump power was in the range of  $4 \cdot 10^4$  cps. To determine the source of the remaining noise, the same experiments of figure 6.3 were repeated. Figure 6.4a shows that the spectrum in this case resembles a lot the spectrum of the pump after the waveguides when measured using the powermeter. Figure 6.4b shows that the noise is linear with respect to the pump power. These experiments suggest that the remaining noise in the fiber comes from light at the wavelength of the pump.

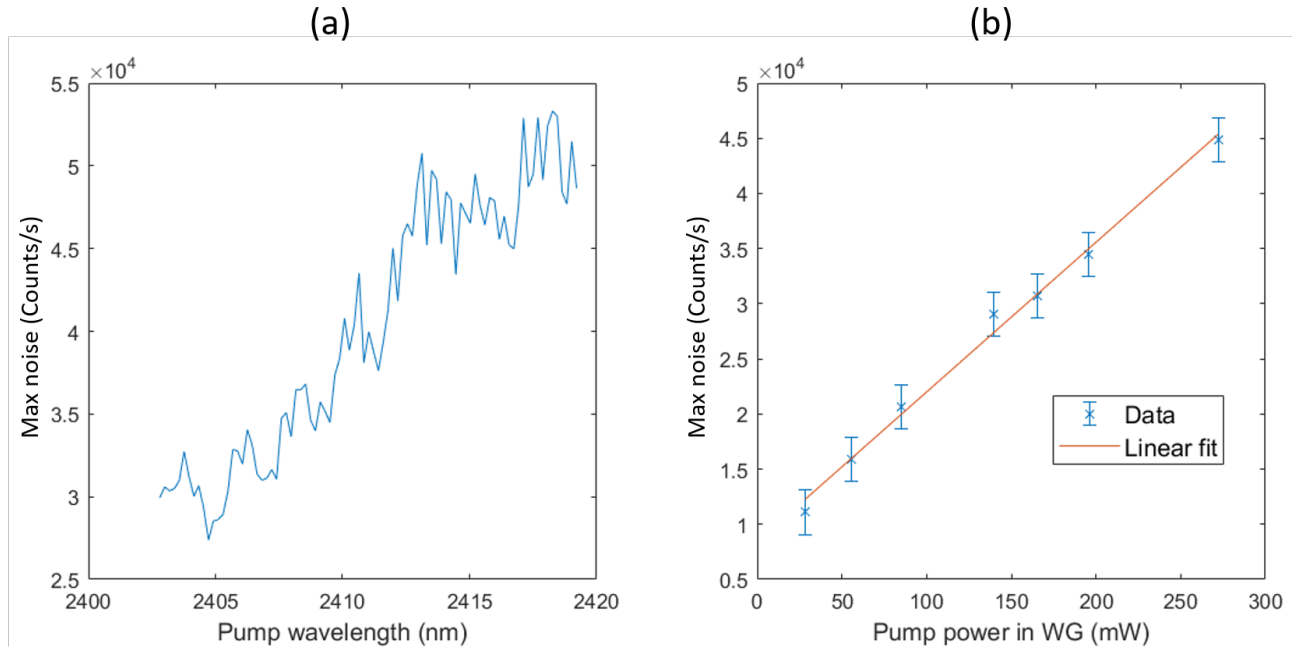


Figure 6.4: (a) Noise intensity in 1550 nm fiber as a function of the pump wavelength when the pump is on but the signal path is blocked and a 1400 nm longpass filter has been installed. (b) Noise intensity dependence on the pump power for a pump wavelength of  $\lambda_1 = 2420$  nm with the longpass filter installed.

### Pump filtering

Adding the longpass filter helped reduce the noise by about two orders of magnitude. To reduce the noise even more, the signal coming from the pump had to be suppressed as well. A straightforward solution would have been to install a shortpass filter with a very high transmission for everything below 1700 nm and a high attenuation for everything above that wavelength. Unfortunately it was not possible to find a filter meeting both conditions at a reasonable price. As an alternative, a blazed reflection grating was used to replace the prism for wavelength separation. The point was that such a grating would separate the different wavelengths of the light significantly more than the prism, making it impossible for the pump to reach the fiber. The disadvantage of using such a grating was that due to higher order reflections, there would be extra losses of the light at 1550 nm.

Replacing the (transmission) prism with a reflection grating meant that the shape of the collection path would have to be slightly adjusted. The resulting path with the grating installed can be seen in figure 6.5a. Before testing the signal on the SNSPDs, the setup was tested using the CTL and regular powermeters first. The end to end conversion efficiency was determined to be  $40 \pm 1\%$  at maximum, with an internal efficiency of  $95 \pm 1\%$  (the same as with the prism). The reflectivity of the grating at 1550 nm was measured to be  $92 \pm 1\%$  by using the 1550 nm diode laser. Compared to the prism, which had a transmission of  $95.3 \pm 0.8\%$ , there is about 3% more loss introduced by using the grating, which explains the 1% reduction in the end to end efficiency.

The use of the grating together with the CTL lead to a bonus discovery, which is the fact that there is a small amount of cascaded non-linear effects in the waveguides. This is due to the combination of the SHG at around 1200 nm with the DFG at 1550 nm, through the process of SFG resulting in a wavelength of about 676 nm, which is visible red light. Another combination is the SHG together with the residual 930 nm signal through SFG resulting in a wavelength of about 525 nm, which is visible green light. Both combinations happen in the waveguide, and thanks to the grating they are clearly separated, as can be seen in figure 6.5b, where there are some clear red and green dots reflected on a regular piece of paper (not a detector card). Their power output was measured with a powermeter, but they were too dim to be measurable. It can be estimated that their power output is below 0.05% of the power input at 930 nm. This means that they are irrelevant for the main experiment, as there is only a negligible amount of the 930 photons that end up being converted to visible light.

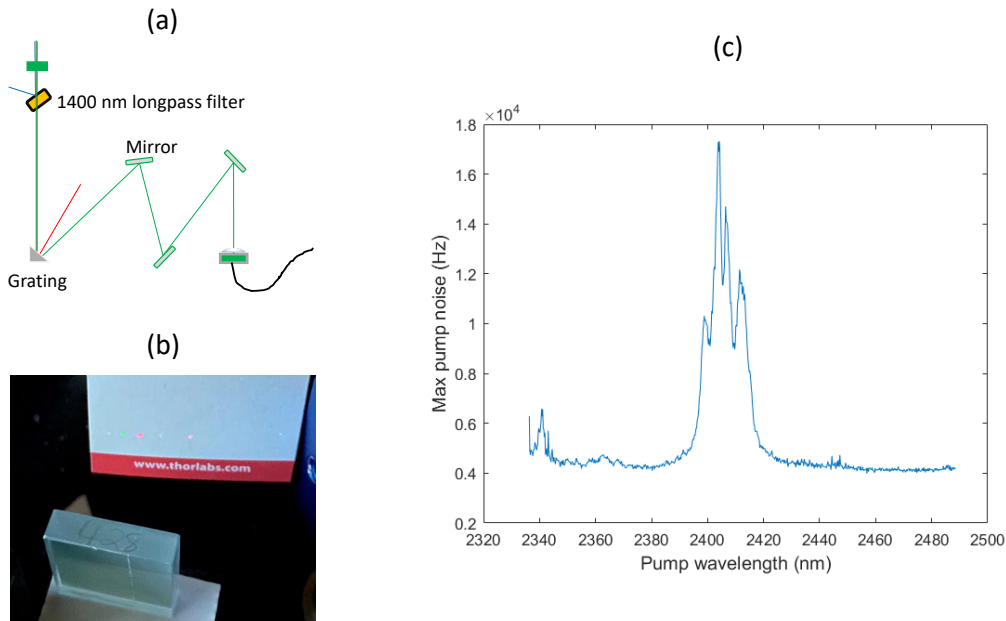


Figure 6.5: (a) Sketch of the collection path after replacing the prism by a reflection grating. (b) Grating reflection on a regular piece of paper of the converted light from the CTL. (c) Maximal pump noise in fiber as a function of the pump wavelength measured in the 1550 nm SNSPDs, using a 1400 nm longpass filter and a reflection grating.

The pump noise was measured on the SNSPDs after using the grating. The measurement was taken using WG11 at a temperature of  $T = 48$  C, which meant that the optimal pump wavelength for frequency conversion was 2398 nm. At this wavelength the noise was of about  $1 \cdot 10^4$  cps, which is about one fourth of what it was when using the prism. The noise spectrum as a function of the pump wavelength was also measured for this case and can be seen in figure 6.5c. Here it can be seen that there is a clear peak in the range of 2380 - 2420 nm, and then the noise is equal to the background noise for almost all of the other wavelengths. This can be explained by there being many high order reflections of the pump, which are heavily attenuated but still present, and one of those reflections is the one that can be seen in the spectrum. This means that the grating separates the main beam of the pump enough for it not to couple into the fiber, but it in turn introduces higher order reflections which still produce noise. In any case, for any part of the spectrum the noise is always less for the grating than for the prism.

It can be concluded that the grating reduces the noise from the pump that is coupled into the fiber by at least a factor of 2, but it also reduces the end to end efficiency by about 1%. Its usefulness therefore needs to be determined by the specific application that the frequency conversion setup is

applied for. A comparison of these devices is summarized in table 2.

Device	End to end efficiency	Max Noise	Output bandwidth
Prism	$41.7 \pm 0.3\%$	$7.8 \cdot 10^4$ Cps	25 nm
Grating	$40 \pm 1\%$	$1.6 \cdot 10^4$ Cps	0.3 nm

Table 2: Comparison of the prism and the grating. A high end to end efficiency and output bandwidth is desired while keeping the noise level as low as possible.

### 6.3 Hanbury-Brown and Twiss experiment

The purity of the single photon states of light can be measured by the Hanbury Brown and Twiss (HBT) experiment [5], which consists on sending the light to be analyzed through a beam splitter and measuring the photon correlation between the two output ports for different time delays. This section contains the results of such an experiment for the light from the quantum dot before and after conversion, to investigate if the frequency conversion process has an influence on the fidelity of the single photons' quality.

The apparatus used for the HBT experiment are illustrated in figure 6.6. After the frequency conversion a 50:50 fiber beam splitter is used to create a superposition between the two output paths. This superposition collapses upon measurement with the SNSPDs, and in the case of one photon states, only one of them should click at a time. A time tagger (TT) is used to monitor the detection times of each detector. At last the detection times are analyzed to get the amount of times the detectors click simultaneously (coincidence counts) for a given time delay.

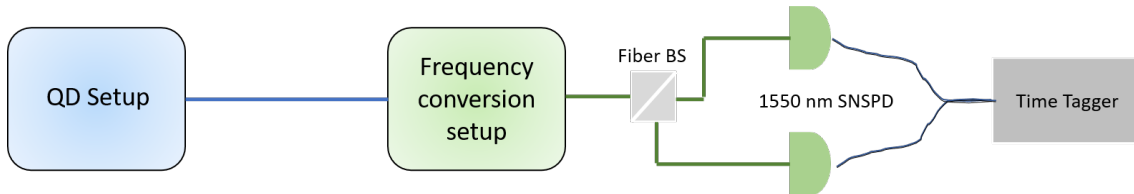


Figure 6.6: Overview of the apparatus required for the HBT experiment.

The HBT experiment for the light before conversion was made by using a Swabian TT 20, while the measurement for the light after conversion was made by using a PicoHarp TT. The only reason for this difference was the short time period where the quantum dot was available for use during this project, and at the time of the experiment there was a Swabian TT connected to the NIR beam splitter, while a PicoHarp TT was connected to the telecom beam splitter.

#### Purity of the light before conversion

The result of the HBT experiment for the light before conversion for a broad time delay span can be seen in figure 6.7a. If zoomed, the blue area can be revealed to be made of peaks of width  $\approx 2$  ns and spaced with  $\approx 13.2$  ns between their center, which coincides with the repetition rate of the pulsed laser used to excite the dot. Ideally for single photons at large time delays, the height of the peaks should be constant, only subject to small fluctuations. The measurement on the other hand shows the peaks are higher in the center (for short time delays), while it becomes flat toward the sides (for large time delays). This is phenomenon is called blinking, it is caused by an alternative decay path in the QD and amplified by an artifact error in the Swabian TT [20]. Its consequences are that to estimate the ratio of the central (missing) peak to one of the other peaks, a peak outside of the blinking area has to be chosen. A zoomed version of figure 6.7a is shown by the blue dots of figure 6.7b. The central

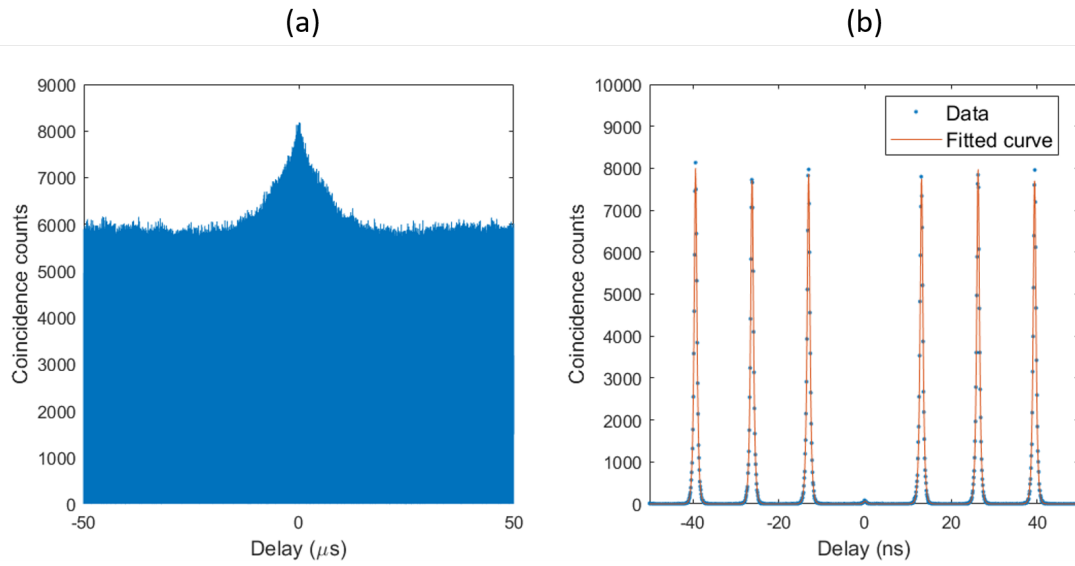


Figure 6.7: (a) Two channel coincidence count measurement for a HBT experiment of the QD light before conversion. (b) Coincidence counts of the 6 peaks closest to the zero time delay peak.

peak can be seen to be heavily attenuated compared to the neighboring ones. This is the indicator that the light of the quantum dot is composed almost exclusively of single photon states, as there are very few occasions where the detectors click simultaneously. The two photon correlation function  $g^{(2)}(\tau)$ , where  $\tau$  is the time delay, can be derived to be a double sided exponentially decaying function [20], with the decay rate equal to the QD's spontaneous decay rate, assuming that the Rabi frequency and the dephasing rate are much smaller than the spontaneous decay rate. This means that there should be a high coincidence rate for the time delay being equal to  $nt_{rep}$ , with  $t_{rep}$  being the repetition rate of the laser, and it should decay exponentially to both sides with a decay rate  $\gamma$  equal to the spontaneous decay rate of the quantum dot. In practice the coincidence count rates are also affected by the instrument response time of the SNSPDs and the TT which is described by an instrument response function (IRF), and will be assumed to be Gaussian with a characteristic response time  $\sigma$ . The measured peaks can therefore be modelled by a double sided exponential decay convoluted with a Gaussian function. By this argument, a model of the central peak plus its 6 adjacent peaks is given by the following function

$$f(\tau) = \left( a_0 e^{-\gamma|\tau|} + a e^{-\gamma|\tau - nt_{rep}|} + c \right) \otimes e^{-\frac{1}{2}\left(\frac{\tau}{\sigma}\right)^2}, \quad (6.3)$$

where  $a_0$  is the amplitude of the central peak,  $a$  is the amplitude of the side peaks and  $c$  is the average coincidence counts caused by background and dark counts. This was used to fit the measured data and the result can be seen as the orange line of figure 6.7b. The fitted function was then used to calculate the area under the central peak and compare it to the area of a peak 40  $\mu\text{s}$  away from it (to avoid the effect from blinking). The  $g^{(2)}(0)$  can then be calculated to be

$$g^{(2)}(0) = \frac{A_0}{A_{40}} = (9.3 \pm 0.4) \cdot 10^{-3}, \quad (6.4)$$

where  $A_0$  is the area of the central peak and  $A_{40}$  is the area of the peak at 40  $\mu\text{s}$  delay. In both cases the background counts and the influence from the other peaks were subtracted when calculating the area.

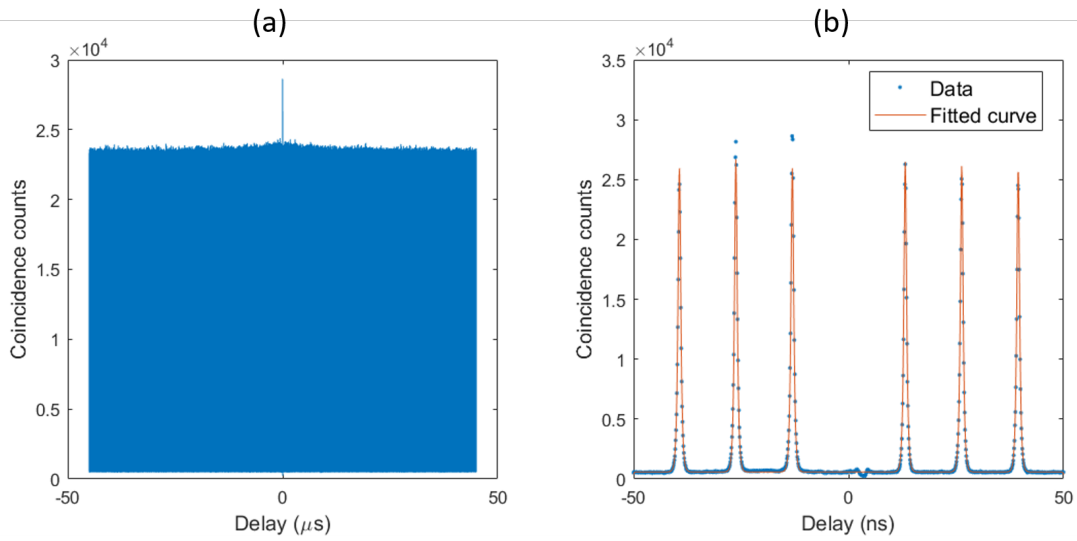


Figure 6.8: (a) Two channel coincidence count measurement for a HBT experiment of the QD light after frequency conversion. (b) Coincidence counts of the 6 peaks closest to the zero time delay peak.

### Purity of the light after conversion

The HBT experiment for the converted light was done using the prism and not the grating in the collection. Due to the short time where the source was available during the experiment, it was not possible to try both. The experiment result is plotted in figure 6.8a. In contrast to figure 6.7a, the central peak values are not so different from the values for long time delays. This is probably due to the fact that the blinking of the quantum dot is not amplified by the PicoHarp as it was by the Swabian, even though it is still there because it is an intrinsic property of the QD. A zoom for small delay times is shown with the blue points in figure 6.8b, while the fit result using the function in equation 6.3 is illustrated by the red line. The central peak in this case is completely gone, and  $a_0 = 0$  in the fit result. Even though this may seem as a positive result at first sight, the reason for it is that the noise level has about 2% the height of the peaks, making the central peak invisible.

The HBT measurement after conversion was done for an integration time of 20 minutes. For the measurement to be reliable, it was important for the frequency conversion setup to be stable over this time scale. The steps taken to achieve conversion stability over time scales below 1 hour are discussed in the next chapter.

Figure 6.9 compares the noise level around  $\tau = 0$  (blue line) with the expected central peak (yellow line) assuming that it conserves its shape and height after conversion. It can be seen that the noise has more than twice of the coincidence counts than the assumed maximal value of the central peak. The noise level if the grating were used instead is what can be seen from the red curve, which was measured on a separate experiment, where the mira was used instead of the source, since the later was not available. The central peak in the case of the mira is just a regular high peak and not very interesting, thus the red curve is a plot of the noise for a region without a peak. According to these experiments, the noise level in the HBT measurement would be 60 times smaller if the grating was used, which would then make the central peak of the source measurement clearly visible.

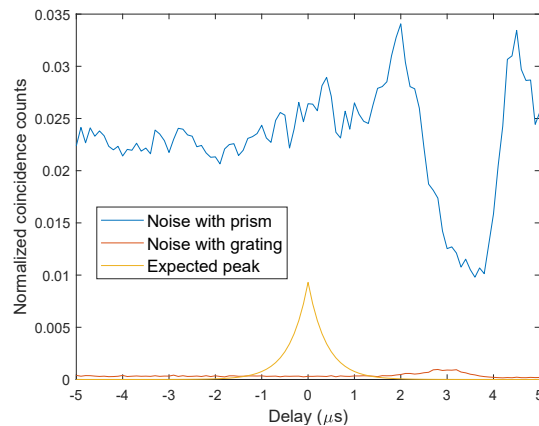


Figure 6.9: Blue curve: Zoomed version of the blue points in the center of figure 6.8b, Red curve: Noise level in HBT experiment for mira (pulsed) laser light conversion, Yellow curve: central peak shape for the unconverted light. The coincidence counts are normalized to peaks far away in each of their respective measurement.

It is not possible to accurately estimate the value of  $g^{(2)}(0)$  if the central peak is not visible. If the noise in the central area is integrated, a higher bound for the  $g^{(2)}(0)$  can be obtained using eq 6.4, which in this case is around  $g^{(2)}(0) = 0.1$ . But this does not tell anything about the state of the converted photons, as the result is uniquely determined by the noise level. A more suitable choice for an upper bound could be to assume that the central peak has exactly the height as the noise, which is to set  $a_0 = c$  in equation 6.3. Calculating the area of this peak, the upper bound for the  $g^{(2)}(0)$  value is

$$g^{(2)}(0) = 0.018 \pm 0.001 \quad (6.5)$$

## 6.4 Summary

For the main experiment of DFG, a high pump power is required. This chapter presented predictions and measurements of the impurities caused by having such a high power laser when trying to produce single photons. First there is the fact of having SHG, which was simulated and then measured to be present in significant amounts (up to hundreds of micro-Watts in strength). The SHG wavelength is of around 1200 nm, which is not as far away from telecom wavelengths as the other wavelengths present in the setup. This means that it has a narrow separation due to the prism, a low attenuation in a 1550 nm meter fiber and a high detection efficiency for 1550 nm detectors. The SHG manifested as a source of noise in the count rates of the SNSPDs, and was eliminated by using a 1400 nm longpass filter. The noise was not completely suppressed by this addition, as it turned out that there was also noise photons at the wavelength of the pump. The use of a grating instead of a prism could reduce the noise level by at least a factor of 4.

The single photon purity, measured by the two photon correlation function at zero time delay  $g^{(2)}(0)$ , is  $(9.3 \pm 0.4) \cdot 10^{-3}$  before conversion and  $0.018 \pm 0.001$  after conversion. The later is an upper bound, where the real value was not possible to measure due to there being too much noise from the pump. From this experiment it is not possible to know if the frequency conversion process alters the state of the single photons after they are converted, which should instead be possible by repeating the experiment with the grating installed in the frequency conversion setup.

## 7 Stability and indistinguishability

Indistinguishable single photons at a stable count rate are very important for applications like quantum teleportation [22] and quantum computation [3]. Therefore it is desired for the output of frequency conversion setup to be indistinguishable photons at a constant count rate. The first part of this chapter explores some of the factors that may influence the stability of the count rate. The second part discusses the factors that may influence the indistinguishability and describes a Hong-Ou Mandel (HOM) experiment for how to characterize the indistinguishability of the converted photons.

### 7.1 Efficiency stability

In chapter 5, an end to end efficiency of  $40.9 \pm 0.8\%$  was reported. This number is a maximum produced when all physical parameters are at their optimal value, but over time the end to end efficiency will drop due to many parameters deviating from their optimal values. Drifting in the following parameters have a tendency to decrease the end to end efficiency over short time scales:

- **Input light polarization:** Given that the laser sources (CTL and 1550 nm laser diode) and the single photons from the QD are connected to the setup through optical fibers, their polarization fluctuates constantly, deviating from the desired TM mode. Such deviations can always be corrected by adjusting the waveplates in the input, but over time there is no way to guarantee that the polarization will not drift. An attempt to minimize the drift of the polarization was made by installing a polarization maintaining (PM) fiber for the coupling into the setup, but if the light before such a fiber has a fluctuating polarization, it will still fluctuate on the output. The effect of the polarization drift is visible over the course of many minutes, and can decrease the converted output power by up to 10%. This problem could be solved by installing PM fibers all the way from the QD to the setup or with an active polarization stabilization loop, but was tackled by adjusting the waveplates before any measurement.
- **Pump power:** The output power of the pump oscillates over time. The oscillations have a period that increases over time, which is about 10 minutes shortly after turning the laser on and about 1 hour after a full day of operation. The amplitude of the oscillations are of about 10% of the total power. The converted output power falls about 2% when the pump power decreases with 10% (assuming pump power inside the waveguides is originally at the maximum I could achieve). This problem was circumvented by not taking measurements shortly after turning on the laser.
- **The mysterious non-linear effect:** The main source of efficiency drops is an effect of unknown origin, which decreases the converted output power with up to 35% over time. This effect will here be denoted as the mysterious non-linear effect (MNLE), and most of this section will describe the experiments I did to characterize it and how it was suppressed in practice.

These effects act over time scales of below one hour. Over time scales of many hours or days the efficiency also drops due to alignment drifting of the optical components. I have not tried to solve this issue, which means that the setup requires daily alignment for it to keep working efficiently.

#### The mysterious non-linear effect

An example of the frequency conversion power output over the course of many minutes is illustrated in figure 7.1. The output power is not constant, with small oscillations happening continuously and clear drops every several minutes. The drops in the figure can be of 30% of the maximum value and they only happen when there is a high pump power in the waveguides ( $P_1 > 100mW$ ). In situations where the output power dropped, I repeatedly tried to restore it by adjusting the input waveplates and

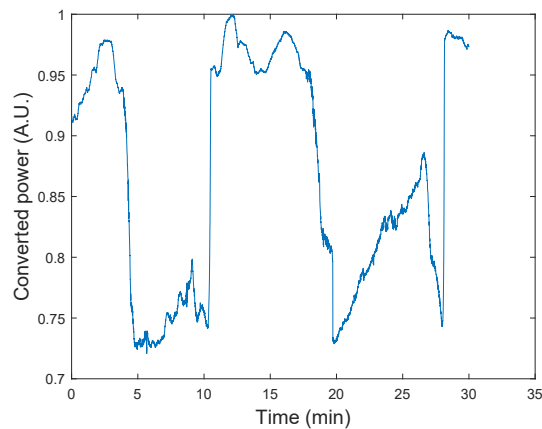


Figure 7.1: Output of frequency conversion of WG11 output over time. The CTL was used to provide the input light at 942.02 nm.

realigning the setup. I realized that this could maximally restore up to 10% of the power, which was not enough when the drops were of 30%. The pump power was also measured in times corresponding to the drops and no correlation was observed between the output power drops and the oscillations of the pump power. The only way to restore the converted power to the maximum was to make a pump wavelength scan and set the pump wavelength to the optimal. This suggested a link between the wavelength of the pump and the output power drops. Figure 7.2 gives a different view of the

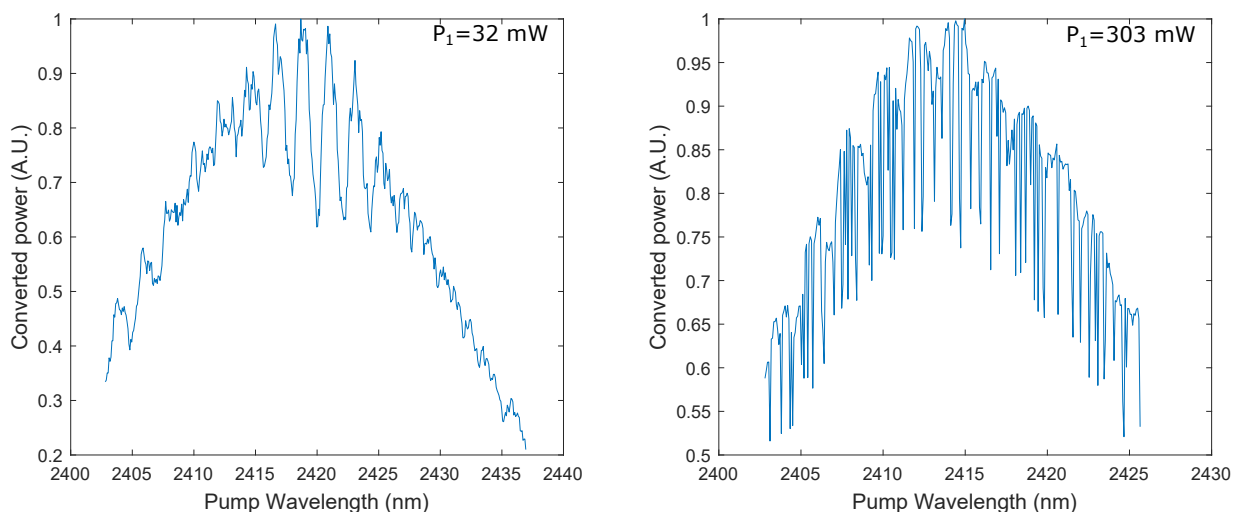


Figure 7.2: (a) Converted power versus pump wavelength for a wavelength scan at low pump power in the WG, indicated in the figure as  $P_1$ . (b) Same scan with higher pump power in the WG.

MNLE. Making a low power pump wavelength scan gave the spectrum shown in figure 7.2a. This spectrum had some fringes, which if the scan was done again, would be in the same position for the same wavelengths and have the same shape. Such fringes arise from instabilities on the pump power, as can be seen in figure 3.6a, since at low pump powers the converted power output is linear with the pump power. The same scan with all parameters kept constant except for the pump power in the waveguide is shown in figure 7.2b. This scan shows some clear drops, and if the scan was done again the drops would not be at the same wavelengths. As explained in chapter 3, the pump power in the waveguides was controlled by attenuating it via a PBS, which means that the power at the output of

the IPG laser was not altered.

To prove that the low power fringes were caused by fringes in the pump power while the high power ones were not, a pump wavelength scan was done, where the pump power after the waveguides was measured. This pump power should be proportional to the one inside the waveguides. The result for low input pump power can be seen in figure 7.3a, where the fringes can be seen to correspond to the ones in figure 7.2a. The same experiment result at high input pump power is seen in figure 7.3b, which is similar to the low power case, but not to figure 7.2b, suggesting that the pattern in the conversion spectrum at high pump powers is not related to the input pump power spectrum.

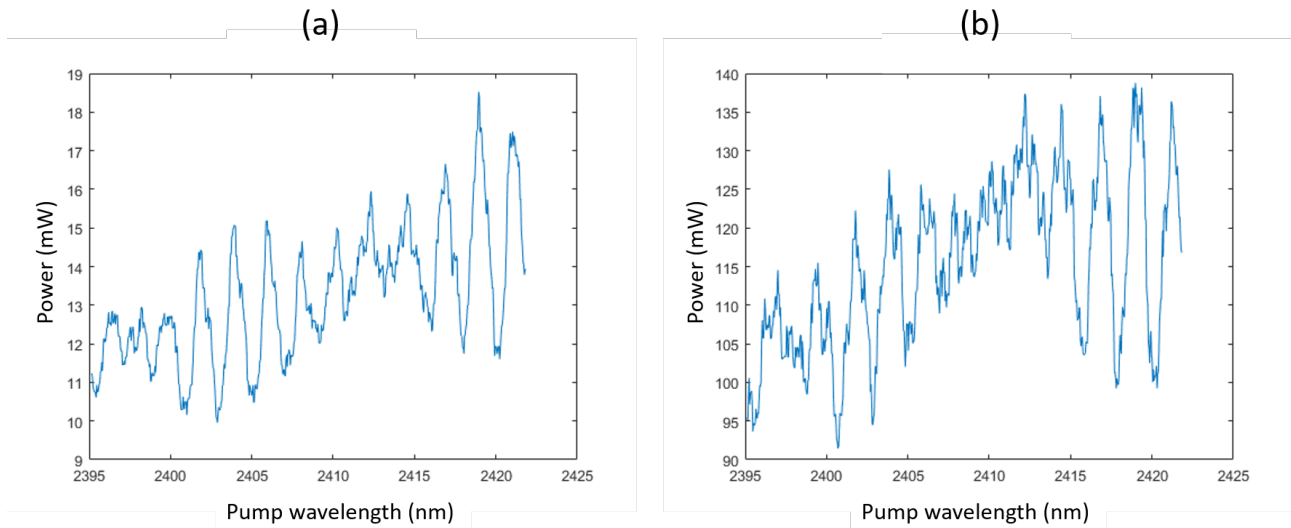


Figure 7.3: (a) Pump power measured right after the output aspherical lens of the waveguides during a wavelength scan of the pump at low input power. (b) Same measurement at high input power

Figure 7.4a shows a pump wavelength scan similar to the one in figure 7.2b, but this time the residual light's power was simultaneously monitored. It can be seen that the converted and residual light are anticorrelated, such that the residual light has peaks where the converted has drops. This shows that whatever the problem is, it is related to the conversion process inside the waveguides, and is not related to misalignments or absorptions in the setup. The problem is thus non-linear in nature, as it depends on the pump power and is directly related to the frequency conversion process. Thus the "non-linear" part of the name.

An experiment to test how the efficiency drops relate to the drifting of the pump wavelength over time was also made. This was possible by observing that the MNLE is also present for SFG, which has an output wavelength in the NIR region, measurable by the wavemeter that was available in the laboratory. The experiment consisted in monitoring the converted SFG power while also measuring its wavelength by using a beam splitter in the collection. The result can be seen in figure 7.4b. Both the wavelength and the converted power jump every few minutes, and have periods of slow change or stability in between. The jumps happen simultaneously, but have no correlation in their size or their sign, as it is assumed that the 1550 nm laser was stable over this period of time. This suggests that the mechanism responsible for the wavelength jumps inside the pump is also responsible for the conversion efficiency drops. It is known that the wavelength jumps happen due to longitudinal mode hopping inside the pump laser cavity, suggesting that the conversion efficiency drops when the pump light is multi-moded. It should be mentioned that the difference in frequency of two modes is in the range of 20 pm as can be calculated from figure 3.6b, which compared to the pump bandwidth of 25 nm measured in section 4.1 should be insignificant. This means that from the perspective of the DFG theory derived in chapter 2, having multi-moded pump light in this case should make no difference

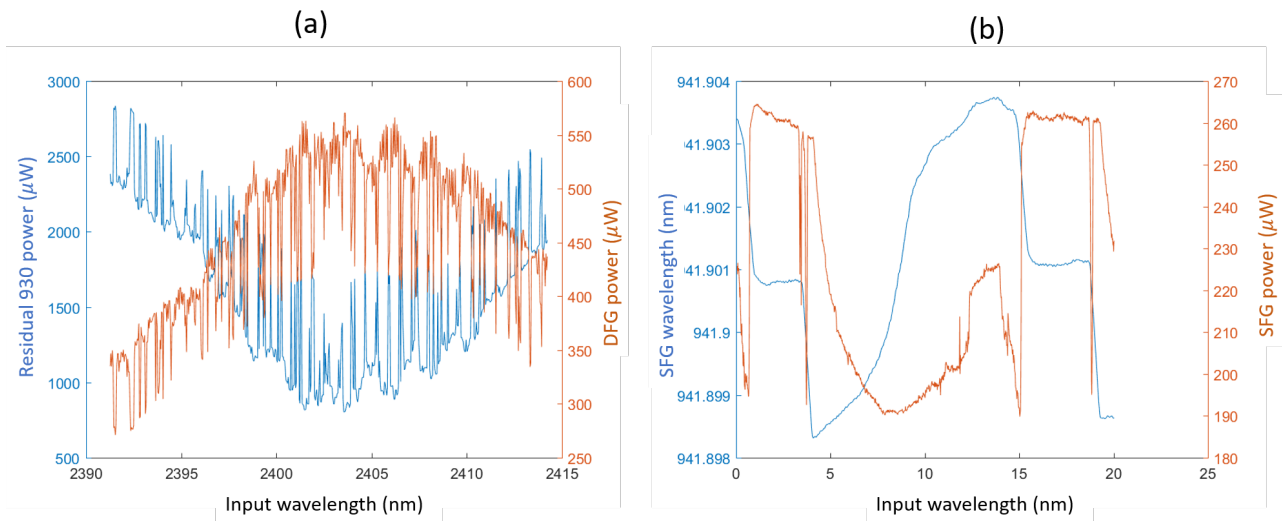


Figure 7.4: (a) Converted and residual power versus pump wavelength for a wavelength scan at high pump power in the WG. (b) SFG pump scan where the output wavelength is monitored simultaneously using a wavemeter.

for the conversion efficiency.

### Suppressing the MNLE

To keep the promise of an end to end efficiency above 40% it is important to suppress the MNLE. Otherwise the efficiency will drop to 30% in a regular basis, and to 25% at some instances. The first method that I implemented to suppress the MNLE was a temporary solution where the output power was monitored, and if it fell below a threshold, a programmed optimization routine would be activated until it was above an acceptable value again. An example of what the converted power would be over long time periods with such an algorithm can be seen in figure 7.5a. In the figure it can be seen that there were many places where the efficiency would have dropped, but the algorithm was activated such that this did not happen. There were two problems of using such an algorithm to suppress the MNLE. The first is that it could not know whether the drops were due to the MNLE or to other factors such as polarization or pump power. This made it hard to make an algorithm clever enough to always keep the MNLE at a minimum. The second problem was that the output wavelength would slightly change for every time the algorithm was activated, making the output photons distinguishable.

A better solution was found when contacting the manufacturer about the fringes in the pump power spectrum. They mentioned that the fringes were due to longitudinal mode hopping inside the pump laser cavity, which apart from decreasing the pump power, also could make the pump light multimoded. The solution for this issue, as was also mentioned in chapter 3, was to tune piezo 2 and 3 inside the laser such that the pump power output at the given wavelength was maximized. Because piezo 2 was malfunctioning I could only tune piezo 3, but luckily it was enough to tune piezo 3 to maximize the pump power, which also meant constraining the cavity to longitudinal single mode operation. The surprise was that apart from optimizing the pump power at the required specific wavelength, the tuning of piezo 3 also eliminated the MNLE. A plot of the converted power with time after tuning of piezo 3 can be seen in figure 7.5b. The abrupt drop and rise after 13 minutes is due to polarization optimization at that moment. It can be seen that the converted power oscillations are much smaller than before the piezo optimization, and they are mainly caused by fluctuations in the polarization of the input light. It is therefore highly probable that suppressing the multimode operation of the pump laser also suppressed the MNLE in the waveguides.

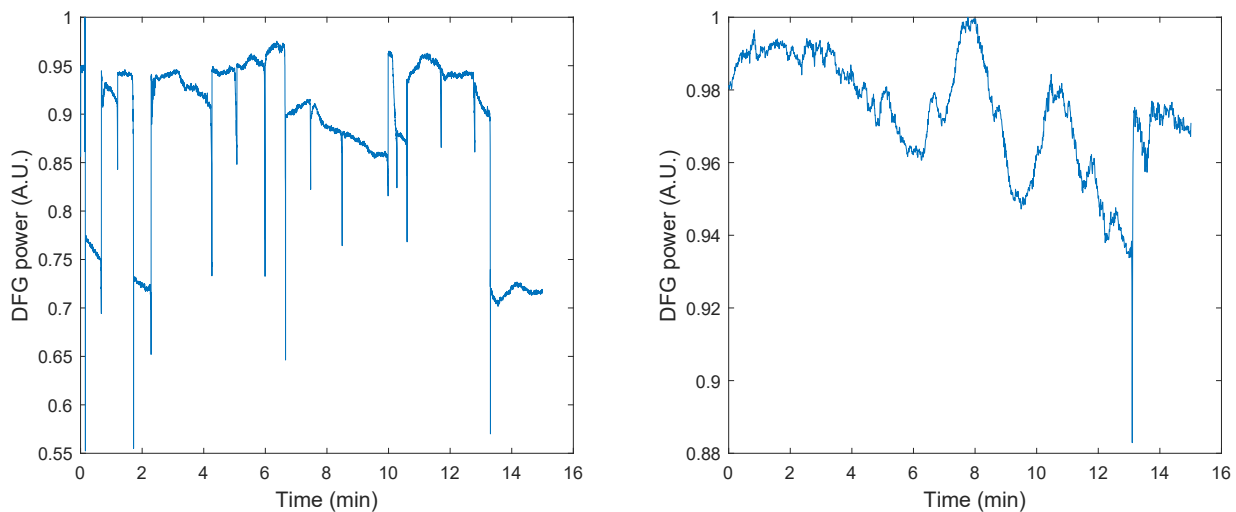


Figure 7.5: (a) Converted power over time with an automated algorithm that corrects for the drops due to the MNLE. The pump power was  $P_1 = 320mW$  (b) Converted power over time after optimization of piezo 3.

The effects of the MNLE and the way to suppress it have now been explained. Its physical explanation is though still unexplored. To find an explanation for it, I conducted a series of experiments and simulations. These are explained in detail in appendix D, where the most likely explanation is found to be photorefractivity due to interference of the longitudinal modes of the pump.

## 7.2 Indistinguishability

Two photons are said to be indistinguishable if they can create perfect constructive or destructive interference with each other when they overlap in space and time. When using quantum dots as single photon sources, the emitted photons can acquire distinguishability from each other due interference of the QDs with electric charges or magnetic fields in the material. These effects have been suppressed in the device containing the QDs, and an intrinsic HOM visibility larger than 96% was measured [7]. When doing frequency conversion, there are some extra factors that will influence the indistinguishability of the converted photons. The following is a list of the factors that may have an influence:

- **Pump wavelength:** For the output photons to be indistinguishable, it is important that they have the same wavelength. The wavelength of the converted photons is directly dependent on the wavelength of the pump. If the wavelength of the pump drifts or jumps constantly over time, the output photons will become distinguishable. The drift in the wavelength output can be measured by doing SFG and measuring the output wavelength with the wavemeter as in figure 7.4b, where it was done shortly after turning on the pump and before mode stabilization through optimization of piezo 3. If the modes are stabilized and the measurement is taken at least 3 hours after turning on the pump, I have measured that the pump wavelength will only drift with up to 20 pm over the course of one hour, and fluctuate with up to 50 fm within one second, which corresponds to a frequency drift of about 20 MHz for the output light. Over the course of 100 photons the wavelength will therefore change with up to 20 Hz, which should be negligible compared to the bandwidth of the quantum dots of 500 MHz.
- **Single-moded pump light:** The pump can do mode hopping, which sometimes leads to two-moded light with two frequencies. This would create also two frequencies of the output

photons, which would be separated by about 0.9 GHz (figure 3.6b) and should therefore be distinguishable. The mode hopping can be reduced by optimizing piezo 3, and maybe if piezo 2 could be optimized it could be completely eliminated, so it is very important to do this optimization to get indistinguishable photons.

- **Polarization stability:** If the polarization is constantly fluctuating it will influence the indistinguishability of the input photons. Fortunately only the TM mode of the photons gets converted, so polarization fluctuations may decrease the efficiency but not the indistinguishability, so the output indistinguishability will not suffer from this.
- **Setup time drift:** Every optical component that the light has to go through can alter the wavepacket of a single photon, and if this alteration fluctuates with time, the photons may become distinguishable. This effect cannot be suppressed and it is therefore natural to expect that the converted photons will be more distinguishable than the unconverted ones, but the degree of the difference can be expected to be low, as the fluctuations in the setup are mostly due to temperature fluctuations, which should be negligible over timescales of 1  $\mu$ s (100 photons).

### Hong-Ou-Mandel experiment

A Hong-Ou Mandel HOM experiment has the purpose of measuring the indistinguishability of two photons. The main idea is illustrated in figure 7.6a. The converted photons are sent into a beam splitter, where one of the arms has a delay exactly equal to the repetition rate of the photons. The same arm has a half waveplate, and depending on its orientation it can add a  $\pi/2$  phase to the polarization, making the photons completely distinguishable, or do nothing, leaving the photons indistinguishable. There are now two simultaneous photons, one at the end of each arm, which interfere through another beam splitter. If the photons are indistinguishable, only one detector will click, but if they are distinguishable (orthogonal polarizations), both detectors can click. The HOM visibility is extracted by doing a correlation measurement between the two detectors in the same way that it was done to find the photon purity. The central peak should be suppressed in the indistinguishable case but unchanged in the distinguishable case. The HOM visibility is related to the area of the central peak in the parallel and perpendicular polarization cases through the following equation:

$$V = 1 - \frac{A_{\parallel}}{A_{\perp}}. \quad (7.1)$$

A more detailed illustration of the optical components required to do a HOM visibility measurement in practice is given in figure 7.6b. Due to differences in the losses of each arm, instead of a 50:50 BS a PBS combined with a half waveplate is used, such that the power in both arms can be manually balanced. The half wave plate in the arm with the delay is mounted on a deployable mount, such that the distinguishable case is created by just removing it from the path. The piezo controller and the fiber polarization control are used together, with the purpose to minimize unwanted polarization differences in the arms that can arise due to birefringence in the fibers. The next BS is a 50:50 fiber BS, which then leads to two SNSPDs connected to a PicoHarp time tagger.

Unfortunately due to the fact that the device with the QDs was unavailable after having built the setup for the HOM measurement, the experiment could not be done within the time of my thesis. Thus the results and their required data analysis are outside the scope of this thesis.

### 7.3 Summary

The first part of this chapter was a discussion of the factors that may reduce the conversion efficiency over time and a discussion on how to deal with these factors. The majority of the discussion was centered on the phenomenon denominated as the mysterious non-linear effect (MNLE), which is an



## 8 Concluding remarks and outlook

In this thesis, the theory and experimental principles required for a quantum frequency conversion experiment have been presented. The conversion process achieved was highly efficient and the output light was highly anti-bunched.

To achieve frequency conversion, periodically poled lithium niobate (PPLN) waveguides were used together with a strong pump laser at around 2400 nm fabricated by the company IPG photonics. The model that describes the frequency conversion process is derived in chapter 2, which is then used to simulate the expected outcome of the experimental process. The optical components and geometrical considerations required to achieve frequency conversion are described in chapter 3, with a detailed illustration of the experimental setup presented in figure 3.9.

The first non-linear process achieved was sum frequency generation. This process was used as a proof of concept and as means of characterization of the PPLN waveguides to facilitate the difference frequency generation process. The methods and results are presented in chapter 4. After achieving SFG it was straightforward to achieve DFG. The optimization considerations required to achieve a high end to end efficiency are described in chapter 5, where it is found that the main limiting factors on the end to end efficiency are the losses in the aspherical lenses that couple in and out of the waveguides and the fiber coupling efficiency to the output fiber. For the conversion efficiency to be stable over time, it was important to get rid of a non-linear effect arising due to the pump laser having longitudinal multimode operation. Chapter 7 explores this process in detail and how it was suppressed in practice.

For the process to be quantum frequency conversion it was also important that the state of the incoming light was preserved. The anti-bunching property of the light before and after conversion is explored in chapter 6. It was found that the main source of impurity was second harmonic generation produced in the PPLN waveguides due to the high pump power. Filtering out this source of noise reduced the impurity level by about two orders of magnitude, and the remaining noise was due to photons at the pump wavelength. The noise rate at the pump wavelength was still significant, which decreased the purity of the converted light. This resulted in an increase of the  $g^{(2)}(0)$  value, which was  $0.94 \pm 0.04\%$  before conversion and could be up to  $1.8 \pm 0.1\%$  after conversion. The noise of the pump was then reduced by introducing a reflection grating, but due to unavailability of the quantum dots, the  $g^{(2)}(0)$  could not be measured again. A setup to measure the indistinguishability of the converted photons through a Hong-Ou-Mandel experiment was also built, but the measurements and their subsequent data analysis are beyond the scope of this thesis.

There are two benchmarks achieved in this thesis. The first is a record high internal efficiency of the downconversion process leading to a very high end to end efficiency. These are respectively  $95 \pm 1\%$  and  $40.1 \pm 0.8\%$ . The end to end efficiency value is the double of the goal that was set on the introduction, and will be an important step in achieving the goals of the Fire-Q project. The second is an estimated record low  $g^{(2)}(0)$  at 1550 nm with photons that are expected to be highly indistinguishable based on measurements on the pump drift and the dot spectrum. These qualities make for some of the highest quality single photons at telecom wavelengths produced to date.

### Outlook

In the short term, new measurements with the light from the quantum dots should be made. Now that the grating has been installed and the HOM setup has been built it should be fairly easy to measure the anti-bunching and indistinguishability of the converted light, making it possible to give a reliable estimate of the quality of the setup as a quantum frequency conversion setup.

In the middle term, it may be worth looking into the factors I described that limited the end to end efficiency, and try to do something about them. As I mention in chapter 5 an end to end efficiency above 50% is not unrealistic if the setup is properly optimized. In the middle-long term there is

applying this setup for the goal of the Fire-Q project, which is to implement QKD from NBI to DTU, and see if the current state of the art values for the secure key rate at around 20 km distance can be achieved through its use. Implementing QKD at 20 km is an important field trial demonstration of quantum communication networks.

In the long term, if the setup proves to be able to produce very high quality single photons at telecom wavelengths, these could be used for more advanced quantum communication techniques than QKD, such like long distance entanglement and quantum teleportation. These would in turn open the way to many groundbreaking research possibilities in quantum optics and photonics, and function as an important step for achieving quantum internet.

## Bibliography

- [1] Charles H. Bennett et al. “Experimental quantum cryptography”. In: *Journal of Cryptology* 5.1 (Jan. 1, 1992), pp. 3–28. ISSN: 1432-1378. DOI: 10.1007/BF00191318. URL: <https://doi.org/10.1007/BF00191318> (visited on 04/28/2021).
- [2] Paul-Antoine Moreau et al. “Imaging with quantum states of light”. In: *Nature Reviews Physics* 1.6 (June 2019). Number: 6 Publisher: Nature Publishing Group, pp. 367–380. ISSN: 2522-5820. DOI: 10.1038/s42254-019-0056-0. URL: <https://www.nature.com/articles/s42254-019-0056-0> (visited on 04/29/2021).
- [3] Han-Sen Zhong et al. “Quantum computational advantage using photons”. In: *Science* 370.6523 (Dec. 18, 2020). Publisher: American Association for the Advancement of Science Section: Report, pp. 1460–1463. ISSN: 0036-8075, 1095-9203. DOI: 10.1126/science.abe8770. URL: <https://science.sciencemag.org/content/370/6523/1460> (visited on 04/29/2021).
- [4] N.A. Olsson. “Lightwave systems with optical amplifiers”. In: *Journal of Lightwave Technology* 7.7 (July 1989). Conference Name: Journal of Lightwave Technology, pp. 1071–1082. ISSN: 1558-2213. DOI: 10.1109/50.29634.
- [5] R. Hanbury Brown and R. Q. Twiss. “Correlation between photons in two coherent beams of light”. In: *Journal of Astrophysics and Astronomy* 15.1 (Mar. 1, 1994), pp. 13–19. ISSN: 0973-7758. DOI: 10.1007/BF03010401. URL: <https://doi.org/10.1007/BF03010401> (visited on 04/29/2021).
- [6] Peter Lodahl, Sahand Mahmoodian, and Søren Stobbe. “Interfacing single photons and single quantum dots with photonic nanostructures”. In: *Reviews of Modern Physics* 87.2 (May 11, 2015). Publisher: American Physical Society, pp. 347–400. DOI: 10.1103/RevModPhys.87.347. URL: <https://link.aps.org/doi/10.1103/RevModPhys.87.347> (visited on 04/29/2021).
- [7] Ravitej Uppu et al. “Scalable integrated single-photon source”. In: *Science Advances* 6.50 (Dec. 1, 2020). Publisher: American Association for the Advancement of Science Section: Research Article, eabc8268. ISSN: 2375-2548. DOI: 10.1126/sciadv.abc8268. URL: <https://advances.sciencemag.org/content/6/50/eabc8268> (visited on 04/29/2021).
- [8] Prem Kumar. “Quantum frequency conversion”. In: *Optics Letters* 15.24 (Dec. 15, 1990). Publisher: Optical Society of America, pp. 1476–1478. ISSN: 1539-4794. DOI: 10.1364/OL.15.001476. URL: <https://www.osapublishing.org/ol/abstract.cfm?uri=ol-15-24-1476> (visited on 04/28/2021).
- [9] Jianming Huang and Prem Kumar. “Observation of quantum frequency conversion”. In: *Physical Review Letters* 68.14 (Apr. 6, 1992). Publisher: American Physical Society, pp. 2153–2156. DOI: 10.1103/PhysRevLett.68.2153. URL: <https://link.aps.org/doi/10.1103/PhysRevLett.68.2153> (visited on 04/28/2021).
- [10] S. Tanzilli et al. “A photonic quantum information interface”. In: *Nature* 437.7055 (Sept. 2005). Number: 7055 Publisher: Nature Publishing Group, pp. 116–120. ISSN: 1476-4687. DOI: 10.1038/nature04009. URL: <https://www.nature.com/articles/nature04009> (visited on 04/28/2021).
- [11] Serkan Ates et al. “Two-Photon Interference Using Background-Free Quantum Frequency Conversion of Single Photons Emitted by an InAs Quantum Dot”. In: *Physical Review Letters* 109.14 (Oct. 4, 2012). Publisher: American Physical Society, p. 147405. DOI: 10.1103/PhysRevLett.109.147405. URL: <https://link.aps.org/doi/10.1103/PhysRevLett.109.147405> (visited on 04/28/2021).

- [12] Benjamin Kambs et al. “Low-noise quantum frequency down-conversion of indistinguishable photons”. In: *Optics Express* 24.19 (Sept. 19, 2016). Publisher: Optical Society of America, pp. 22250–22260. ISSN: 1094-4087. DOI: 10.1364/OE.24.022250. URL: <https://www.osapublishing.org/oe/abstract.cfm?uri=oe-24-19-22250> (visited on 04/28/2021).
- [13] Christopher L. Morrison et al. “A bright source of telecom single photons based on quantum frequency conversion”. In: *Applied Physics Letters* 118.17 (Apr. 26, 2021). Publisher: American Institute of Physics, p. 174003. ISSN: 0003-6951. DOI: 10.1063/5.0045413. URL: <https://aip.scitation.org/doi/full/10.1063/5.0045413> (visited on 05/06/2021).
- [14] Gilles Brassard et al. “Limitations on Practical Quantum Cryptography”. In: *Physical Review Letters* 85.6 (Aug. 7, 2000). Publisher: American Physical Society, pp. 1330–1333. DOI: 10.1103/PhysRevLett.85.1330. URL: <https://link.aps.org/doi/10.1103/PhysRevLett.85.1330> (visited on 04/29/2021).
- [15] Hoi-Kwong Lo, Xiongfeng Ma, and Kai Chen. “Decoy State Quantum Key Distribution”. In: *Physical Review Letters* 94.23 (June 16, 2005). Publisher: American Physical Society, p. 230504. DOI: 10.1103/PhysRevLett.94.230504. URL: <https://link.aps.org/doi/10.1103/PhysRevLett.94.230504> (visited on 04/29/2021).
- [16] Yan-Lin Tang et al. “Source attack of decoy-state quantum key distribution using phase information”. In: *Physical Review A* 88.2 (Aug. 8, 2013), p. 022308. ISSN: 1050-2947, 1094-1622. DOI: 10.1103/PhysRevA.88.022308. arXiv: 1304.2541. URL: <http://arxiv.org/abs/1304.2541> (visited on 04/29/2021).
- [17] Kazuya Takemoto et al. “Quantum key distribution over 120 km using ultrahigh purity single-photon source and superconducting single-photon detectors”. In: *Scientific Reports* 5.1 (Nov. 2015), p. 14383. ISSN: 2045-2322. DOI: 10.1038/srep14383. URL: <http://www.nature.com/articles/srep14383> (visited on 04/28/2021).
- [18] Nurul T. Islam et al. “Provably secure and high-rate quantum key distribution with time-bin qudits”. In: *Science Advances* 3.11 (Nov. 1, 2017). Publisher: American Association for the Advancement of Science Section: Research Article, e1701491. ISSN: 2375-2548. DOI: 10.1126/sciadv.1701491. URL: <https://advances.sciencemag.org/content/3/11/e1701491> (visited on 04/28/2021).
- [19] Roland Schiek and Thomas Pertsch. “Absolute measurement of the quadratic nonlinear susceptibility of lithium niobate in waveguides”. In: *Optical Materials Express* 2.2 (Feb. 1, 2012). Publisher: Optical Society of America, pp. 126–139. ISSN: 2159-3930. DOI: 10.1364/OME.2.000126. URL: <https://www.osapublishing.org/ome/abstract.cfm?uri=ome-2-2-126> (visited on 05/01/2021).
- [20] Freja T. Pedersen. “Deterministic Single and Multi-Photon Sources with antum dots in Planar Nanostructures”. PhD thesis. Niels Bohr Institute, Dec. 2020. 156 pp. URL: <https://www.nbi.ku.dk/english/theses/phd-theses/freja-thilde-pedersen/>.
- [21] J. S. Pelc et al. “Long-wavelength-pumped upconversion single-photon detector at 1550 nm: performance and noise analysis”. In: *Optics Express* 19.22 (Oct. 24, 2011). Publisher: Optical Society of America, pp. 21445–21456. ISSN: 1094-4087. DOI: 10.1364/OE.19.021445. URL: <https://www.osapublishing.org/oe/abstract.cfm?uri=oe-19-22-21445> (visited on 05/01/2021).
- [22] D. Bouwmeester et al. “Quantum Dense Coding and Quantum Teleportation”. In: *The Physics of Quantum Information: Quantum Cryptography, Quantum Teleportation, Quantum Computation*. Ed. by Dirk Bouwmeester, Artur Ekert, and Anton Zeilinger. Berlin, Heidelberg: Springer, 2000, pp. 49–92. ISBN: 978-3-662-04209-0. DOI: 10.1007/978-3-662-04209-0\_3. URL: [https://doi.org/10.1007/978-3-662-04209-0\\_3](https://doi.org/10.1007/978-3-662-04209-0_3) (visited on 05/16/2021).

- [23] Peter W Milonni and Joseph H Eberly. “Laser Resonators and Gaussian Beams”. In: *Laser Physics*. Section: 7\_eprint: <https://onlinelibrary.wiley.com/doi/pdf/10.1002/9780470409718.ch7>. John Wiley & Sons, Ltd, 2010, pp. 269–329. ISBN: 978-0-470-40971-8. DOI: 10.1002/9780470409718.ch7. URL: <https://onlinelibrary.wiley.com/doi/abs/10.1002/9780470409718.ch7> (visited on 05/12/2021).
- [24] Bo Chen et al. “Wavelength and temperature dependence of photorefractive effect in quasi-phase-matched LiNbO3 waveguides”. In: *Applied Physics Letters* 89.4 (July 24, 2006). Publisher: American Institute of Physics, p. 043510. ISSN: 0003-6951. DOI: 10.1063/1.2240741. URL: <https://aip.scitation.org/doi/10.1063/1.2240741> (visited on 05/01/2021).
- [25] Vera Marinova et al. “Photorefractive Effect: Principles, Materials, and Near-Infrared Holography”. In: Aug. 1, 2016. DOI: 10.1002/047134608X.W6010.pub2.
- [26] Karsten Buse et al. “Photorefractive Effects in LiNbO3 and LiTaO3”. In: *Photorefractive Materials and Their Applications 2: Materials*. Ed. by Peter Günter and Jean-Pierre Huignard. Springer Series in Optical Sciences. New York, NY: Springer, 2007, pp. 83–126. ISBN: 978-0-387-34081-4. DOI: 10.1007/0-387-34081-5\_4. URL: [https://doi.org/10.1007/0-387-34081-5\\_4](https://doi.org/10.1007/0-387-34081-5_4) (visited on 05/01/2021).

# Appendices

## A Practical guides

### How to couple the 930 nm path into the waveguides

Use the Toptica CTL at maximum power for this alignment. Align the beam such that it roughly follows the blue path shown in fig 3.5. It is very useful to place a camera as illustrated in figure 3.5, to see the reflections from the waveguides. Then follow these steps:

- Remove the waveplates from the path.
- Place the camera such that it records the reflexion from the waveguides. It might be a bit tricky. For this I recommend using the detector cards, where if the power is high enough even the reflexion will be visible but very dim. Once found it will be necessary to reduce the shutter time and gain of the camera to center it.
- Block the laser light and turn the shutter time of the camera to the maximum. Use the IR broad light source by shining it from the back side (collection side) of the waveguides. This should give a clear view of the structure of the waveguides at the current alignment position.
- Use the mirrors to make the beam spot overlap with the desired waveguide, then beam walk such that moving the lens in and out of focus only changes its size but not its position.
- The laser spot should now be visible with a detector card on the collection side of the setup. Then move the camera to the output of the waveguides such that this spot is visible in the camera. Some OD filters might be necessary in order not to saturate the camera.
- Beam walk the spot until it looks single moded. This can be hard, but the point is that if there are many vertical modes, the beam should be walked in the vertical direction and the same for the horizontal direction. Once the beam is single moded the transmitted power should be at least 70% of the power before the waveguide.
- Put back the waveplates, if placed correctly the single mode on the camera will be completely unchanged.

Getting a single mode might be quite hard, but it is essential to achieve difference frequency generation. If the light is single moded, the transmission through the waveguides will be optimized. Measure the power before the input aspherical lens and after the collection aspherical lens. If the transmission is above 70% then the light is probably close to being single moded. There was a long period where I could not achieve single moded light and the transmission was always below 60%. Later I found that this was because there was some dirt in the waveguides, and after cleaning them it was possible to get the right transmission and mode profile again.

### How to couple the 1550 nm path into the waveguides

For the 1550 nm path, connect the same 930 nm CTL laser to the input where the 1550 nm laser diode usually is connected. Place the camera in the same position as for the 930 nm coupling. Follow the first 4 steps of the 930 nm coupling. Then do the following:

- Connect the diode laser into the input
- Put a detector card on the collection side of the waveguides. The spot will probably look distorted. Move one of the mirrors until it looks gaussian.

- Place the photo detector such that it collects the beam. Beam walk to optimize the power output.

At 1550 nm the light in the waveguides will be mostly single moded, so the optimal coupling is simply the one with the highest power.

### How to couple the pump into the waveguides

Given that the pump can neither be detected by the camera or by the fluorescent detector cards, it is strongly recommended to use a second laser as an aid when aligning it. This laser might as well emit visible light for easy alignment. It will also be necessary to use the camera to capture the reflection coming from the waveguides, so it should be placed as shown in figure 3.5. The idea is to align the coming visible light laser such that it follows exactly the same path as the pump laser. Then couple into the desired waveguide by looking at the reflection in the camera. After doing this many times, I found that the fastest way to do it was with the following steps:

- Collimate the beam in the beam expander. This is not strictly necessary, but it makes the coupling easier. To collimate the beam I recommend using 2 iris pinholes, one close (about 10 cm) and one far (about 50 cm) from the beam expander. Put a powermeter after the second pinhole. Adjust the beam expander such that both pinholes cut the beam with the same amount when the closing is at the same size. Check that the distance between the lenses is around 60 mm.
- Install two iris pinholes as shown in figure 3.6. Make sure that the pump beam is centered through these. For this I recommend closing them almost completely and optimize the position by looking at the power transmitted with a powermeter.
- Beam walk the visible light laser such that it is centered through both pinholes. To do this precisely I recommend to look at its reflection in the camera. Align such that the first "mirror" gets the beam through the first pinhole and the second mirror gets it through the second, repeat until the beam goes through both. Make also sure that its beam is not being cut by the waveplates.
- Now the pump and the visible laser should be following the same path. Using the last two mirrors before the dichroic, center the visible light laser into the desired waveguide by looking at the reflection on the camera.
- The pump beam should now be going into the waveguide, but not very well coupled. The next step is to optimize its coupling by doing SFG. Turn on the 1550 nm laser diode and couple it into the waveguide. Set the pump wavelength such that it will produce SFG, see the table in section 4.1. The wavelength does not need to be exact, but close.
- Place the camera on the collection side and check if there is a spot of SFG. If there is, beam walk the pump with the last two mirrors to make the spot brighter.
- Replace the camera with a 930 nm photodetector. Make a scan of the pump wavelength and set it to the optimal wavelength for SFG.
- Beam walk the pump such that the SFG is optimized on the powermeter.

## B Gaussian beam propagation theory

This appendix contains the equations used for the gaussian beam simulations that were necessary for the optimization of the pump coupling into the waveguides. The equations in this appendix are derived from the gaussian beams chapter in Laser Physics by Milonni and Eberly [23].

A gaussian beam propagating in the z direction with a given polarization has the following equation:

$$E(\mathbf{r}) = A(\mathbf{r})e^{iP(z)}e^{ik(x^2+y^2)/(2R(z))}e^{-(x^2+y^2)/w^2(z)}. \quad (\text{B.1})$$

where  $R(z)$  is the radius of curvature of the beam and  $w(z)$  is the beam width. They can both be absorbed into the  $q$  parameter

$$\frac{1}{q(z)} = \frac{1}{R(z)} + \frac{i\lambda}{\pi w^2(z)}. \quad (\text{B.2})$$

where  $\lambda$  is the wavelength in the material. The  $q(z)$  parameter propagates according to the equation

$$q(z) = q_0 + z. \quad (\text{B.3})$$

where

$$q_0 = \frac{-i\pi w_0^2}{\lambda}. \quad (\text{B.4})$$

in which  $w_0$  is the beam width at the waist of the given laser. This is for the pump laser of this experiment around 0.8 mm. The  $P(z)$  parameter is a quantity linked to the overall phase of the beam and is calculated by letting  $P(0) = 0$  and using the equation

$$\frac{dP}{dz} = \frac{i}{q}. \quad (\text{B.5})$$

When going through optical elements, the  $q$  parameter of a gaussian beam changes. In ray optics the ABCD matrix formalism would be used to calculate what happens to the ray vector going through the elements. Two common ray matrices are

$$\text{Lens: } \begin{bmatrix} 1 & 0 \\ -1/f & 0 \end{bmatrix}, \quad \text{Free space: } \begin{bmatrix} 1 & d \\ 0 & 1 \end{bmatrix}, \quad (\text{B.6})$$

where  $f$  is the focal lens of the lens and  $d$  is the distance of propagation. A similar approach can be used with gaussian beams by letting

$$\begin{bmatrix} A & B \\ C & D \end{bmatrix} \rightarrow q_f = \frac{Aq_i + B}{Cq_i + D}, \quad (\text{B.7})$$

where  $q_f$  is the  $q$  parameter at the output and  $q_i$  at the input. In my simulation I assumed the beam waist to be right at the output of the laser, and then calculated the propagation of  $q(z)$  using eq B.3, and B.7. Then the value of the beam width and curvature radius at the end of the propagation can be derived from eq B.2 to be

$$R = \frac{1}{\text{Re}\left(\frac{1}{q}\right)}, \quad (\text{B.8})$$

$$W = \sqrt{\frac{\lambda}{\pi \text{Im}\left(\frac{1}{q}\right)}}.$$

To calculate the coupling of a gaussian beam to a waveguide mode, the following equation is used

$$\eta = \frac{|\int E_{in}^* E_{WG} dA|^2}{\int |E_{in}|^2 dA \int |E_{WG}|^2 dA}. \quad (\text{B.9})$$

where the integrals are taken over xy plane of the beam profile. The incoming field  $E_{in}$  is the gaussian beam from equation B.1 using the resulting  $q$  and  $P$  parameters from the simulation, and  $E_{WG}$  is the fundamental mode of the waveguide extracted from the Comsol simulation.

## C 1550 nm SNSPD and TT characterization

This appendix contains measurements done to characterize the 1550 nm SNSPD detectors when doing two photon correlation measurements. The aim is to find which anomalies of the two photon correlation  $g^{(2)}(\tau)$  measurements come from detector biases and which ones are due to physical phenomena.

The first anomaly to be discussed is the high peak in the center of figure 6.8a. A slightly more zoomed version of this plot can be seen in figure C.1a. From here it is clear that the two peaks to the left of the center are higher than the rest and that there is also a bunching effect in the central 100 ns of the measurement. This should be compared to a measurement done with the mira laser going through the frequency conversion, as showed in figure C.1b. There is one peak to the left of the center that is clearly higher than the other ones, but no clear bunching effect in the 100 ns close to the center. It can therefore be concluded that the high peaks close to the center are due to instrument bias, but the bunching effect has a physical root and is inherent to the measurement with the quantum dot.

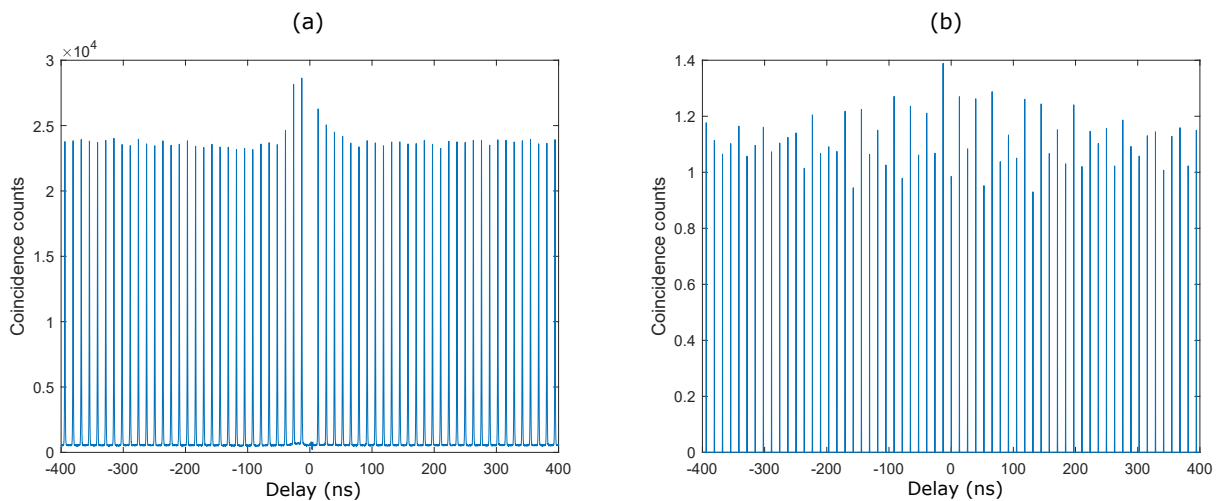


Figure C.1: (a) Two photon auto-correlation measurement of the converted light, where the zoom is somewhere in between the ones from figure 6.8a and b. (b) Two photon auto-correlation measurement for the attenuated mira laser with the same zooming as in (a).

The second anomaly to be discussed is the clear drop on the right side of the blue curve in figure 6.9. A detail that was not explained in the main text is that given to a small difference in the length of the fibers between the BS and the SNSPDs, the 0 ns time delay is not in the same place as the maximum of the central (attenuated) peak of the two photon autocorrelation measurement. I have corrected this in all of the plots of the main text by moving the center of the plot to the place of the central peak. If this was not done, the blue curve in figure 6.9 would be like in figure C.2a, which is the same but un-shifted in the first axis. It can be seen that the drop happens close to  $\tau = 0$ . To understand more about the drop at the center, the red curve of figure 6.9 is amplified and shown as the red curve in figure C.2a. It can be seen that in both cases there is a drop for time delays very close to zero. This means that this drop is due to instrument bias of either the time tagger or the SNSPDs. The drop was not present for the measurement with the Swabbian TT, which means that it is most likely a bias of the PicoHarp TT. The reason for this bias is unknown.

The last instrument property to discuss in the instrument response function (IRF) that was used in the fit. The value of  $\sigma$  in equation 6.3 was determined to be 160 ps by using a fit, but in the following I will discuss my attempt to measure it directly. The pulse width of the Mira laser should be much shorter than the instrument response time of the SNSPDs. It can therefore be suggested that measuring the two photon correlation of the Mira laser should give the IRF of the 1550 nm SNSPDs.

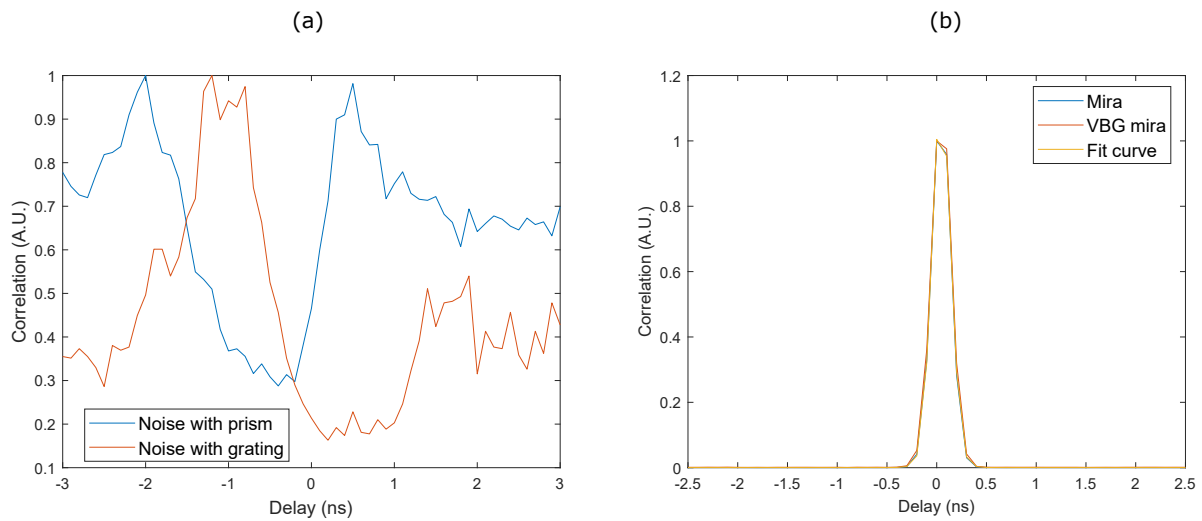


Figure C.2: (a) Noise drop at the center of the two photon correlation measurements for both the QD and the converted Mira experiments. (b) Comparison of the two photon correlation for the converted Mira with and without the volume Bragg grating (VBG). The fitted curve was calculated for the case without the VBG.

As a test for the validity of this suggestion, the measured curve for the Mira and for the VBG Mira, where the pulse width is enhanced by a factor of 5, should be compared. Since both pulse durations should be so short that it is only the IRF that means something for the measurement result, the two photon correlation curves should be identical. This was indeed the case as can be seen from comparing the blue and red curves of figure C.2b, reassuring that the width of the curve was solely dependent on the IRF. The curve was then fitted and the result is the yellow curve of the figure. The fit result says that the instrument response time  $\sigma = 60$  ps, which can be taken as a measurement of such quantity.

If the measurement of the instrument response time is inserted in equation 6.3 and the fit is done with that as a fixed parameter, the quality of the fit falls drastically. For the fit to have a good quality, the instrument response time should be roughly 3 times of what was measured. This suggests that there is something wrong with my measurement of the instrument response time. But I have not been able to find the root of the problem.

## D Possible explanations for the MNLE

After having suppressed the MNLE it was possible to produce stable frequency conversion with an end to end efficiency consistently above 40%, but in the main text the MNLE has only been explained in terms of how it manifests on the main experiment, and how it can be suppressed. Its physical cause was not been explored. In this appendix I will explore different hypothesis of physical phenomena that might explain the MNLE, and connect them to experiments or simulations I have done to prove (or disprove) them. The criteria to accept a physical phenomenon as a viable explanation for the MNLE are the following:

1. It has to create conversion efficiency instability emerging at high pump powers in the waveguides. The instability is not present at low pump powers.
2. It has to be responsible for the clear drops on a pump wavelength scan, which are not necessarily in the same position if the scan is repeated. The drops only emerge at high pump powers.
3. It has to be very sensitive to changing the wavelength of the pump even by very small amounts. The reaction time has to be below 1s.
4. The phenomenon disappears when optimizing the position of piezzo 3, which allegedly means that there is single mode (and thus single frequency) operation of the pump laser.

**Temperature fluctuations:** If there are many impurities in the waveguides, they will absorb the high pump power and be warmed up. If the temperature is locally raised, the refractive index will change, giving a bad phasematching and thus a lower conversion efficiency. Such local temperature fluctuations would only be present for high pump powers, which fulfills the first criterion. It is unclear how the temperature fluctuations can be dependent on the wavelength, as most impurities absorb infrared light no matter the wavelength. Temperature changes also have relaxation times which are typically higher than one second, especially if they have to be big enough for them to make a noticeable difference in the phasematching. It is also unclear why they should only happen for multimode operation. As a check, I tried to change the overall temperature whenever the efficiency dropped, but this rarely improved the conversion efficiency, meaning that either the temperature fluctuations were not affected by changes in their surrounding temperature, or they were not causing the drop. Also blocking and unblocking the pump did not help, the efficiency drop was still there, even though the temperature fluctuations should have dissipated. So even though temperature fluctuations explain the first phenomenon, they cannot explain the other 3. My two small experiments also make them improbable as an explanation, and thus it may be concluded that temperature fluctuations have very little chance to explain the MNLE.

**Beamfront distortions:** It is possible that even though the pump light is being coupled to the waveguides, it could be coupled to its second order mode, which would not contribute to the frequency conversion process. According to the simulations, the second order mode should be very hard to excite using a Gaussian beam as the input, but if the input beam is distorted, such that the shape is different, it might be excited. Back-reflections into the laser can lead to instabilities of the laser cavity, which may result in beamfront distortions. The back-reflections should be filtered by the Faraday isolator, but if it was not aligned correctly or the amplitude of the reflections was just too high, they may still have an influence. Such back-reflections have a higher chance of creating distortions when the power in the waveguides is high, making it possible for them to fulfill the first criterion. The second and third criteria can also be fulfilled by this effect, as changing the wavelength also means making changes to the laser cavity, which should also result in distortions to the beamfront. The problem comes when trying to explain the fourth criterion with this hypothesis, as it is unclear why the problem of the back-reflections would be solved by making the pump light singlemoded. As a test, I made an experiment where I tried to minimize the back reflections by placing two iris pinholes, one right before

the dichroic mirror, and one right before the beam expander. The pinholes were closed down to the point where they cut about 30% of the incoming power, which means that the pump power in the waveguides was cut by about 50%, and the assumed back-reflected power should be cut by at least this fraction, but probably even more due to it not having exactly the same beam size and direction as the incoming beam. The measurement for the pump scan in this experiment showed that the MNLE was still present and the spectrum was very similar to a measurement where the pump power was attenuated by the same amount using the PBS. This experiment makes the back-reflection hypothesis less likely as an explanation. It should also be said that this hypothesis was improbable to begin with, as it was unlikely that the distortions created by the very small back reflections were exactly the ones needed to excite the second order mode of the waveguides.

**Interference by the SHG:** There are at least two non-linear processes happening simultaneously in the waveguides during the frequency conversion process, these are DFG and SHG. This hypothesis is that the SHG for some reason interferes with the DFG process, decreasing its conversion efficiency. The SHG is especially strong for high pump powers and is highly dependent on the pump wavelength, so the first 3 criteria can be easily explained by this hypothesis. It is unclear how this hypothesis fits into the fourth criterion, as splitting the power of the pump between slightly different wavelengths should have very little influence on the total amount of SHG, and if it had, it would be for it to decrease, due to the quadratic nature of the SHG with respect to the pump power. But is it possible for this interference to happen? There are two reasons why this interference may happen, the first could be that the pump power decreased simply because it was converted to another wavelength, and the second is that the SHG process, added a phase to the DFG process, as both processes can change but also depend on the complex value of  $a_1$  (equations 2.18 and 6.1), this phase change could make the DFG reverse to SFG before it achieved its maximum. The first possibility is not viable, as the SHG can maximally be in the order of hundreds of microWatts, which compared to the hundreds of miliWatts of the pump power inside the waveguide should be negligible. The second possibility is not as simple and can only be confirmed through simulations or measurements. Figure D.1 shows a

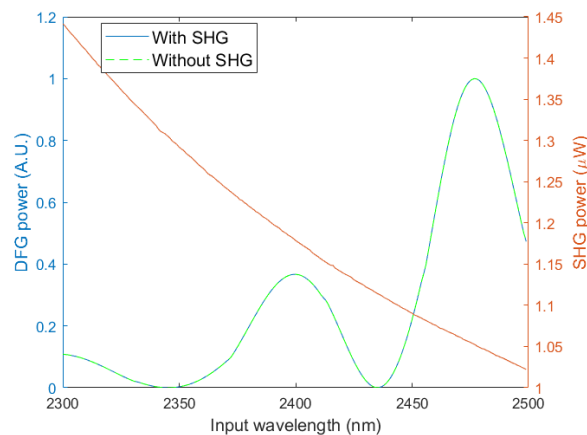


Figure D.1: Simulation of simultaneous DFG and SHG, where the pump width oscillations described in section 4.2 are taken into account.

simulation of what happens when DFG and SHG are taken into account simultaneously. The blue curve is the simulation when the SHG is happening simultaneously, and the dashed green curve is the simulation where there is no SHG. It can be seen that the curves overlap perfectly, meaning that the presence of SHG makes no difference in the DFG process. Thus in this simplified model where there is only one SHG mode, there should be no interference with the main DFG process. But as was seen in figure 6.2c, the SHG light is composed of many higher order modes which are not taken into account by the simulation. Therefore the only way to be completely sure is to also take a measurement where

the SHG and the DFG are simultaneously measured. Such a measurement is not easy to do, as the powermeter that can detect the SHG light is also sensible for the telecom and pump wavelengths, making it hard to distinguish the signals from each other. As an alternative to using the powermeter I found that it was better to use the SNSPDs. The SHG light was reflected by the longpass filter and sent through a 930 nm fiber to the 930 nm SNSPDs, while the telecom light was sent through the regular route to the 1550 nm SNSPDs. Both signals had to be attenuated by neutral density filters for them not to saturate the SNSPDs. In principle there would be some pump light at 2400 nm coupling to the 930 nm fiber used to measure the SHG, but this one should be heavily attenuated because the fiber was 50 m in length and designed for a much lower wavelength, as well as the 930 nm SNSPDs being very insensitive for the pump wavelength. The result of taking such a measurement can be seen

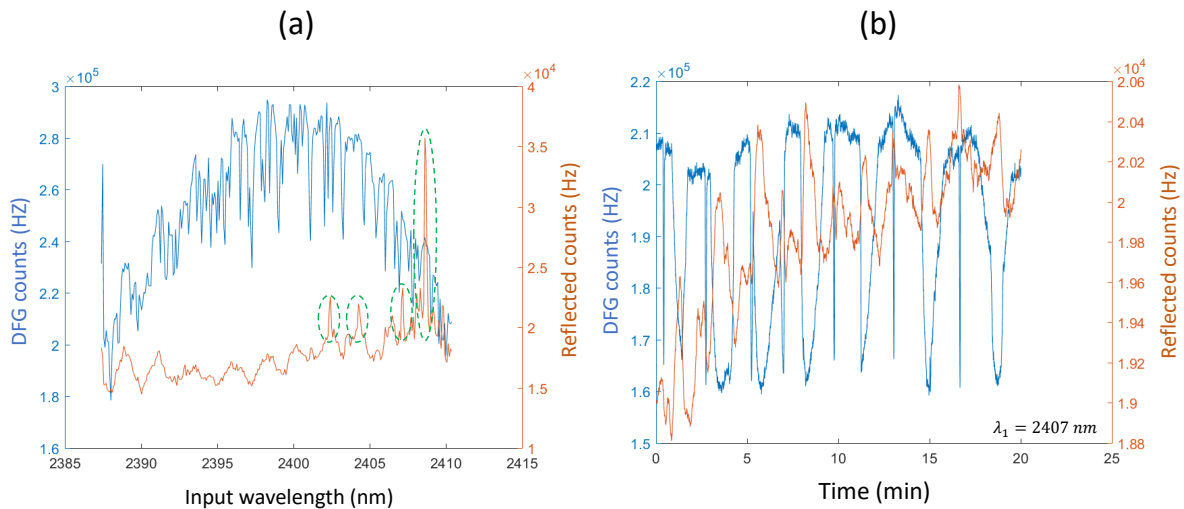


Figure D.2: (a) Pump wavelength scan experiment where the DFG and SHG are measured simultaneously for WG 11. The CTL was used as the input with  $\lambda_3 = 942.02$  nm. (b) Simultaneous measurement of DFG and SHG over time for a pump wavelength where the SHG was observed to have a high intensity.

in figure D.2a, where both processes were measured simultaneously while the pump wavelength was scanned. Unfortunately I did not succeed in filtering out the photons from the pump completely. For the majority of the wavelengths, the counts measured in the 930 nm SNSPD come from photons at the pump wavelength, but there are four peaks that can be attributed to SHG, which are enclosed by dashed green lines. There is no clear correlation between the SHG peaks and the DFG drops, and the DFG is not significantly smaller in the region where the SHG becomes more prominent. Figure D.2b shows a time measurement at the wavelength that gave the highest SHG peak. This measurement was taken on a different day, shortly after the pump laser was turned on, since that is when its mode hopping is most active, which will be relevant for the next phenomenon. It can be seen that all of the jumps happen simultaneously for both processes, and that they are mostly anticorrelated, such that drops in DFG mean increases in SHG.

The conclusion about the interference of the SHG with the DFG is that it is probably not there. This is supported by the result from the simulation and a simultaneous measurement during a pump wavelength scan. But an important lesson from this dead end is that if the SHG is very prominent, it is enhanced when the DFG drops, suggesting that the MNLE responsible for the drops in DFG efficiency has the possibility of enhancing the SHG efficiency. This should now be considered as a fifth criterion for a plausible explanation of the MNLE.

**The photorefractive effect:** a non-linear phenomenon that has been observed in PPLN waveguides is the photorefractive effect (PRE) [24]. It happens when there is a strong and irregular electric field, such as that produced by two-moded coherent light of very similar wavelengths. The field ionizes some of the atoms in the crystal, and the ionized charges are then attracted to the negative maxima of the electric field. This creates a spatial charge distribution which in turn alters the refractive index of the material, adding spatial oscillations to the refractive index [25]. This is illustrated in figure D.3a. In my DFG experiment the irregular electric field could be caused by the interference pattern of the two frequency components coming out of the pump laser when operating in multiple longitudinal modes. If the pump power is high enough this irregular field can lead to oscillations in the refractive index through the photorefractive effect. As was discussed in section 4.2, spatial oscillations of the refractive index lead to a shift of the phasematched wavelength and a higher pump power requirement to achieve full conversion. So if the pump laser operation jumps from single to two moded the conversion efficiency will drop due to the worsening in the phasematching. From figure 3.6b it can be seen that the difference in wavelength for two longitudinal modes is in the order of 0.89 GHz or 17 pm. A simulation for the spatial amplitude distribution of the pump electric field for two interfering waves with wavelength differences of this order can be seen in figure D.3b. The orange curve is for a spectral separation of 17 pm and is the one that corresponds to the 0.89 GHz that were measured by the company. Using this as a reference for the shape of the PRE induced refractive index oscillations, the influence of the PRE on the spectrum of a pump scan was simulated. The result is seen in figure D.3c, where it is clear that the PRE with the currently discussed parameters should have an influence on the converted spectrum, and this spectrum has resemblances to the one in figure 7.2b caused by the MNLE.

The PRE has been well documented on PPLN for wavelengths below 1000 nm [26], but it is not well understood whether it happens for wavelengths above. In [24] the PRE is measured for a pump at 1550 nm, but it is attributed to the SHG created by that pump. On the other hand most of the measurements are done by lasers at single frequencies, thus making it hard to determine whether it can be ruled out for two-frequency laser light. It is possible that this kind of PRE, which happens at wavelengths as long as 2400 nm, and is due to two-frequency laser operation has never been observed before. Assuming that the PRE can happen to a significant degree at 2400 nm, it can fulfill criteria 1,2 and 4 for the explanation of the MNLE. The third criterion on the other hand is uncertain, as the relaxation time of the PRE measured for lithium niobate is usually in the order of minutes, but as previously mentioned, these measurements are probably done for a different type of PRE, making it hard to rule out the hypothesis based on those measurements.

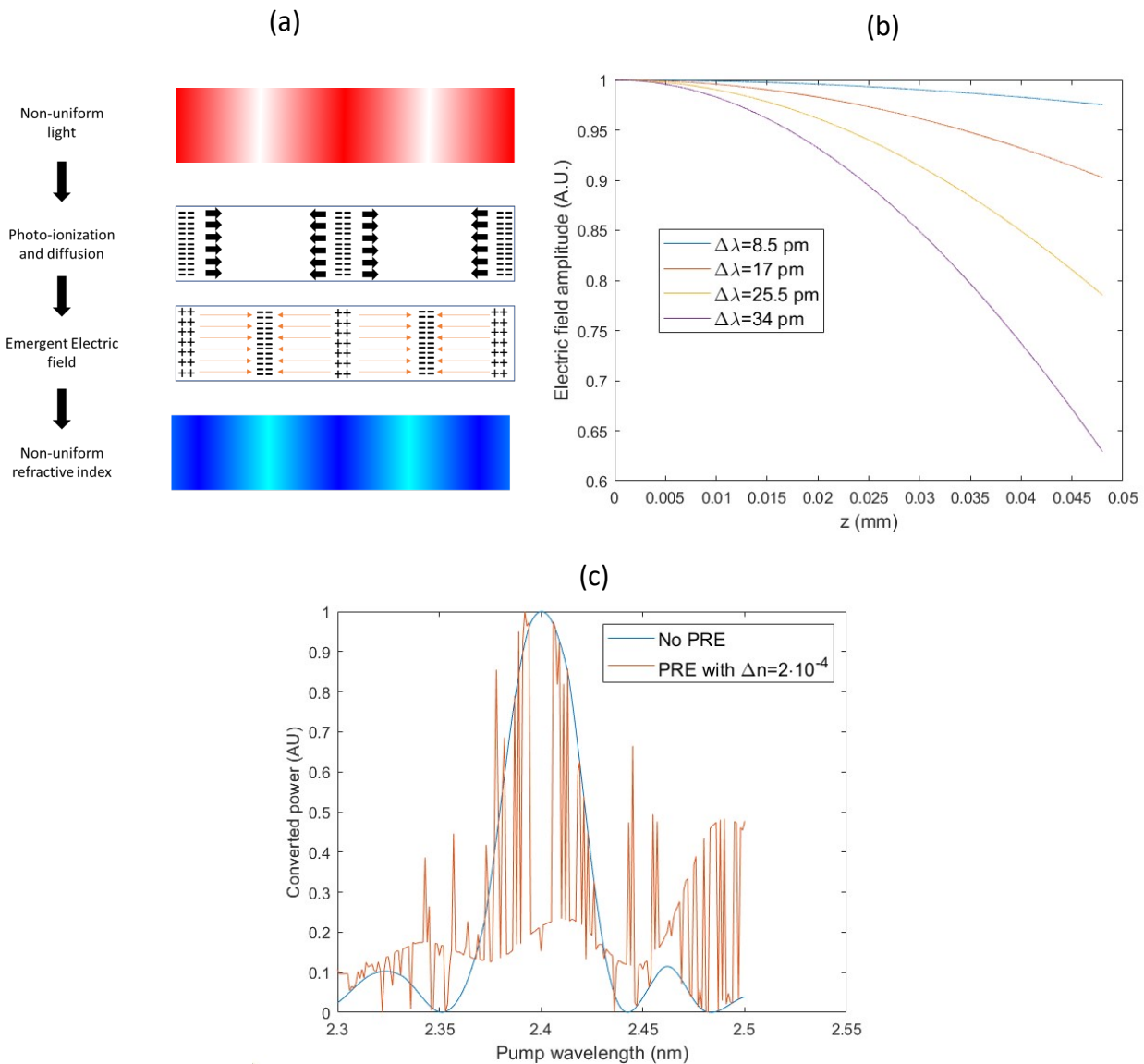


Figure D.3: (a) Illustration of how the photorefractive effect works. Figure inspired by [25] (b) Electric field amplitude as a function of propagation distance for two waves interfering with each other with a slight detuning at the pump wavelength. (c) Simulation of a pump scan spectrum if the PRE is taken into account. Done by calculating the red curve in (b) and then assuming that the amplitude of the refractive index oscillations was  $2 \cdot 10^{-4}$  which is a reasonable value according to [26].

There are two more arguments in favor of the PRE being present and causing the MNLE. The first is its influence on the SHG. As was discussed in section 6.1 the SHG can be enhanced by spatial oscillations in the refractive index. This would explain the correlation between the jumps in the DFG and SHG in figure D.2b. The second is that the effect of the PRE on frequency conversion has been shown to decrease with the temperature [24]. I made pump scans for the SFG process through different temperatures. Up to 50 C, there was no noticeable difference in the drops, and the resulting measurement at  $T=47 \text{ C}$  can be seen in figure D.4a. Above from 50 C it became very hard to achieve a good conversion efficiency, but it was also observed that the PRE started to disappear, and already at 55 C it was not possible to see its effect. The result of the pump scan at  $T=57 \text{ C}$  can be seen in figure D.4b. It is hard to draw conclusions from this experiment, as it is still unknown why the

efficiency drops for temperatures above 50 C, but if this effect is assumed to be independent of the MNLE, it can be concluded that the MNLE is attenuated at high temperatures.

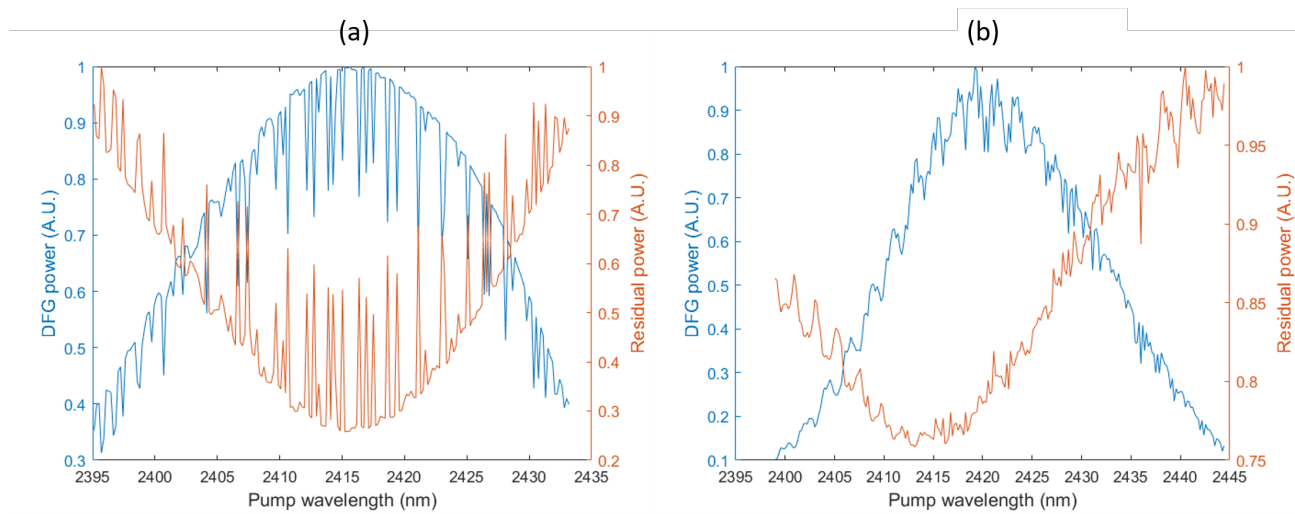


Figure D.4: (a) DFG pump scan for WG 11 at maximal pump power for T=47C. (b) DFG pump scan for WG 11 at maximal pump power for T=57C.

In conclusion, even though the PRE has not been measured at this wavelength and its relaxation time is typically much higher than 1s, it fits very well into explaining all of the phenomena related to the MNLE. A summary of the 4 hypothesis reviewed is given in table 3, and of these four, the PRE is the one with the least critical arguments against it and therefore the most likely to be the correct explanation. But to be completely sure, other measurements should be taken, and until then the source of the MNLE will remain unknown.

Phenomenon	Crt. 1	Crt.2	Crt. 3	Crt. 4	Crt.5	Experiments	Other arguments
Temperature fluctuations	Yes	No	No	No	No	Against	None
Backreflections	Yes	Yes	Yes	No	No	Against	None
SHG interference	Yes	Yes	Yes	No	Yes	Unconclusive	Strongly against
Photorefractivity	Yes	Yes	No	Yes	Yes	In favor	Against

Table 3: Comparison of the different hypothesis and how well they fulfill the criteria required for them to explain the MNLE. The fifth criterion is the enhancement of the SHG.

## **E List of abbreviations**

<b>AR:</b> Anti-reflection	<b>NIR:</b> Near infrared
<b>BE:</b> Beam expander	<b>PM:</b> Polarization mantaining
<b>BS:</b> Beam splitter	<b>PPLN:</b> Periodically poled lithium niobate
<b>CTL:</b> Continuous tunable laser	<b>QD:</b> Quantum dot
<b>CW:</b> Continuous wave	<b>QKD:</b> Quantum key distribution
<b>DFG:</b> Difference frequency generation	<b>RK4:</b> Runge-Kutta 4th order (method)
<b>DTU:</b> Technical university of Denmark	<b>SFG:</b> Sum frequency generation
<b>FWHM:</b> Full width half maximum	<b>SHG:</b> Second harmonic generation
<b>HBT:</b> Hanbury-Brown and Twiss	<b>SNSPD:</b> Superconducting nanowire single photon detector
<b>HOM:</b> Hong-Ou-Mandel	<b>TE:</b> Transversal electric
<b>IPG:</b> Name of laser company (IPG photonics)	<b>TM:</b> Transversal magnetic
<b>IRF:</b> Instrument response function	<b>TT:</b> Time tagger
<b>MNLE:</b> Mysterious non-linear effect	<b>VBG:</b> Volume Bragg grating
<b>NBI:</b> Niels Bohr institute	<b>WG:</b> Waveguide
<b>ND:</b> Neutral density (filter)	